MPHIL

Blood Damage in Mechanical Circulatory Support Systems

-

Khoo, Dominica Pi Ying

Award date:
2023

Awarding institution:
University of Bath

Blood Damage in Mechanical Circulatory Support Systems

submitted by

Dominica Khoo Pi Ying

for the degree of Master of Philosophy

of the

University of Bath

Department of Mechanical Engineering

July 2022

Publications

Some of the work contained in this thesis has been previously published in the International Journal of Artificial Organs [1]. As the first author of that journal paper, my contributions were establishing computational LVAD models and methods to study the stresses present in the VADs. The CFD simulations were carried out by me, Dominica Khoo as the first author at different operating conditions for different LVAD designs to investigate the effect of fluid dynamic stresses. The results as written in my publication [1] and in Chapter 4 of my thesis showed a significant volume of other forms of mechanical stress experienced by blood in VADs, specifically elongational stress. The work was further extended into Chapter 5, whereby the effects of pulsatility were accounted and the difference in the flow field, shear stresses and residence times for HVAD patients with a typical average left ventricular flow rate were described. The other authors were my PhD supervisors who supervised me in this research process. The sections of text from this publication which are in the thesis are in section 2.3 and 2.4 in Chapter 2, in section 3.1 and 3.2 in Chapter 3 and section 4.5 in Chapter 4. Other publications which relate to the work I have done for my paper and thesis were published in the abstract for the 23rd Congress of the European Society of Biomechanics [2] and BioMedEng18 Conference [3].

Summary

Despite the evolution of Ventricular Assist Devices (VADs), VAD patients still suffer from complications due to the damage to blood by fluid dynamic stress. Measurements and simulations of cell and protein deformation show normal and shear stresses deform, and potentially damage, cells and proteins differently.

The thesis explores numerical models for blood damage which are generally based on the Scalar Shear Stress (SSS), a scalar invariant calculated from the tensor components in analogy with the von Mises stress for solids and first introduced by Bludszuweit [4]. Relationships between damage to the blood components and the SSS are then used in predictions of blood damage from the whole device. In addition, flow conditions such as constant flow rate applied at the inlet boundary do not reflect a pulsating flow of a beating heart. Combining flow dynamics of the HVAD with flow data from a pulsatile mock circulation loop, the influence of flow pulsatility on device-induced blood trauma was investigated.

The calculations showed normal stresses do occur in rotary VADs: the fluid volumes experiencing normal stress above 10 Pa were 0.011 ml (0.092%) and 0.027 ml (0.39%) for the HeartWare HVAD and HeartMate II, and normal stresses over 100 Pa were present. Considering thresholds for red blood cell and von Willebrand factor deformation by normal and shear stresses, the fluid volumes causing deformation by normal stress were between 2.5 and 5 times the size of those causing deformation by shear stress. In pulsatile flow, the normal stress volumes were higher above the 10 Pa threshold which was 0.024 ml (0.2 %). There is an increase in 2 orders of magnitude of normal stress compared with steady flow at peak flow, which existed in the clearance between the top housing and rotating impeller. Larger variations were observed in the flow profile and stress field over time, but the time-averaged values were indiscernible compared to fixed-rate (steady flow). It was found the results clearly show that while blood within rotary VADs experiences more shear stress at much higher magnitudes as compared with normal stress, there is sufficient normal stress present to cause deformation of, and potentially damage to, the blood components.

Acknowledgments

The completion of this undertaking could not have been possible without the participation and assistance of so many people whose names may all not be enumerated. Their contributions are sincerely appreciated and gratefully acknowledged. However, I would like to express my deep appreciation, particularly for the following:

Dr Katharine Fraser, my first supervisor for the opportunity, her help and support in writing this thesis during the pandemic. Her encouragement is what kept me going and not giving up my work and writing.

Professor Richie Gill and Dr Andrew Cookson, my project supervisory team for their expert advice and support, and for guiding me throughout my PhD journey.

To my friends and family, for all their support over the last 4 years. Especially, my parents and Leong Chee Hang who have supported me unquestioningly.

Nomenclature

Subscripts and Abbreviations

MCS ..... Mechanical Circulatory Support

VAD ..... Ventricular Assist Device

CFD ..... Computational Fluid Dynamics

HF ..... Heart Failure

CVD ..... Cardiovascular Disease

MI ..... Myocardial Infarction

BiVAD ... Bi-Ventricular Assist Device

BTT ..... Bridge To Transplant

BTR ..... Bridge To Recovery

DT ..... Destination Therapy

BTC ..... Bridge To Candidacy

BTD ..... Bridge To Decision

TAH ..... Total Artificial Heart

IABP ..... Intra-Aortic Blood Pump

FDA ..... Food and Drug Administration

PVAD .... Pulsatile Ventricular Assist Device

RBC ..... Red Blood Cell

WBC ..... White Blood Cell

vWf ..... Von Willebrand Factor

PFH ..... Plasma Free Haemoglobin

H-Q ..... Pressure Head - Volumetric Flow Rate

PIV ..... Particle Image Velocimetry

NIH ..... Normalised Index of Haemolysis

LV-VAD .. Left Ventricle to Ventricular Assist Device

CAD ..... Computer Aided Design

HTB ..... Hydrodynamic Thrust Bearing

STL ..... Stereolithography

NS ..... Navier Stokes

MRF ..... Moving Reference Frame

MP ..... Mixing Plane

TRS ..... Transient Rotor Stator

DI ..... Deformation Index

SSS ..... Scalar Shear Stress

RMS ..... Root-Mean-Square

SPH ..... Smoothed Particle Hydrodynamics

List of Figures

List of Tables

Contents

Chapter 1

Introduction

1.1 Motivation

Since the 1980s, one of the most important scientific breakthroughs of the era is the ability to support and replace the heart's function with either mechanical circulatory support (MCS) or heart transplantation. In the late 1960s and early 1970s, visionary people started to devise ways to artificially assist the heart. Originating thus, the field of MCS. The prevalence of heart failure (HF) and the number of patients treated with Left Ventricular Assist Devices (LVADs) have increased. During these last decades, innovation in cardiac surgical procedures became a key component of the development of mechanical assist devices. Since then, many kinds of mechanical assist devices have been developed to assist the heart, such as cardiopulmonary bypass machines (CPB), intraortic balloon pumps (IABPs), and Ventricular Assist Devices (VADs), the last, a promising long-lasting therapy for patients with chronic heart failure (CHF).

However, the increasing development of ventricular assist devices (VADs) or commonly referred to as rotary blood pumps are considerably swayed by the rising concern over deficient organ donations for transplant. Shortage of available organs in Europe persists [5], with an average of 15–30% of patients dying annually on the waitlist. Associated with this is the growth of patient numbers with approximately 14,000 patients being admitted to the hospital each year with the most severe heart failure symptoms [6].

In modern-day cardiovascular medicine, the survival rates of patients with rotary blood pumps have improved immensely compared to earlier designed pulsatile devices after the first year of implantation with an 82% survival rate (refer to section 2.1.3). Although VADs are becoming an established therapy for heart failure patients [7], there are serious complications related to the non-physiological flow conditions experienced by blood in the devices implanted. A large number of patients experience post-surgical adverse events like thrombosis, bleeding and infections, which are 50% related to blood damage and that makes it difficult for patient recovery [8, 9].

There are various attempts to develop the potential of combining CFD with the mechanical and biomechanical aspects to develop a numerical model of combined LV-LVAD to be utilised in clinical studies. Furthermore, the computational model will provide the capability of predicting regions of blood damage in VADs based on fluid dynamic stresses. The new information obtained can be used to improve the new generation of VAD designs.

1.2 Thesis Overview

Chapter 1 provides a general introduction to the project. Chapter 2 is divided into four sections. The first part provides an overview of the physiological characteristics of the circulatory system, the heart and the condition of interest: heart failure. The second section expands on the use of mechanical circulatory support devices as a treatment option for patients with end-stage heart failure, along with a brief explanation of current technologies, and the state of the art of left ventricular assist devices. And the last section explores mechanical approaches used in LVAD design, testing, and optimization. Chapter 3 describes the methods and approaches used to virtually characterize the performance of the pump. Chapters 4 and 5 discuss the results of both studies and the significance of findings in view of current limitations, and suggested future work for the project.

Chapter 2

Literature Review

This chapter provides an overview of the physiological characteristics of the circulatory system and the heart. VADs being the alternative treatment to heart transplants are discussed, and heart failure is introduced. The limitations and expectations of heart pump designs were explored to identify current design issues faced and future developments. This will lead to the discussion of adverse events after VAD implantation relating to blood damage. The history of the experimental setup to investigate blood damage is established, while CFD analysis is used to have a comprehensive virtual visualisation in the flow field of a real system. Toward the end, it described an insight into fluid dynamics stresses and the effects of flow pulsatility inside the heart pump.

The sections of text from this publication [1] which are in the thesis are in section 2.4 in Chapter 2. For my study, the fluid dynamic stress threshold for blood damage needed to be defined. The numerical values found in the literature and applied were stated repeatedly in my thesis in the literature review, methodology and results, but also mentioned in my publication.

2.1 Cardiovascular Physiology

2.1.1 Circulatory System and the Heart

The circulatory system has the function of transporting nutrients (examples are amino acids and electrolytes), oxygen supply, hormones and blood cells, alongside waste and carbon dioxide to all parts of the body. This helps to provide the body with nourishment and maintain homeostasis. And, the heart is the main mechanism that drives the blood throughout the circulation.

The heart is an organ that consists of two muscular pulsatile pumps that work in series. The same amount of blood needs to overcome high systemic resistance in the left ventricle to push blood through systemic circulation (movement of blood from the heart, to the body, and back to the heart); Whereas the right ventricle serves the pulmonary circulation (movement of blood from the heart, to the lungs, and back to the heart) which have lower pulmonary resistance hence low pressure. In a normal heart (**Figure 2.1 B**), heart muscles relax and both ventricles are first filled with blood from the atrium during the diastole process. This happens when the pressure in the ventricle drops below the atrium's level and the atrioventricular (AV) valves open. The AV valve in the left ventricle is the mitral valve, and consequently, the valve in the right ventricle is the tricuspid valve. During systole, contraction of heart muscles causes the ventricles to pump out about 60 to 80% of the blood and the AV valves to close [10]. The aortic valve and pulmonary valve open under high pressure exerted during systole leading blood to the aorta and pulmonary artery respectively.

2.1.2 Heart Failure

Heart failure (HF), often referred to as Congestive Heart Failure (CHF), is a common form of Cardiovascular Disease (CVD). It's a condition that describes the heart's incapability of pumping sufficient blood supply to the whole body, fulfilling body tissues' metabolic needs. HF is unlike myocardial infarction (MI) where part of the heart muscle dies, and it is neither like a cardiac arrest where the heart's mechanical function ceases. HF occurs following a sudden myocardial infarction event or because of chronic degradation of the cardiac structure or function. There are two types of HF in **Figure 2.1 (B)**: systolic dysfunction

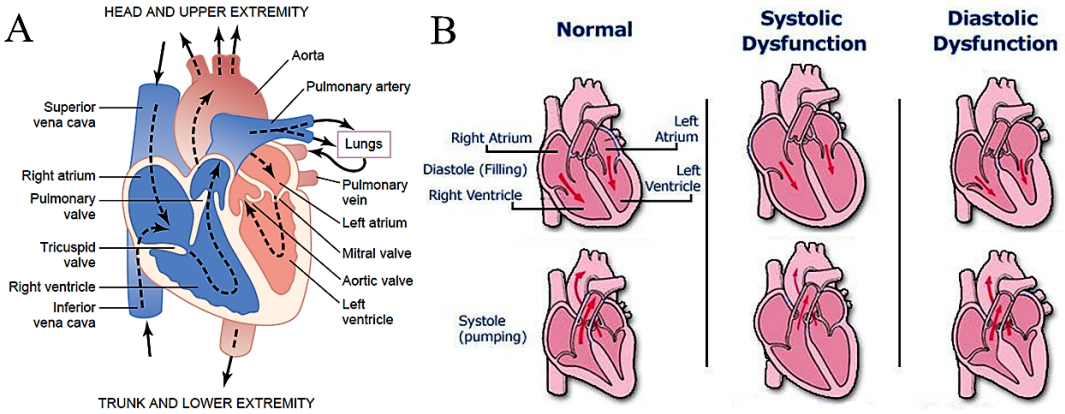

Figure 2-1: A. Schematic diagram of the heart. The dotted lines represent the flow pathway of blood [11]. Blood enters the heart from vena cava for right heart and from the pulmonary vein for left heart. Blood gets pumped out of the heart from pulmonary artery and aorta; B. Pathophysiology of heart failure from normal to manifestation of systolic and diastolic dysfunction.[12]

which is the impaired discharge of the heart, and diastolic dysfunction which is impaired filling of the heart. This is due to ventricular dysfunction which leads to inadequate perfusion and circulation pressure of the heart, resulting in breathlessness and fatigue. Blood is backed up from the veins to the heart and it becomes congested in the tissues. The fluid retention causes weight gain, leg swelling (oedema) and congestion in the pulmonary system [13].

A presentation of the normal and abnormal cardiac cycle can be plotted through a real-time pressure-volume (PV) loop as shown in **Figure 2.2**. For individuals with systolic dysfunction, the ventricles of the heart are enlarged which is caused by the deposition of scar tissues from inadequate blood flow (ongoing ischemia or myocardial infarction). The heart muscle is weakened and the loss of contractibility causes less than 40 to 50% of the blood to be pumped out of the heart [10]. As for diastolic dysfunction, heart muscle diseases such as hypertrophic cardiomyopathy and amyloidosis cause the heart muscle to stiffen by thickening the ventricle wall through abnormal cell deposition or inflammation [14]. The ventricles pump out about 60% of the blood but the initial volume may be lower than normal as the heart is filled with less blood. As a result, reduced cardiac output and constant strain on the heart cause chronic HF.

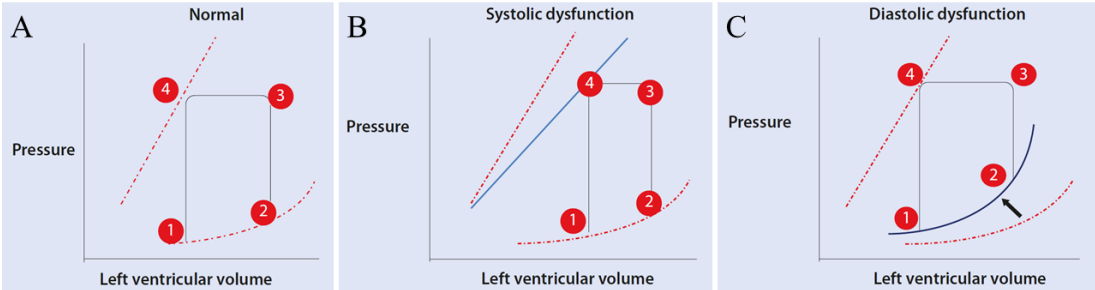

Figure 2-2: Left ventricular pressure-volume loops in individuals with: A. Normal heart function; B. Systolic Dysfunction; C. Diastolic Dysfunction. The numbers represent stages of the cardiac cycle of the left ventricle. (1-2) Filling; (2-3) Contraction; (3-4) Ejection; (4-1) Relaxation.[14]

2.1.3 Ventricular Assist Devices as Alternative Treatment

HF affects 26 million people worldwide, and its incidence is growing in the UK [15]. More than 500,000 people in the UK have heart failure and there are around 100,000 deaths each year [16]. HF is expensive to treat and medical professionals have tried to manage the condition through the application of drugs and pacemakers. But in the worst cases, patients need a new heart which makes heart transplants remain the gold standard treatment. Due to the limited number of donor's hearts, and the costs involved, less than 200 heart transplants are performed in the UK each year [17]. There were only 267 people on the heart transplant waiting list in the year 2015 - 16 and only 160 heart transplants were carried out [18]. Thus VADs became the therapy of choice for end-stage heart failure patients to help bridge this gap.

MCS is a good secondary option for patients with HF who are ineligible for heart transplants, offering improvements to the survival and quality of life of patients. Not all hearts that are offered for donation can be used. For example, in the year 2021, 134 hearts were not used for organ donation because the donor was too old [19]. This causes implant rates of MCS such as LVAD to have steadily increased in the last decade. Many studies assessing LVAD outcomes use randomised control trials (RCT), the values may not be generalised due to restrictive RCT selection criteria [20]. Survival estimates following an LVAD implant range from 56% to 87% at 1 year and 43% to 84% at 2 years; most do not report survival rates beyond 2 years [21, 22]. More LVAD studies are needed to assess longer-term sur-

vival, costs and complications, as this has limited cost-effectiveness evaluations.

Current LVAD designs are relatively easy to implant, have high durability and are small in size. Generation of LVAD designs can be classified based on their output characteristics and inner mechanisms. Firstly, LVADs can be categorised anatomically by the placement of the implant intracorporeally (abdomen or pericardial space) or extracorporeally. They also can be differentiated by flow fields and can either be a pulsatile flow pump or a continuous flow pump with an axial or centrifugal pump design. LVADs are generally suited for any of the three main methods of treatment: Bridge to Transplant (BTT), Bridge to Recovery (BTR) and Destination Therapy (DT), regardless of the patient's life expectancy. Recently, Bridge to Candidacy (BTC) was also introduced as patients are put on a waiting list for heart transplantation or Bridge to Decision (BTD) till a decision for therapy is made.

2.1.4 VAD Design and Classification

Emerging in the late 1960s, visionary people started to devise ways to artificially assist the heart. It started with the expandable chamber by Dr Kantrowitz (1963) [23], followed by the gas-energized synchronized left ventricular bypass pump by Dr DeBakey (1966) [24]. This originated the field of innovative cardiac surgical procedures for the development of mechanical assist devices. Since then, many kinds of MCS have been developed to assist the heart, such as intraortic balloon pumps (IABPs), and the Total Artificial Heart (TAH). Then, the first successful bridge-to-transplant LVAD procedure was performed in 1978 [25]. From there until the late 1990s, the evolution of VADs began and this is the latest technique which gave a promising long-lasting therapy for patients with chronic HF. VADs are slowly becoming the gold standard treatment for advanced heart failure and the most common type of MCS for long-term implantation [26].

The first generation of VADs were positive displacement pumps with pneumatically or electrically driven membranes, paired with artificial valves as inlets and outlets [27]. Early development of pump design attempted to replicate the physiological pulsatility of the flow of the native heart. The moving membrane expands to allow pump volume or diastolic phase filling and is compressed to

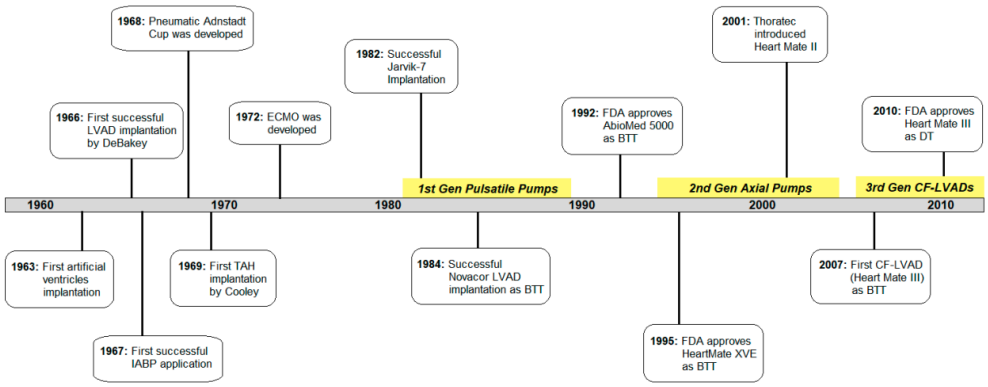

Figure 2-3: Timeline of important milestones of MCS development history [27]

eject blood during the systolic phase (**Figure 2.4 A**). Initially, these types of MCS devices functioned as BTT to stabilise the patient's heart condition, then the implementation of VADs at the end-stage of HF patients helped improve the organ's function making it possible to be listed again for a heart transplant. The main drawback of the design was that the degradation of the artificial valves used to regulate unidirectional flow risks causing blood cell trauma in the VAD [28]. Other drawbacks included the largeness in size (the pump is implanted extracorporeally), mechanical failure of the diaphragm due to its complicated drive mechanism and constant moving parts [29]. Examples of the first-generation pumps are the HeartMate XVE, Abiomed AB5000, Medos HIA-VAD, Berlin Heart EXCOR and Thoratec PVAD.

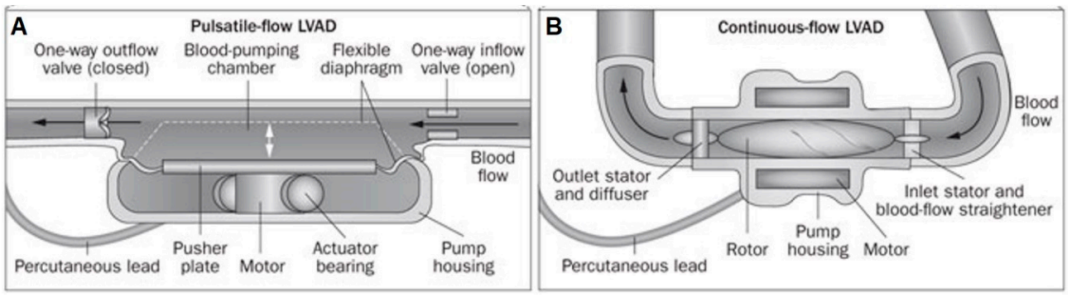

Figure 2-4: The first generation pulsatile-flow pumps. A. replicated the native cardiac cycle using a diaphragm and unidirectional artificial heart valves, while the second generation continuous-flow pumps. B. integrated a valveless axial pump designed to rapidly spin a single impeller [27].

In the second generation of VADs, rotary centrifugal and axial flow pumps provided continuous flow, had a relatively small design, fewer moving parts, high durability and low power consumption [30]. An operating continuous pump uses a high-speed rotating impeller to build up internal pressure to drive blood from the inlet port to the outlet. Moving components exposed to repeating forces, like membrane and artificial valve, were replaced with impellers and it has greatly improved the performance and lifetime of VADs (**Figure 2.4 B**). The engineering application of magnetic levitation on positioning the impeller increases the efficiency and durability to a survival rate minimum of five years [31]. Since then, the US Food and Drug Administration (FDA) approved that the HeartMate 2 (HM 2) rotary continuous axial flow pump can be used for BTT or DT treatment since the year 2008 [32]. The disadvantage of this generation of VADs was that the design was only suitable for intrathoracic implantation, even with the reduction in size from the first generation. With a magnetic bearing embedded in the housing, high shear force and vibration of the pump could cause problems on the components in the long term such as gastrointestinal bleeding, blood damage and reduced lifespan of the device. However, it is still the most commonly available for clinical usage with the selection of either a centrifugal pump (for example, Gyro pumps) or an axial pump (MicroMed Debakey and HeartMate 2).

2.1.5 New Rotary Blood Pump Technologies

With a further size reduction, the third generation of VADs was introduced with fewer mechanical contacts within the pump and a strong magnetically driven impeller. The implantation of third-generation pumps can be in the pericardial space. The removal of seals and bearings in contact with blood prolonged the lifespan of the VADs. The impeller is supported by hydraulic forces and magnetic suspension, keeping it levitated from the housing to reduce mechanical wear and stress on blood cells. The goal was to create a pump for all types of treatment (BTT or BTR or DT) and no wear-out is expected to increase the durability of VADs by 10 years [31]. Examples of third-generation pumps available include Thoratec HeartMate 3, DuraHeart, INCOR, Medtronic Miniature VAD (MVAD) and HeartWare HVAD (HVAD).

Medtronic acquired Heartware International Inc. in the year 2016, the developer

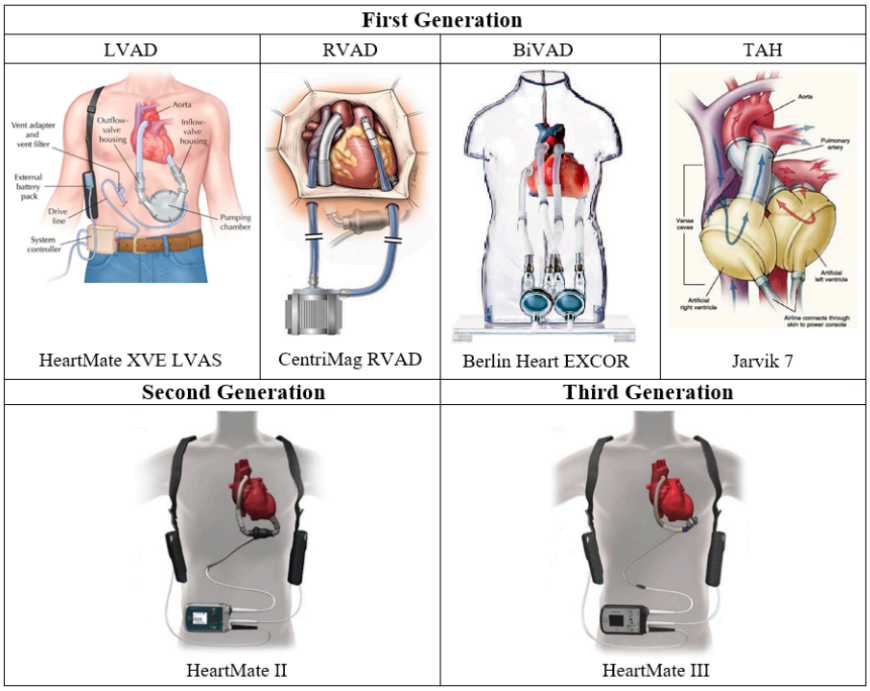

Figure 2-5: Examples of first, second, and third generation mechanical circulatory support devices[27]

of the HVAD system and the next-generation MVAD system. The system was approved by the FDA in 2012 for implantation in patients with severe heart failure. The other was Thoratec which controlled 60% of the market under Abbott. While Heartmate 3 can be surgically implanted below the diaphragm in the abdomen, Heartware HVAD is a lot smaller, which allows intrapericardial placement and thoracotomy implantation. However, over the last few years, HeartWare encountered some setbacks. Past studies have shown that such pumps encountered clotting-related side effects 4% of the time [33]. In reality, 3 of the first 11 patients in Europe who got the device in a clinical trial experienced the problem causing the company to close down the trial in 2016 [33].

On June 3, 2021, Medtronic stopped the sale and distribution of the HVAD system given the increased risk of mortality and neurological adverse events in patients using the device, and a malfunction where the device may fail to restart [34]. Both problems may lead to serious injuries or death. Both Medtronic and the FDA specifically cited Abbott's HeartMate 3 to be the primary alternative device for HF patients [35]. The FDA approved the device based on the

MOMENTUM 3 clinical study, which was the most extensive LVAD study with 294 patients needed for short and long-term cardiac support [36]. With an 82% two-year survival rate, HeartMate 3 demonstrates high event-free survival, low adverse event rates and improved quality of life.

Based on the INTERMACS Report done by Kirklin *et al*, more than 50% of medical complications after VAD implantation relate to blood damage [37]. The main function of blood in the circulatory system is to act as the medium of transport for oxygen, toxic waste and blood cells. Thus, it is important to understand blood rheology and non-physiological device-blood interaction. These are the crucial steps to understanding a pump that causes minimal blood damage.

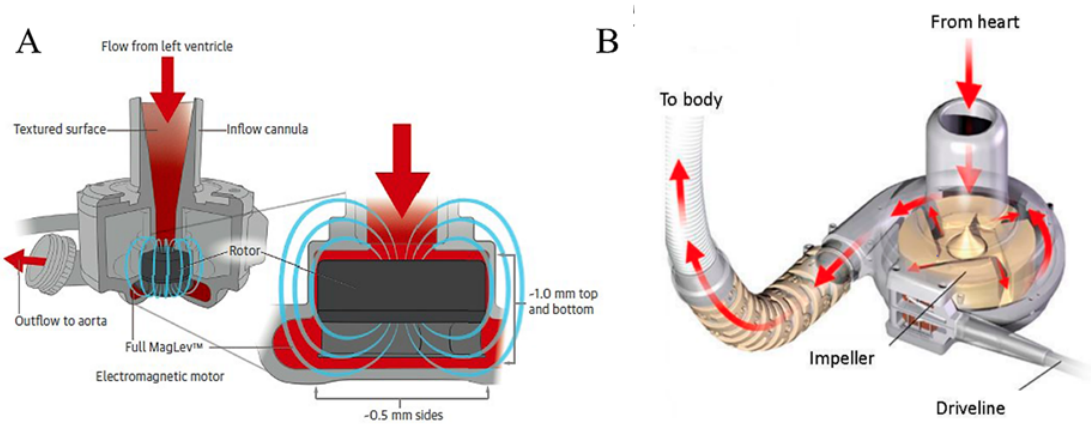

Figure 2-6: New rotary bloop pump technology. A. Thoratec HeartMate III [38]; B. HeartWare VAD (HVAD) [39].

2.2 Non-physiological Blood Damage in VADs

2.2.1 Blood Properties

The main cellular components of blood are as observed in **Figure 2.7**. First, red blood cells (RBCs), also clinically known as erythrocytes, made up approximately 40 - 50% of the total blood composition. Their functions include transporting oxygen and carbon dioxide for gaseous exchange, delivering nutrients and hormones for body tissues' metabolic reactions and removal of toxic waste. RBC have a diameter of 8 μm and a thickness of 2 μm. In each RBC, there is a glob-

ular molecule known as haemoglobin which helps bind gaseous molecules such as oxygen for transport. Next, the second most abundant blood cell in the fluid is white blood cells (WBCs), otherwise known as leukocytes. While RBCs take up 40 - 50% of the blood volume, WBCs take up about 4%. There are different types of leukocytes, varying in size and function. But, they all have one main role which is to act as defenders of the body's immune system against infectious diseases and foreign invaders. Unlike RBCs, WBCs are larger and range from sizes between 7 to 15 μm in diameter.

Lastly, platelets are cell fragments that form a clot with other clotting factors to construct a 'plug' to prevent bleeding when a blood vessel is damaged. They occupy 0.01% of the blood and are a size between 2 to 3 μm in diameter. When unactivated for clotting, they have a biconvex disc structure as they are fragments of cytoplasm. When activated, they become more of an amorphous form with projecting finger-like structures to adhere with other clotting factors. These blood cells are suspended in a medium known as plasma which makes whole blood a suspension. Plasma is 90% made up of water and other components such as minerals, nutrients, enzymes and proteins and it functions to maintain blood pressure and regulate the body's temperature. It is the single largest blood component, comprising about 55% of the total blood volume.

While VADs have benefited many patients, they have the potential to benefit even more if blood cell damage problems can be eliminated or reduced. This project will focus on two of the blood elements: RBCs and von Willebrand factor (vWf). These have been chosen because the deformation of the elements (either cells or molecules) is a predominant factor in their destruction.

In terms of rheology, blood behaves as a non-Newtonian fluid. However, the assumption that blood can be simplified to incompressible Newtonian fluid is widely used in CFD simulations to analyse LVAD-blood interaction. In the case of LVADs, blood viscosity is considered to have a constant value at shear rates above the normal physiological range ($> 100\ s^{-1}$) [41]. Dynamic viscosity (μ) of blood ranges between 3.23 x 10^{-3} Pa s to 4.20 x 10^{-3} Pa s and it varies depending on the hematocrit levels [42]. As for composition, blood is an inhomogeneous, anisotropic fluid that consists of a suspension of blood cells and plasma. In rotary

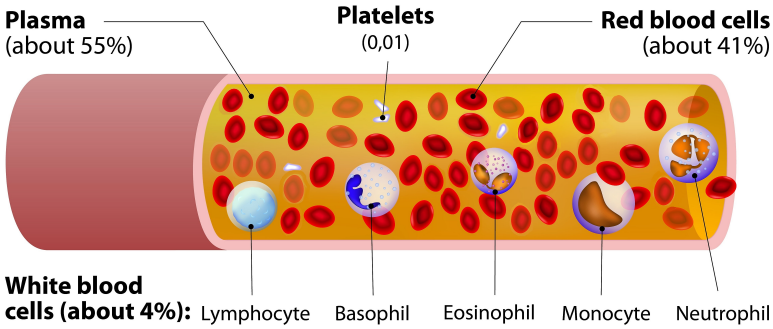

Figure 2-7: Overview of different cell components present in the composition of whole blood [40].

blood pumps, there are many factors influencing the damage of blood components and thrombus formation.

Haemocompatibility of blood-contacting surfaces inside the blood pump and heat generation at contact bearings are two important factors in relation to blood damage. However, with the incorporation of sophisticated biomaterials and the advent of hydrodynamic and magnetic levitation bearings, these factors have become less important. The remaining significant factor is the fluid dynamics stress. Hence in this study, the focus is on the effects of the non-physiological flow conditions of rotary blood pumps. Blood cells' sensitivity to elevated shear stress, flow turbulence and prolonged exposure time between blood cells and foreign surfaces are still unknown, despite the amount of extensive research carried out in the past decade. Hence, the known damaging effects on blood components will be introduced in these sections.

2.2.2 Destruction of Erythrocytes

At a low shear rate, erythrocytes aggregate to form large secondary particles with rod-shaped stack structures called rouleaux [43]. Erythrocytes have different types of movement under higher shear rates, including flipping, tumbling and tank treading [44]. As the shear rate increases, the rouleaux disintegrate to form smaller structures and blood is treated as a Newtonian fluid. At higher shear stress, cells began to lose their biconcavity at 50 Pa and the majority assumed an ellipsoid shape when shear stress applied exceeded 150 Pa [45].

Above a certain mechanical shear stress, the RBC's membrane is stretched to critical stress or strain which then causes either the membrane to rupture or become porous and the RBCs deformation is irreversible [45]. This phenomenon is known as haemolysis, resulting in the release of haemoglobin into the blood plasma. Besides the magnitude of shear stress, it is found that haemolysis also depends on the increased duration of exposure in the pump. At long exposure time (4 minutes), the RBCs were sheared up to 250 Pa where the cell was elongated along the direction of flow [45].

Several blood damage experiments have been done to investigate the effect of shear stress on the blood which will be discussed in **Section 2.3**. The amount of haemolysis can be described through power law function of shear stress magnitude and exposure time. The function was derived through a series of investigations through Couette flow devices from different research groups [46–49]. The power law function is the haemolysis index and it represents the percentage of cells which were haemolysed as a function of exposure time (t) and shear stress (σ):

$$\text{Haemolysis Index (HI)} = \frac{\Delta Hb}{Hb} \times 100 = Ct^a\sigma^b \tag{2.1}$$

Where C = 3.6210^{-5}, a = 0.785 and b = 2.416 are empirical constants. HI is also the percentage difference of plasma free haemoglobin (PFH), Hb after blood has a single pass through the device.

2.2.3 Platelets Activation and Apoptosis

Blood clotting is related to three factors which are known as Virchow's triad: surface nature, blood condition and local flow conditions [50]. In combination with shear stress, this initiates adhesion of platelets, platelet activation and coagulation cascade to form blood clot or thrombus. There are two main theories behind the mechanism surrounding stress-induced activation of platelets and they are: 1) shear stress effect on platelet receptors actively binding to vWf; 2) stored agonists was released into plasma to react with platelets and RBCs at high shear stress through mechanical lysis. Therefore in normal homeostasis, platelets adhered and are activated when in contact with thrombogenic surface such as an injured wall vessel.

At low shear period, the deceleration of flow allows the interaction between collagen and integrin $\alpha 2\beta 1$ receptor (transmembrane protein) to form a strong bond. Platelet aggregation occurs to form thrombus to adhere to thrombogenic surfaces of medical devices. This can happen even when flow in devices is slow, stagnant or recirculating [51]. At high shear rates, platelets release procoagulant agonist such as thrombin and serotonin under mechanical shear stress to bind with vWf via GPIbα receptor [52]. An example would be the study carried out by Hellum *et al*, producing a shear stress-exposure time threshold plot which defined the locus of points where platelets become activated [53]. In addition to activation, an in-vivo study done by Bakir *et al* found that at shear stress 6.5 Pa with a long exposure time of 15 minutes showed a significant reduction in platelet count [54]. Leytin *et al* also discovered platelet apoptosis when caspase 3 activation and mitochondrial transmembrane potential depolarisation was found in plasma when shear stress ranging 11.4 to 38.8 Pa for 90 seconds was applied [55].

2.2.4 Degradation of Von Willebrand Factor

In brief, vWf are large multimeric glycoproteins that perform a critical role as they exist in blood plasma: they act as a binding agent for platelet adhesion and aggregation under high shear conditions. In normal circulation, the large polymer is converted after being secreted by endothelial cells in plasma into series of multimer via proteolysis [56]. At critical shear stress, the large multimers are unravelled, exposing its cleavage sites which enhances its susceptibility to proteolysis. This process occurs normally in circulation with wall stress ranging between 0 to 5 Pa. However it is thought to be accelerated in patients with aortic stenosis [57], as well as patients with implantable rotary blood pump who have acquired von Willebrand disease [58]. The decrease in vWf in patients reduces platelet adhesion and aggregation that cause patients to be prone to bleeding excessively.

Shear stress effect on the degradation of vWf multimer structure has been studied in-vitro. The enhanced cleavage of vWf multimer can be found at a shear stress above 3.5 Pa by Siedlecki *et al* who uses a rotating disk system for applied shear effect [59]. Using flow through capillary tubes, Tsai *et al* showed a reduction in high molecular weight multimers in aortic stenosis patients at approximately 5

and 7 Pa [56]. And lastly, shear stress threshold was calculated by Di Stasio *et al* to unfold vWf exposing its functional domain for cleavage at more than 10 Pa of stress [60].

2.3 Experimental Model for Blood Damage

As discussed in **Section 2.2**, the range of haemodynamic stresses for different blood components are determined and detailed experimental models can be constructed to understand and analyse the amount of damage done in different LVADs. In addition, hydrodynamic experiments are constructed to study the flow fields of VADs and investigate fluid stress distribution based on pressure head and volumetric flow. Experiments for flow field studies such as particle image velocimetry (PIV) are able to provide two dimensional real flow fields with helical flows, backward flows and vortices. While, closed loop experiments provides real time data for blood damage comparison against fluid flow field. This also can be used to measure the amount of blood damage such as haemolysis and vWf cleavage that occurs in LVADs. Fluid stresses and exposure time can be varied and applied in these experiments to induce blood damage for research.

2.3.1 Hydrodynamic Analysis

Understanding and having the ability to predict fluid dynamics within the pump is critical to determine the pump's performance and efficiency. The nature of flow conditions experienced by blood within these type of devices can be analysed with optical techniques such as PIV, laser Doppler velocimetry, oil dot flow visualization and paint erosion techniques. In addition to the complicated 3D design, transient flow effects are caused in the pump due to the interaction between impeller blades and fixed pump geometry with time-varying flow caused by pulsating left ventricle. Although the pump operates at specific operating conditions, the flow rate is dependent on the ventricular contraction that varies the inlet pressure of the pump. Increased efforts to investigate flow fields ranging from different flow rates have created an awareness in researchers that the flow rate through the pump varies during each heartbeat, despite efforts in maintaining constant rotational speed.

The use of PIV technique to study fluid dynamics of blood pumps is common. PIV measures instantaneous velocity field using light scattered from particles seeded in the fluid within an illuminated plane of fluid field as shown in **Figure 2.8 A**. The advantage of using this technique as opposed to laser Doppler velocimetry which measures from a single point is that multiple points on illuminated plane can be measured simultaneously. The PIV flow field experimented at 1500 rpm was clearly turbulent so the CFD solution computed with a k-ε turbulence model showed a good agreement with the velocity field computed [61]. Assumptions made for maximum shear stress in the flow field of VADs often estimate analytically that it occurs based on the impeller radius, rotational speed and clearance gap. These however assume a linear velocity gradient between the blade tip and housing and in reality, the gradient is steeper at the wall of the housing [61]. Steady flow conditions were applied to PIV and simulated with a computational model while ignoring the pulsatile characteristic of a time-dependent flow.

With that said, turbulence is a characteristic of velocity fluctuations and it depends on the frequency of flow disturbance. In most cases, hot and cold wire anemometers are used to characterize turbulence in a fluid flow (**Figure 2.8 B**). These are based on the convective heat transfer from a heated wire to the surrounding fluid, the heat transfer is directly related to the fluid velocity. By using very fine wires and adapted electronics, one can measure velocity fluctuations down to fine scales and at high frequencies. Although thinner wire provides more accurate measurements, this decreases the robustness of the probe. The number of wires dictates the number of dimensions measured (1D, 2D or 3D). The characteristics of the flow will impose the type of wire to be used. An experiment by Chua *et al* uses air as the medium for the present study instead of blood to observe the flow fields in the centrifugal pump [62]. The highest wall shear stress was found at roughly 44 Pa which is high enough to disrupt RBC morphology and activate platelets. These findings explain the occurrence of haemolysis at low level of stress in the clearance gap of VADs.

The last two techniques involve applying liquid colouration on the blades of the impeller to visualise flow patterns within the pump. The effects of different operating conditions and impeller design on the fluid dynamic and hydrodynamic performance were studied. Both oil dot and paint erosion methods allowed the

analysis of disturbed flow within the tight flow passage between the impeller blade and the housing of rotary blood pumps. The tight gaps were imperceptible with light sheet methods in PIV. For the oil dot method, a viscous droplet of coloured oil was applied to the surface of the impeller and shear stress adjacent to the surface caused streaks to appear in relation to the flow direction and magnitude [63]. A clear visualisation of the fluid dynamics of the impeller design can be seen in **Figure 2.8 C**. As for paint erosion, high-viscous and water-insoluble oil paint coated the pump components excessively and was partially washed away by local flow at the beginning of the operation [64]. The remaining thickness of the surface paint corresponds to the average wall shear stress acting on the surface. In terms of analysis, bad washout areas were considered critical regions for thrombosis and haemolysis to happen and in this way, high-shear stress regions for blood damage were identified. And from **Figure 2.8 D**, overall good agreement of CFD and experimental results was observed which includes the location and direction of the maximum wall shear stresses alongside the presence of recirculation zones on the pump stators [64].

2.3.2 Blood Damage Analysis

After obtaining quantitative data for flow fields in rotary blood pumps, in vitro performance tests were constructed in order to characterise hydrodynamic performance and blood damage for comparison. High shear stresses regions predicted through the velocity field should correspond to the normalised index of haemolysis (NIH), obtained from variation of PFH measured at the end of a closed mock loop experiment, clinically known as haemolysis testing. The experimental setup is as shown in **Figure 2.9 A** and it is planned according to ASTM Standard Practices F1830 and F1841 guidelines for haemolysis testing [65]. The protocol is standard for testing various types of blood shearing devices and involves five steps: collection and preparation of blood, mock loop setup, a six-hour test, PFH measurement and NIH calculation. Based on Restle's group, the mock loop was used to perform pre-clinical investigations of LVAD-associated vWF degradation [66]. Paired with a HeartMate II, blood circulated through closed-loop demonstrated a similar profile of degradation of large vWf multimers and an increase in fragmentation of vWf strands. The amount of vWf degradation can be char-

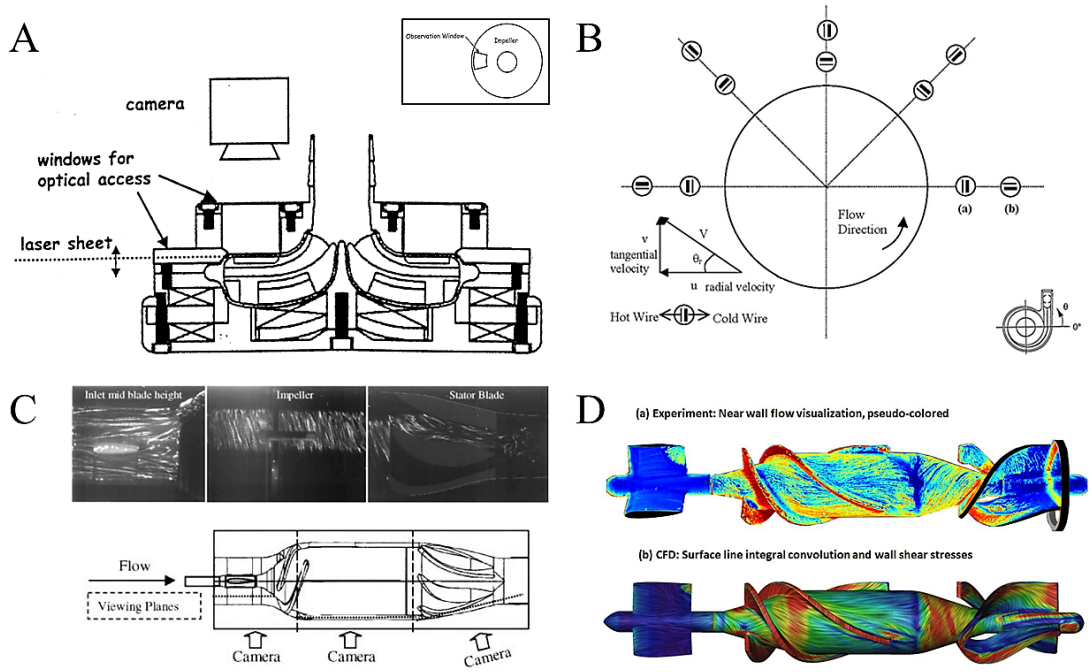

Figure 2-8: A. Setup for PIV experiment with the prototype CFVAD3 pump with a camera located by the window to capture light scattering by seeding particle [61].; B. Orientation of hot and cold probes for measuring tangential and radial velocity at different position of the pump for turbulence flow detection [62]; C. Flow patterns detected at the position on rotating impeller with a synchronised stroboscope to illuminate oil streak growth [63]; D. Comparison of near surface flow between paint erosion experimental method and CFD-derived [64].

acterised through electrophoresis and immunoblotting.

Couette flow blood shearing devices are used to produce shear-induced haemolysis by varying exposure time. This is to evaluate the haemocompatibility of different pump designs with varying operating conditions to study the range of shear stresses caused in the flow pathway. Wurzinger and Giersiepen were the first experimental research group to use such a device with resuspended human RBCs under the conditions $\tau < 255$ Pa and t < 700 ms [46, 47]. Heuser and Opitz used the same device but with porcine blood at similar exposure time (t < 700 ms) measuring higher shear stresses ($\tau < 700$ Pa) [48]. A faulty fluid seal was assumed to be the cause of overestimated overall blood damage. Then in year 2003, Paul *et al* conducted an experiment with a newly-sealed Couette shear device at exposure times from 25 ms to 1250 ms and shear rates ranging from

30 Pa up to 450 Pa [49]. A seal fluid is pumped vertically into the device to prevent secondary blood damage effects while blood is pumped axially as shown in **Figure 2.9 B**. As a result, evident haemolysis was observed at shear stresses more than 425 Pa and at exposure time more than 620 ms. Last but not least, the most recent Couette-type blood shearing device was developed by Zhang *et al* based on commercial rotary VAD designs [67]. The results obtained show a gradual increase of haemolysis starting from 150 ms with an increase in shear rate rather than a sudden onset as displayed by Paul's study. the difference in results is likely to be the different animal blood used in the mock loop experiment, which were porcine blood (Paul *et al*) and ovine (Zhang *et al*).

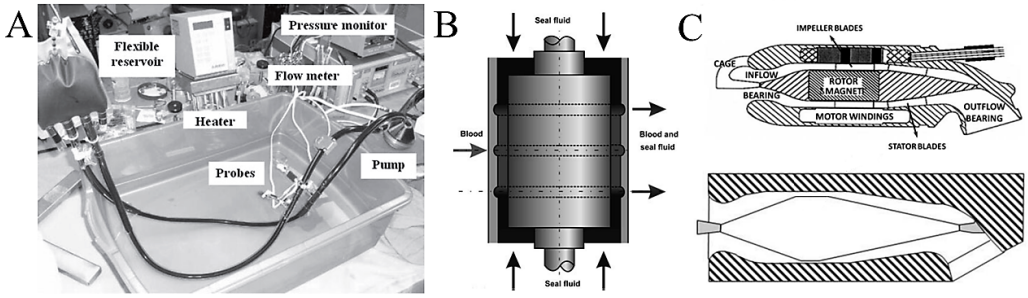

Figure 2-9: A. Mock loop circuit used during haemolysis testing [65].; B. Schematic diagram of Paul's Couette flow shearing device with the newly-designed seal [49]; C. (Top) Cross-section of the adult Jarvik 2000 blood pump, (Bottom) Schematic diagram of Zhang's design of an axial rotary pump [67].

2.3.3 Fluid Dynamic Stresses Analysis

After defining threshold stress values for blood damage, there has been some research into the differing effects of shear and elongational stress on the blood components. Lee *et al* measured the deformation of RBCs in both shear and extensional velocity fields [68]] using a Couette flow device and hyperbolic converging microchannel respectively (**Figure 2.10 A**). They found that cells deformed more at lower elongational stress compared with shear stress: the deformation index was 0.51 at 3.0 Pa in extensional stress compared to 0.29 at 3.0 Pa in shear stress (**Figure 2.10 B**). Down *et al* extended the work calculating the velocity fields to conclude that they found no threshold shear stress for haemolysis and

that extensional stress appeared to be a critical parameter [69].

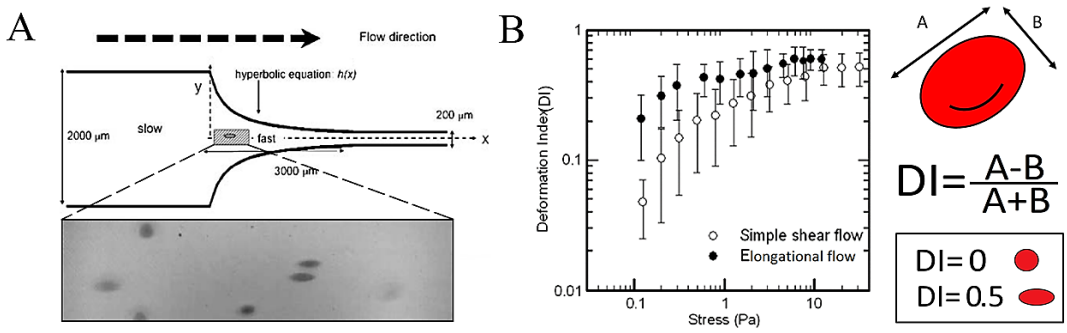

Figure 2-10: A. Hyperbolic converging microfluidic channel design. The elongational flow is induced by velocity difference when cells pass through the converging region [68]; B. Plot from Lee *et al* shows experimental data for RBC deformation occurring at both shear and elongational flow. It also shows that elongational flow produces a higher deformation index as compared to shear flow.

2.4 Numerical Model for Blood Damage

Empirical models are generated and validated against the experimental data obtained. This is to establish a relationship between flow field and fluid stresses which contributes to blood damage. Among the types of blood damage, haemolysis modelling is the best studied. If current modelling of blood constituents are extended, universal models of blood damage can be used to capture underlying haemodynamic stress mechanisms for any blood cell.

2.4.1 Red Blood Cells

To calculate haemolysis, the most common practice is to used the power law equation developed by Giersiepen *et al* [47]. There are two approaches to modelling haemolysis (RBC damage) and they are either a stress-based method or a strain-based method. The first approach forms an empirical relationship between stress and haemolysis, based on experimental measurements of haemolysis in a uniform shear stress condition. The power law equation is implemented into CFD calculation used for post-processing in Eulerian or Lagrangian approach. With

an Eulerian approach, Garon and Farinas integrated the haemolysis index over cells in a specific numerical space and found a good agreement with published and own experimental data [70]. Arvand *et al* incorporated pressure head and high stress fraction into his Eulerian stress-based equation and obtained their constants experimentally [71]. Chen *et al* also used the linearised power law model to compare the haemloysis index under pulsatile flow condition [72]. Although pump-modulation genrates large variations in stress field, his findings suggest that pulse modulated CF-VAD may be sufficient to restore vascular pulsatility without risking blood trauma.

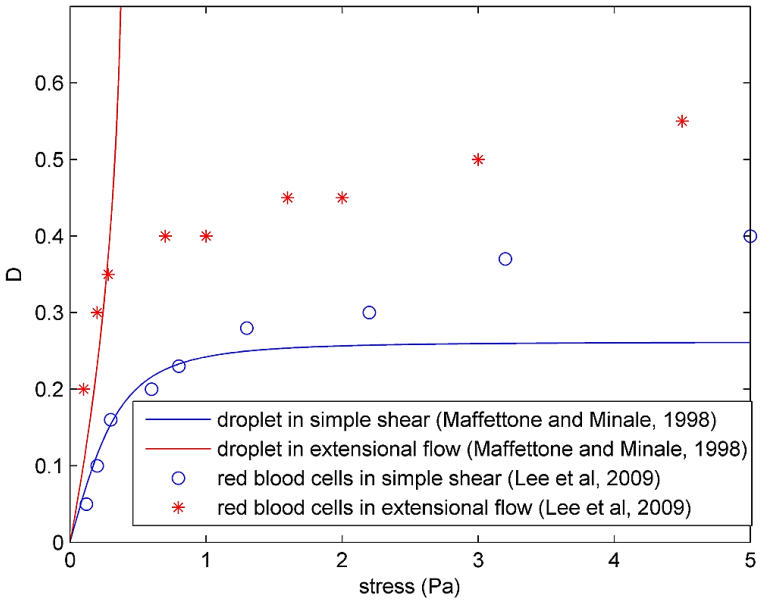

Figure 2-11: Comparison of the steady state deformation of an oil drop from the model by Maffettone and Minale (1998) with the experimental measurement of the deformation of a red blood cell measured by Lee *et al* [68]. D is the Deformation Index.

Second approach is the strain based method and this method uses analogy of oil drops. The deformation of a droplet of an immiscible fluid immersed within a second fluid can be calculated. Maffettone and Minale used this approach to represent RBC deformation [73]. They were the first to propose a method for calculating the transient deformation of the oil drop in a general shear field. To make the droplet analogous to a RBC, the surface tension was adjusted to give

deformation indices of the correct magnitude when compared with the experimental data for RBCs by Lee *et al* [68] as shown in **Figure 2.11**.

The difference in the deformation index between the oil drop and the RBC can be explained by the structure of the RBC. The biconcave disk shape of the RBC results in a large surface area to volume ratio meaning the cell deforms differently to the droplet at high stress. However, the analogy serves to illustrate how the two different types of velocity field have differing effects on the cell/droplet deformation. Despite this discrepancy Pauli *et al* used the oil drop model of Maffettone and Minali to investigate haemolysis in a centrifugal VAD, although it is unclear how accurate their predictions are as they do not compare with any experiments [74]. It is clear that a more accurate model is still required. The advantage of the strain-based models is that it accounts for the viscoelastic deformation of RBCs.

2.4.2 Von Willebrand Factor

As compared to the well-established models of RBCs studies, there are not many numerical models for the unravelling and cleaving of vWf. The first models were developed by Alexander-Katz [75]. They used techniques from polymer physics by studying the movements of vWf in a flow field with Brownian dynamics. The vWf blood glycoprotein is constructed of dimers and the modelling of vWf is represented as spheres connected to adjacent dimers by springs. These springs represent the scissile bond between vWf dimers which causes the vWf multimer to form a globule. Meanwhile, Huisman *et al* focused on the analysis of vWf cleavage in only shear flow. Based on the vWf models developed, he incorporated an instantaneous spring tension which mimics the force-responsive opening of vWf cleavage sites at a critical shear rate of 2000 s^{-1} [76].

The difference between shear and elongational flow effects on protein deformation are even more pronounced than those for cell deformation. Sing *et al* [77] performed coarse-grained molecular dynamics calculations to investigate the behaviour of von Willebrand factor (vWf) multimers in flow. vWf is a long molecule, up to 1000 μm in length [78]. When fluid dynamic stresses are low, the long chain molecule exists as a coiled globule, and in the presence of fluid dynamic stress, the globule unravels to reveal the long chain. The percentage extension is used to

quantify vWf deformation: $L/L_0 \times 100$ where L is the current length of the molecule and L_0 is the original length [77, 79]. Sing *et al* [77] found that a shear rate of 10^4 s^{-1} caused a 27 % extension of the vWf molecule but that an elongational rate of just 30 s^{-1} was enough to cause the same extension.

2.5 Concept, Goal, and Research Objectives

Based on the literature review, numerical models for blood damage should account for the differing relative contributions of shear and normal stress components. However, before proceeding to create such numerical models it was important to establish their necessity; that is, do rotary VADs create normal stresses? [1] Moreover, in reality, the flow through a VAD is pulsatile due to the beating heart [80]. Quantification of the fluid stress components based on realistic flow conditions is also ideal for accurate prediction in real blood-contacting device morphology. Therefore, the aim of this work was to quantitatively assess the magnitude and extent of normal stresses present in commercially available rotary VADs and compare that with the magnitude and extent of the shear stresses.

The research objectives are as follows:

- Perform CFD analyses on the two most commonly implanted VADs, the HVAD and the HeartMate 2, and then used the velocity gradients to calculate the magnitudes of normal and shear stress components.
- Carry out flow field investigations on the influence of flow pulsatility on flow properties such as wall shear stresses and deformation volumes.

This assessment is vital in determining the importance of further experimental investigations of the influences of normal stress on the blood components, and of creating numerical blood damage models incorporating the influences of realistic flow conditions.

Chapter 3

Methods

For this chapter, the methods reported were centred around fulfilling objective one as mentioned in **Chapter 1**. Sections of text from my publication [1] which are in the thesis are in section 3.1 and 3.2 in Chapter 3. Other publications which relate to the methodology created in this chapter by me for my paper and thesis were published in the abstract for the 23rd Congress of the European Society of Biomechanics [2] and BioMedEng18 Conference [3].

The construction, meshing, solver setting and post-processing of the HVAD model were done by me and as described in this chapter. In summary, the first steps involved post-processing point cloud data from a previous project [81] and converting it into a three-dimensional computer-aided design (CAD) model for simulations. This content was extracted directly from my paper [1]. The model was then imported into CFD solver (ANSYS CFX, ANSYS Inc, Canonsburg, PA, USA) to create a mesh for fluid domain discretisation. The discretisation error of the HVAD mesh is compared against flow fields and velocity profiles obtained from literature at specific regions of the FDA blood pump [82], mentioned in section 3.2.2. I used CFD to calculate flow fields in a centrifugal (HVAD) and an axial VAD (Heartmate 2). The geometry and mesh of the axial VAD were obtained from Molteni *et al* [83] previous work, hence the mesh construction was not detailed in this chapter. The velocity of the blood defined the reference frame, which I used to compute from the transformed strain rate of both stresses: normal and shear. In this chapter, most of the methodology has been published

in The International Journal of Artificial Organs in 2018 [1].

3.1 Geometry of the Flow Domain

Two commercially available rotary VADs were investigated: a centrifugal flow pump, the HVAD (Medtronic, formerly HeartWare, Miami Lakes, FL), as shown in **Figure 3.1** and an axial flow pump, the HeartMate II (Abbott Laboratories, Abbott Park, IL, formerly Thoratec Corp, Pleasanton, CA).

The HVAD was one of the most frequently used VADs and its small size allows implantation within the pericardium [84]. The main blood contacting components of the HVAD are an impeller with four wide blades, and a volute casing. In operation, the HVAD's impeller is suspended using hydrodynamic and magnetic levitation which maintains clearance between rotating and stationary parts. In this study, the impeller position was fixed so that the top hydrodynamic bearing gap was 20 μm and the bottom, secondary flow, gap was 180 μm, which is appropriate for the operating conditions used [85]. However, the exact position of the rotating impeller still remains unknown due to the hydrodynamic thrust bearings. Since this position could have a large influence on the stresses, particularly the shear stress in the secondary and tertiary flow paths, the position of the impeller was varied to assess the impact on stress calculations.

The HeartMate 2 (HM 2), has been implanted more times than any other VAD with over 20,000 implants to date [86]. Geometry of the HMII consists of a flow straightener, and an axial impeller and diffuser, each with three blades. The impeller is held in place by blood washed cup-socket pivot bearings [87] which were not explicitly modelled. There was a fixed clearance gap of 100 μm between the housing and the blades. To ensure fully developed flow at the entrance to the VADs, and to ensure the outlet boundary condition did not influence the flow within the VAD, the inlet and outlet tubes respectively were extended by at least 10 inlet radii when creating the computational fluid domain.

3.1.1 Scaling and Post-processing Point Cloud Data

Based on previous work [81], the point cloud of the HVAD was obtained by scanning the surfaces of the impeller and volute casing with a contact scanner (DS-10

Figure 3-1: The HeartWare HVAD device (courtesy of HeartWare, Inc.).

contact scanner, Renishaw, U.K.) at a 20 μm resolution. The point cloud data was saved as a stereolithography (STL) file format. STL file is described as a raw unstructured triangulated surface by the unit normal and vertices of the triangles using a three-dimensional Cartesian coordinate system. In other words, it is basically a dense mesh of triangles which were slices of a well-constructed solid model into a series of thin two-dimensional layers. Each layer was made up of multiple line segments with two end vertices. This output file can be applied to drive a stereolithography machine or other type of 3D printer which produces physical prototypes through layer-by-layer deposition.

Meanwhile, a solid CAD model consists of the least complex geometric entities which is ideal and stable for design-sharing purposes. The solid geometry can be shared without degradation in a solid format (STEP file). It provides parametric, history-based models and assemblies. STL files do not contain the original reference geometry to reconstruct the solid and will at the best result produce an approximation. In this case, the use of 3D software converted the STL file into an equivalent 3D surface. Sufficient information can be obtained to rebuild the part with a high degree of accuracy to the original design. To begin processing, the point cloud data for the impeller was imported into a 3D reverse engineering software (Geomagic Design X, Geomagic Scanning Software, U.S.A.). The STL file was converted into a surface model whereby the features on the impeller were

defined in **Figure 3.2**. The model was then deconstructed in 3D CAD design software (SolidWorks 2015, Trimble Navigation, U.S.A.) to obtain the impeller's dimensions. The dimensions acquired from the 3D surface geometry were applied to constructing a CAD model of the impeller. The volute casing's point cloud data was post-processed with a similar method.

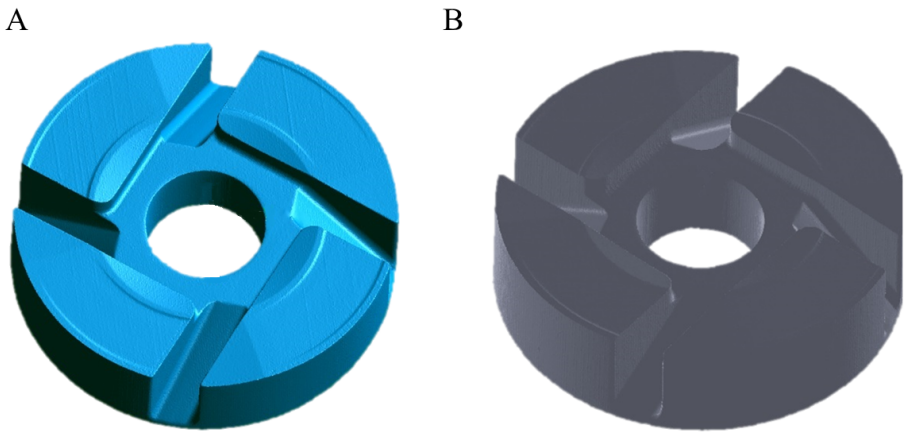

Figure 3-2: A. Conversion of STL file into a 3D surface of HVAD impeller. B. 3D surface model of HVAD impeller.

3.2 Mesh Creation

Unstructured hybrid meshes using tetrahedral, hexahedral and prism elements were constructed for each of the VADs using a combination of ANSYS Meshing (ANSYS Inc., Canonsburg, PA, USA) and TurboGrid (ANSYS Inc., Canonsburg, PA, USA). Sizes of the mesh were, HVAD: 8.5M and HM 2: 2.52M elements. The design of the HM 2 makes hexahedra easier to implement, and most of the domain was meshed using this efficient element shape, hence the mesh size is smaller than that for the HVAD. Each mesh had a minimum of 6 elements across the gaps. Since regions of high stresses are of special interest, inflation layers were generated near the walls of both housing and rotor to resolve the near wall flow.

Refinement ratios of 2 (coarse, 3.8M elements) and 0.5 (fine, 18.1M elements) to yield meshes for the centrifugal VAD. The discretisation errors were assessed by examining pressure heads, velocity fields and fluid dynamic stresses volumes. The same analysis method was applied to the axial VAD using refinement ratios of 1.25 (coarse mesh, 1.3M elements) and 0.625 (fine mesh, 5.6M elements).

Table 3.1: Parameters selected for meshing of the HVAD body for the grid sensitivity study

	Mesh Densities Definitions		
Parameter	**Coarse**	**Medium**	**Fine**
Nodes	1528331	3463148	7679467
Elements	3815388	8266277	18052286

3.2.1 HeartWare HVAD

The mesh generated for the HVAD body was based on the parameters displayed in **Table 3.1**. Regions include inlet and outlet tubes, fluid domain and the magnetic rotor that were meshed using tetrahedral elements with prism layers as shown in **Figure 3.3**. Tetrahedral elements functioned to fill the structured volume region of the HVAD. In addition, inflation layers were introduced as they effectively and efficiently capture boundary layer effects and velocity profiles at the wall. This increased the node density near the wall which affects the overall mesh density, resulting in an increased simulation time.

In addition to the first mesh, both coarser and finer mesh was produced for the HVAD. These meshes have the same structure as the original and were produced by multiplying element size by a factor of 2 (for the coarse mesh) and 0.5 to yield three meshes. The mesh refinement factor defined in **Equation 3.1** from literature is the ratio of the representative cell sizes of fine and coarse mesh respectively and should in general be kept above 1.3 [88]. The operating conditions used for the medium mesh were implemented for the coarse and fine meshes. The discretisation errors for the pressure head and stresses were calculated, analysed and compared among all three meshes.

$$\text{Mesh Refinement Factor, R} = \left(\frac{\text{number of elements in fine mesh}}{\text{number of elements in coarse mesh}}\right)^{\frac{1}{3}} \tag{3.1}$$

3.2.2 FDA Benchmark Blood Pump

Geometry for the blood pump was acquired in the form of CAD files from an open-source website for CFD method validation [82]. The CAD model was imported

into ANSYS and mesh generation for the FDA blood pump was based on the parameters as displayed in **Table 3.2**. For the comparative study, it was decided that a coarse mesh would be appropriate for the requirements of the analysis. The grid structure is the same as the HVAD coarse mesh using tetrahedral elements for volume region with prism layers as shown in **Figure 3.4**. The operating condition was an angular velocity of 3500 rpm with a flow rate of 6 l/min. The quantitative validation then compared velocity plots from specific regions of the blood pump with published Particle Image Velocimetry (PIV) results [82].

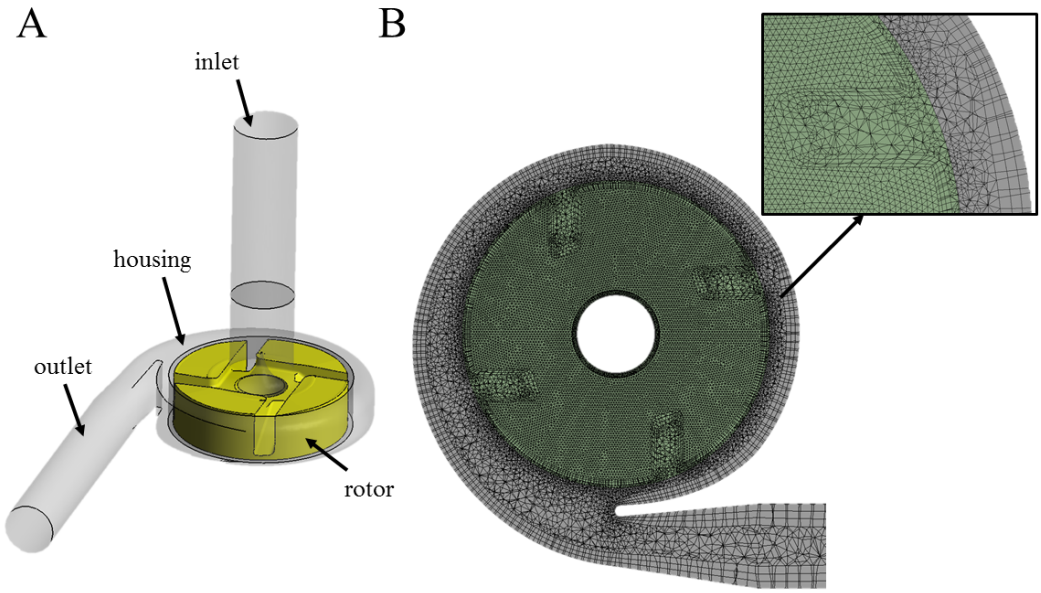

Figure 3-3: HeartWare Ventricular Assist Device. A. CAD Geometry; B. Mesh.

Table 3.2: Parameters selected for meshing of the FDA benchmark blood pump body

Parameter	**Mesh Density Definitions**
Smoothing	Medium
Transition	Slow
Maximum Face Size (m)	0.005
Maximum Tetrahedral Size (m)	0.005
Inflation Layers	3
Growth Rate	1.2
Nodes	1108477
Elements	3132884

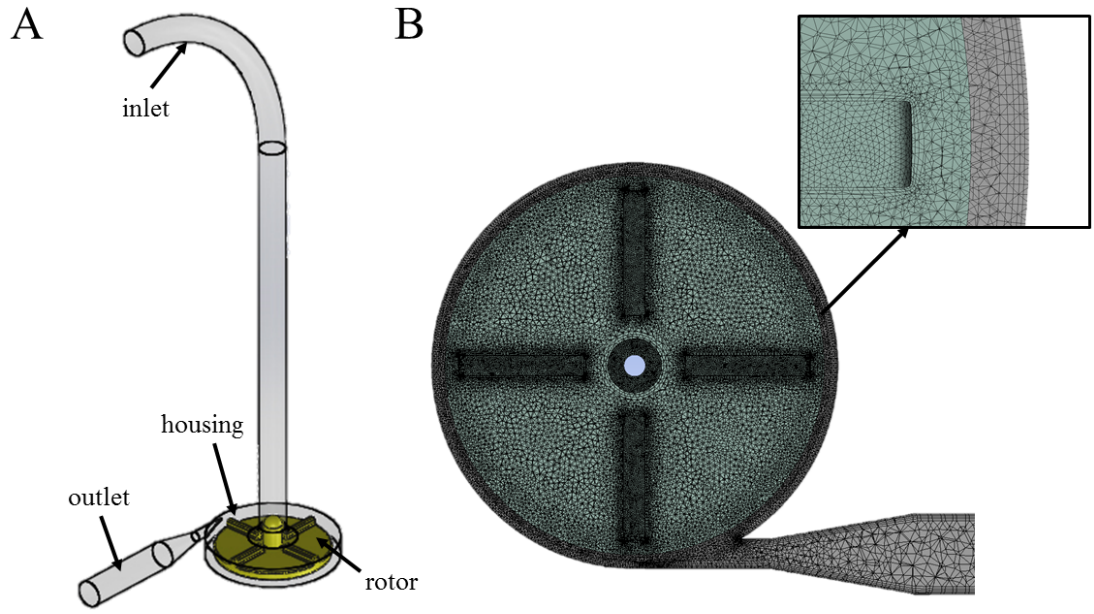

Figure 3-4: FDA's benchmark blood pump. A. CAD Geometry; B. Mesh.

3.3 CFD Setup

3.3.1 Governing Equation

The fundamentals of fluid flow modelling can be referred to as the compressible Navier-Stokes (NS) equation which embodies a set of coupled partial differential equations used to derive the equations of motion for fluid particles. The law of conservation applies to NS as it involves the rate of change of mass, momentum or energy of a certain volume is equal to the rate of diffusion or production internally. The governing equation needed for fluid flow is through simplification of the NS equation by the implementation of assumptions. Hence, the solution obtained represents an approximation and it will always contain a certain degree of domain discretisation or convergence error. A typical NS equation as stated is as followed

$$\rho\left(\frac{\partial\vec{v}}{\partial\vec{t}}+(\vec{v}\cdot\bigtriangledown)\,\vec{v}\right)=-\bigtriangledown P+\bigtriangledown^2\cdot\vec{v}+\rho\vec{g} \tag{3.2}$$

For most fluid flow applications, the NS equation can be simplified analytically based on the assumptions made for different cases. The first equation comprises both a time-dependent term and a non-linear convective term. For incompress-

ible, steady flow the equation simplifies

$$\rho\left(\vec{v}\cdot\bigtriangledown\right)\vec{v} = -\bigtriangledown P + \bigtriangledown^2\cdot\vec{v} + \rho\vec{g} \tag{3.3}$$

The first term is referred to as convective acceleration. The right hand side of the equation contains source terms, induced by pressure, viscous stresses and body forces respectively. As for turbulence, the k-ω shear stress transport model was used as it was found to give an accurate prediction of HVAD pressure head. Menter *et al* proposed a hybrid model that combines the positive aspects of both the k-ε with the k-ω approach [89, 90]. Some of the limitations with k-ε model is the over prediction of turbulent shear stress in either the presence of adverse pressure gradient or in stagnation regions. This results in the suppression of separation at curved walls which means pressure drop is underestimated or excessive heat transfer in reattachment regions. The k-ω model solves a two equation turbulence transport model for the specific dissipation rate with unit s^{-1}, which is related to the rate of turbulence dissipation through

$$\omega = \frac{\varepsilon}{k} \tag{3.4}$$

The k-ω tends to exhibit excellent performance in near wall regions. While, k-ε is used in the fully turbulent region far from the wall. This may cause numerical instabilities due to the choice of the freestream boundary conditions to the turbulence parameters in the two regions (different turbulent viscosity). However, this can be overcome by a blending function used to smoothly vary model constants from one model to another. Therefore, the effect on the flow simulates properly the transport of shear stress.

Steady state simulations were used to provide start-up calculation for transient sliding mesh simulation. It was also used to check if the solution converges since it was less computationally demanding. It was assessed using mass and momentum residuals, which was monitored to be below 10^{-3}, and the pressure at inlet was kept stable. Therefore, all simulations were ran at steady state iterations and the results were used as a basis for transition to transient flow to improve initial accuracy of solution. The parameters selected for steady state simulations are displayed in **Table 3.3**.

Table 3.3: Steady State Simulation Parameters

Parameter	**Value**
Advection Scheme	High Resolution
Turbulence Numerics	First Order
Maximum Iterations	700
Residual Target	10^{-5}

Steady state simulations cannot be used to estimate transient flows which may occur in strong rotor-stator interactions. To start off, there are two simplest approaches in incorporating motion of the impellers to provide a reasonable model of flow for many applications.

3.3.2 Moving Reference Frame Method

Firstly, the moving reference frame (MRF) model is a steady state approximation of the fluid flow in a pump whereby different domain could be assigned different rotational and/or translational speeds [91]. The flow in the rotating domain is solved in a frame of reference moving with the impeller, in other words with the same angular velocity applied. If the domain is stationary, that region is calculated in a stationary reference frame. At the interfaces, flow variables in one zone can be used to calculate the fluxes at the boundary of a neighbouring zone by performing a local reference frame transformation. However in MRF, the mesh remains fixed for computation as it does not account for relative motion of a moving zone with respect to the adjacent stationary zone. This is comparable to suspending the rotor at a specific position and observing the instantaneous flow field that surrounds the moving part. Hence, this method was employed in steady state simulations as the "frozen rotor model".

For MRF formulations, the fluid domain was divided as mentioned into subdomains, each of which maybe rotating/ translating with respect to the stationary frame. The governing equation for each subdomain is defined with respect to the reference frame. Thus, the flow in stationary and translating subdomain is governed by **Equation 3.3**. As for rotating reference frame, the equation of motion are solved with additional terms appearing in the momentum equation.

The position of vector relative to the origin of the rotation axis is defined as [91]

$$\vec{r} = \vec{x} - \vec{x_0} \tag{3.5}$$

where $\vec{x}$ is the position in absolute Cartesian coordinates and $\vec{x_0}$ is the origin of the zone rotation axis. The relative velocity in the moving reference frame can be written as [91]

$$\frac{\partial}{\partial t}(\rho\vec{v}) + \bigtriangledown \cdot (\rho\vec{v}\vec{v}) \tag{3.6}$$

$$\vec{v} = \vec{v_r} + (\vec{\omega} \cdot \vec{r}) + \vec{v_t} \tag{3.7}$$

In **Equation 3.7**, $\vec{v_r}$ is the velocity of in the reference frame, $\vec{\omega}$ is the angular velocity vector (angular velocity of the rotating frame) and r is the position vector in the rotating frame, and $\vec{v_t}$ is the translational velocity of the non-inertial reference frame.

3.3.3 Mixing Plane Method

The mixing plane (MP) approach is the alternative to the MRF and sliding mesh model to simulate fluid flow at steady state conditions in all domains [91]. In this approach, fluid in each subdomain was treated as a steady-state problem. Flow field data from respective domains were passed at the boundary conditions applied at the interface and were spatially averaged in the circumferential direction. The mixing eliminates any unsteadiness in the passage-to-passage flow field, such as separated flow due to circumferential variations. Despite the simplicity of the model, the resulting solutions provided reasonable approximations of the time-averaged flow field.

3.3.4 Transient Rotor Stator Method

As previously mentioned, steady-state simulations cannot be used to estimate transient flows that occur in strong rotor-stator interactions. After steady state approximation of fluid interactions, an unsteady solution is sought after in a sliding mesh simulation which is time-periodic. The unsteady solution was solved repeatedly with a period related to the speeds of the moving domains.

In transient rotor-stator (TRS) model, two or more domains are used and each domain is bounded by an interface whereby the meshes are connected [91]. The interface is where adjacent domains interact with one another to form a mesh interface. The sliding mesh technique allows the adjacent mesh (rotating and stationary) to slide along one another along the interface. The different mesh surfaces do not have to be aligned with neighbouring mesh. In order to solve for transient simulations, the flux across the non-conformal interface of each mesh needs to be computed and it is determined at each new time step. Theoretically, fluxes are solved using faces resulting from the intersection of the two mesh rather than from the interface face.

Table 3.4: Transient State Simulation Parameters

Parameter	**Value**
Number of Time Steps per Run	540
Time Steps (s)	User Specified
Initial time (s)	0
Time Step Interval (s)	10

The TRS model interface was selected for transient simulations to enable actual rotation of the rotor relative to the static domains of the pump with the following parameters in **Table 3.4**. For this study, the time step was adjusted with respect to the rotational speed to yield a 2° rotation per step. The transient simulations were run using second-order schemes in space and time until the pressure head showed smooth periodic behaviour. An averaged pressure head, velocity and turbulent viscosity were obtained after the flow field stabilised.

3.4 Operating Conditions

3.4.1 Boundary Conditions

Blood flow calculations were conducted using a commercial CFD solver (ANSYS CFX, ANSYS Inc, Canonsburg, PA, USA) when completed meshes were loaded for simulation setup. Unlike an axial VAD, a centrifugal VAD has a non-axially symmetric geometry due to its inlet and outlet. The fluid domain of the centrifugal VAD was divided into three parts, namely rotating, stationary and interfaces

(**Figure 3.5**). The rotating domain included the cylindrical region surrounding the impeller (labelled as rotating housing) and the impeller. The impeller was constrained to rotate at a specified rotational speed about the Cartesian Z axis. Inlet, outlet and volute casing is part of the stationary domain. Interfaces were the regions between stationary and rotating domains. Boundary condition for both pump simulations is as specified and shown in **Table 3.5**.

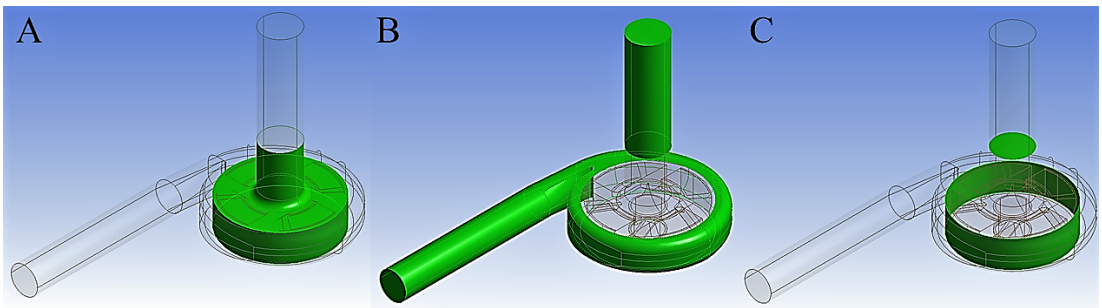

Figure 3-5: HVAD Fluid Domains. A. Rotating; B. Stationary; C. Interfaces.

Table 3.5: Boundary Conditions for VAD CFX Simulation

Domain	**Regions**	**Boundary Conditions**	**Input**
Rotating	Rotating Housing	Type	Wall
		Detail	Counter Rotating Wall
	Impeller	Domain Motion	User Specified (rpm)
Stationary	Inlet	Type	Inlet
		Detail	User Specified (l/min)
	Outlet	Type	Opening
		Detail	Pressure (0 Pa)
	Volute Casing	Type	Wall
		Domain Motion	Stationary
Interfaces	Inlet, Volute Interface	Frame Change	MRF or TRS

3.4.2 Steady Flow

Unsteady Reynolds Averaged Navier-Stokes (URANS) equations were solved using a commercial, vertex-centered, finite volume solver ANSYS CFX (ANSYS Inc., Canonsburg, PA, USA). The largest Reynolds number at the inlet was 2530 which is above the transition to turbulence (usually taken to occur around 2300 for pipe flow) and in the low turbulence flow regime. The k-ω shear stress transport model was used to model the turbulence. The operating points chosen for

the calculations were based around a typical working point for LVADs: 5 l/min at 100 mmHg which required an impeller rotational speed of 3000 rpm. The inlet boundary condition was mass flow rate, fixed to give flow rates of 3, 5 or 7 l/min, with a speed set at 3000 rpm. The rotational speed was varied from 2200 to 3400 rpm, while maintaining 5 l/min. The outlet boundary condition was constant, with uniform pressure at 0 mmHg. Blood was treated as a Newtonian fluid with a density of 1050 kg/m^3 and dynamic viscosity of 3.5 mPas. Boundary conditions were as prescribed and the parameters for simulations are shown in **Table 3.6**.

Transient calculations were used and the rotation of the impeller was accounted for by using sliding meshes, also known as the transient rotor-stator approach. These transient calculations were initialised from steady-state calculations in which the motion of the impeller was incorporated using the multiple reference frame (MRF) approaches. The time step for the transient calculations was adjusted with respect to the rotational speed to yield 2° rotation per step. These calculations were run using high-resolution, and second-order backward Euler, schemes in space and time respectively, for three full rotations. Following the first rotation, the pressure head showed a smooth periodic behaviour. The averaged pressure head and velocity field were obtained from the third rotation.

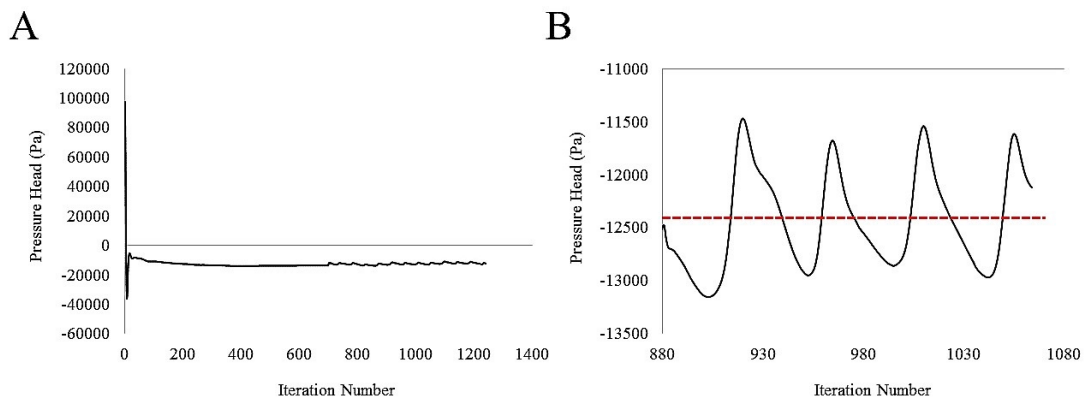

Figure 3-6: A. CFX Solver results from steady state to transient simulations. B. Plot of the change in pressure head with time step and the red dotted line represent the average pressure head.

3.4.3 Pulsating Flow

Data from the HeartWare VAD (HVAD) is obtained from Noor *et al* [92] pulsatile mock circulation loop over one cardiac cycle. This inlet boundary condition was

Table 3.6: User Specified Operating Conditions for Steady Flow in a Centrifugal Pump Simulations.

Operating Conditions	1	2	3	4	5	6
Rotational Speed (rpm)	2200	2600	3000	3000	3000	3400
Time Steps (s)	0.000152	0.000128	0.000111	0.000111	0.000111	0.000095
Flow Rate (l/min)	5	5	3	5	7	5
Mass Flow Rate (kg/s)	0.0875	0.0875	0.0525	0.0875	0.1225	0.0875

applied in **Chapter 4**. The inlet boundary condition for the non-pulsatile model was a constant mass flow of 5 l/min. For the pulsatile model, the time-dependent flow rate obtained from mock loop experiments from Noor's paper was set at the inlet. In this chapter, only the centrifugal VAD model was analysed. Since the working principles are similar, the obtained methodology for a centrifugal blood pump can still be applied to an axial flow pump. A commercial finite volume solver was used to calculate the flow fields in a centrifugal VAD, the HeartWare HVAD (Thoratec). The operating condition for the non-pulsatile model was 2600 rpm, mean flow of 5 l/min. Transient solutions were calculated, with the rotating impeller accounted for using a TRS, and turbulence accounted for using an unsteady Reynolds-averaged Navier Stokes (URANS) turbulence model.

Table 3.7: User Specified Operating Conditions for Pulsating Flow in a Centrifugal Pump Simulations.

RPM	Inlet flow condition	Inlet (l/min)	Outlet (Pa)	Rotor
2600	Non pulsatile	5	0	Frozen
	Non pulsatile	5	0	TRS
	Pulsatile	2 – 13	0	Frozen
	Pulsatile	2 – 13	0	TRS

3.5 Post-processing

3.5.1 Coordinate Transformation of Stress

Although there are forces due to both pressure and viscous stress the pressure does not affect the blood components. To date, scalar shear stress (SSS), first proposed for use in haemolysis estimations by Bludszuweit [4] is a scalar invariant of the stress tensor, analogous to the von Mises stress for solids, which is calculated from the components of the stress tensor as

$$\sigma_{scalar} = \left[\frac{1}{6}\left((\sigma_{11}-\sigma_{22})^2 + (\sigma_{22}-\sigma_{33})^2 + (\sigma_{33}-\sigma_{11})^2\right) + (\sigma_{12}+\sigma_{23}+\sigma_{13})^2)\right]^{\frac{1}{2}} \tag{3.8}$$

Von Mises is defined as a single value of stress at a point based on the six stress values. However, the Von Mises stress is scaled such that a simple shear stress produces a SSS of the same value i.e.

$$\sigma_{scalar} = \frac{1}{\sqrt{3}}\sigma_{vonMises} \tag{3.9}$$

The viscous stresses of specific interest are shear stress and elongational stress. In general, the viscous stress can be described by a symmetric tensor. The stress tensor characterises the properties of a physical system, in this case with cells, with three diagonal components giving the elongational stresses (or, if negative, the compressional stress) and the off diagonal components giving the shear stresses (**Equation 3.8**).

$$\sigma = \begin{pmatrix} \sigma_{11} & \sigma_{12} & \sigma_{13} \\ \sigma_{21} & \sigma_{22} & \sigma_{23} \\ \sigma_{31} & \sigma_{32} & \sigma_{33} \end{pmatrix} \tag{3.10}$$

For an incompressible, isotropic, Newtonian fluid, the stress tensor can be easily found from the velocity gradient (or strain rate) tensor (e_{ij})

$$\sigma_{ij} = \mu\dot{\varepsilon_{ij}} \tag{3.11}$$

$$\dot{\varepsilon_{ij}} = \mu\frac{1}{2}\left(\frac{\partial V_i}{dx_j} + \frac{\partial V_j}{dx_i}\right) \tag{3.12}$$

Table 3.8: Components of simple stress tensor in comparison with simplified scalar shear stress.

Case	**Components of Stress Tensor**	**Scalar Shear Stress (SSS)**
Elongational Stress (Strain Rate)	$\begin{pmatrix} \sigma_{11} & 0 & 0 \\ 0 & 0 & 0 \\ 0 & 0 & 0 \end{pmatrix}$	σ_{11}
Simple Shear Stress	$\begin{pmatrix} 0 & \sigma_{12} & 0 \\ \sigma_{21} & 0 & 0 \\ 0 & 0 & 0 \end{pmatrix}$	σ_{12}

This is because the stress is directly proportional to the velocity gradient. According to Lee *et al* [68] shear stress will first cause the cell to be rotated and then deformed. While elongational stress will deform the cell without rotation. In general, the deformation of liquid is proportional to rotation free strain rate. However, simple shear is a combination of deformation and rotation. This has consequences for the way cells and polymer chains deform, stretch and in some cases break during flow. A generalised shear stress equation was defined in order to be consistent with the normal stress equation.

$$\sigma_{ij} = 2\eta\dot{\varepsilon}_{ij} \tag{3.13}$$

Most numerical models for blood damage use SSS which is frame invariant thus no transformation is required. However, by dividing the stress tensor into shear and elongation, these stresses are not frame invariant. So firstly, the local reference frame was defined by the local direction of the velocity and both stress equations were computed from a transformed strain rate. For the two simple cases of an incompressible, isotropic, Newtonian fluid under uniaxial extensional stress and simple shear stress, SSS simplifies as shown in the **Table 3.7**. The new stress tensor is a contravariant second order tensor. From x_i-system to the new $x_i^{'}$-system, the σ_{ij} components from the initial system were transformed into $\sigma_{ij}^{'}$ in the new coordinate system according to the tensor transformation rule (**Equation 3.14**).

$$\sigma^{'} = AA^T\sigma \tag{3.14}$$

Where A is the rotation matrix which is represented by a_{ij}. The stress tensor components were as shown in **Figure 3.7** and the **Equation 3.14** was written

in matrix form as displayed as **Equation 3.15**,

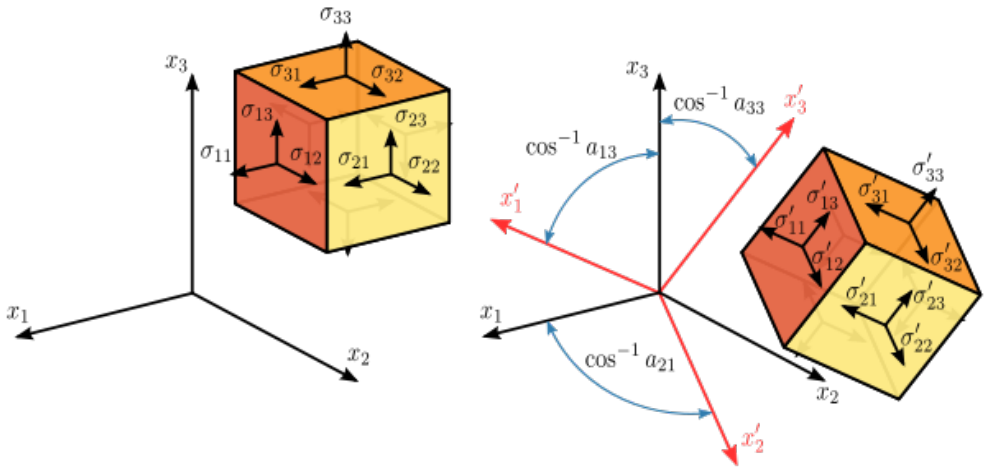

Figure 3-7: Coordinate Transformation of Stress Tensor [93].

$$\begin{bmatrix} \sigma_{11}^{'} & \sigma_{12}^{'} & \sigma_{13}^{'} \\ \sigma_{21}^{'} & \sigma_{22}^{'} & \sigma_{23}^{'} \\ \sigma_{31}^{'} & \sigma_{32}^{'} & \sigma_{33}^{'} \end{bmatrix} = \begin{bmatrix} a_{11} & a_{12} & a_{13} \\ a_{21} & a_{22} & a_{23} \\ a_{31} & a_{32} & a_{33} \end{bmatrix} \begin{bmatrix} a_{11} & a_{21} & a_{31} \\ a_{12} & a_{22} & a_{32} \\ a_{13} & a_{23} & a_{33} \end{bmatrix} \begin{bmatrix} \sigma_{11} & \sigma_{12} & \sigma_{13} \\ \sigma_{21} & \sigma_{22} & \sigma_{23} \\ \sigma_{31} & \sigma_{32} & \sigma_{33} \end{bmatrix} \tag{3.15}$$

The full derivation of the stress tensor coordinate transformation can be seen in the **Appendix**, and the newly transformed stress tensor components were found. The components chosen for post-processing are similar to the forces that simulate cell or polymer chain deformation in the direction of flow. The elongational and shear stress were computed from the transformed strain rates and their rotating component, and are displayed respectively as:

$$\sigma_{11}{}^{new} = 2\eta\sigma_{11}^{'} \tag{3.16}$$

$$\sigma_{12/13}{}^{new} = 2\eta\left(\sigma_{12}^{'2} + \sigma_{13}^{'2}\right)^{\frac{1}{2}} \tag{3.17}$$

3.5.2 Fluid Stress Threshold Volumes

To assess both the magnitude and extent of the normal stress $\vec{\sigma'}_{11}$, relative to the shear stress $\vec{\sigma'}_{12/13}$, the flow domain was thresholded into regions with stress values greater than 10, 50 and 100 Pa. While blood damage processes are complicated functions of both stress magnitude and exposure time, these values were chosen as representative values for low, middle and high stress. Based on the pub-

lished data: 10 Pa is thought to be relevant to the cleavage of vWf [56, 57, 60], which is the blood damage aspect of bleeding events; 100 Pa is thought to be relevant to haemolysis [47, 49, 67]; and 50 Pa is an intermediate threshold. The values are not intended to be exact but are a way to quantitatively compare the stress fields in different VADs. The thresholded regions were displayed in CFX Post (ANSYS Inc., Canonsburg, PA, USA) to determine where the stresses occurred. For quantitative comparison, the volumes of the thresholded regions were calculated. Since the simulations were transient, the volumes were found every 20° of impeller rotation, and these volumes were averaged for comparisons.

3.5.3 Cell Deformation and Protein Unravelling Threshold Volumes

Since the available data suggest cell deformation [68] and protein unravelling [77] occur at lower elongation stress, compared to shear stress, the volumes were assessed which could deform cells and unravel proteins. Regarding RBC deformation, Lee *at el* [68] measured cell deformation as a function of either shear or normal stress. This data was used to find stress values which would create a DI of 0.5 (**Figure 3.8 A**). A DI of 0.5 is achieved with a shear stress of 13.4 Pa, whereas the value with normal stress is much lower at 1.8 Pa. Regions of the VADs with $DI > 0.5$ were compared for shear and normal stress by determining the threshold values at 13.4 Pa and 1.8 Pa respectively in **Figure 3.8 A** below.

Thresholds for unravelling vWf come from work by Sing *at el* [77] who used a coarse-grained numerical model to investigate the hydrodynamic forces on vWf molecule. In their study a 27% extension of the vWf molecule was obtained with a shear rate of 10^4 s^{-1}, or an extensional rate two orders of magnitude lower at 200 s^{-1} (**Figure 3.8 B**). These correspond to stresses of 35 Pa and 0.7 Pa respectively for the CFD calculations presented here.

3.5.4 Exposure times

Fluid stresses act in combination with exposure times to cause deformation of, and eventually damage to, the blood components. To estimate the exposure time of the blood components to both normal and shear, stress, pathlines were calculated from the final timestep of the solution. The final timestep was chosen

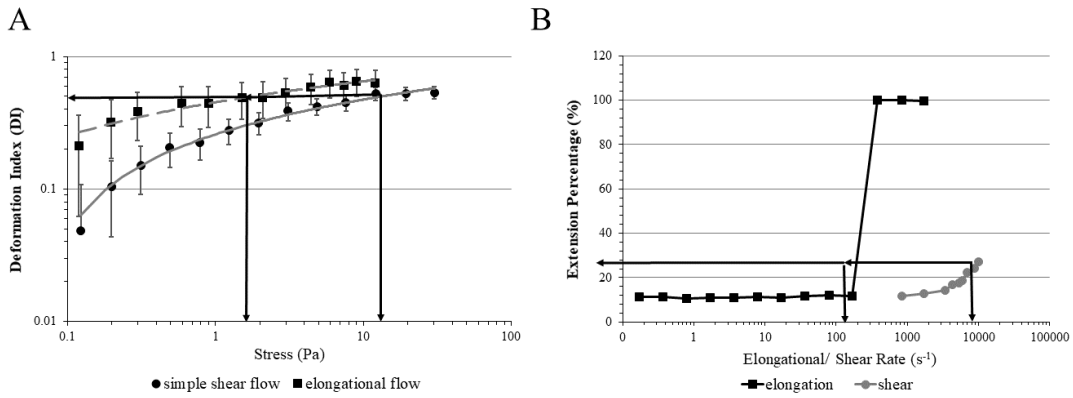

Figure 3-8: A. Data from Lee *et al* [68] shows RBC deformation occurring with both shear and elongational flow. By defining a DI that would compute evident deformation at 0.5, the threshold values were extrapolated to obtain threshold values for cell deformation at shear flow 13.4 Pa and elongational flow 1.8 Pa; b. Data from Sing *et al* [77] shows vWf deformation occurring with both shear and elongational flow. The maximum extensional percentage was defined at 27%, the threshold values were extrapolated to obtain threshold values at shear flow 10^4 s^{-1} (35 Pa) and elongational flow 200 s^{-1} (0.7 Pa).

since the volumes of the high-stress regions were not found to vary significantly with time. Pathlines were seeded in the regions of cell deformation and protein unravelling described above and were tracked both forwards and backwards using a Runga-Kutta method with a tolerance of 1 % of the mesh element size. The length of time within the region was calculated for each pathline and the mean was then found. The total number of pathlines used was 2000. This value was chosen based on a convergence test using the RBC deformation regions in the HVAD. Reducing the number of pathlines to 500 resulted in a reduction in the normal stress exposure time of almost 10 %, while increasing the number to 8000 resulted in an increase in that exposure time of around 5 %. There was almost no change in the shear stress exposure times over this range in the number of pathlines. This increase in normal stress exposure time with the number of tracks suggests our analysis is more likely to underestimate, rather than overestimate the normal stress exposure time.

Chapter 4

Normal fluid stresses are prevalent in two commercial VADs

In this chapter, I performed CFD analysis on the two most commonly implanted VADs, the HVAD and the HeartMate 2, and then used the velocity gradients to calculate the magnitudes of normal and shear stress components. The sections of text from this publication [1] which are in the thesis are in section 4.5 in Chapter 4, which explains the results obtained from my simulations.

Since rotary ventricular assist devices are assumed to exert mainly shear stress, studies of blood damage are based on shear flow experiments. However, measurements and simulations of cell and protein deformation show normal and shear stresses deform, and potentially damage, cells and proteins differently. The aim was to use computational fluid dynamics to assess the prevalence of normal stress, in comparison with shear stress, in rotary ventricular assist devices. Steady state simulation results were used to analyse mesh sensitivity of HVAD model. Steady state approximation studies between MRF and MP were conducted. Suitable mesh and solver setup were determined from the analysis of results from initial runs. The validation of simulation model was to fit simulated pressure head and velocity field against experimental results from the literature.

Transient results were examined through different flow pathways of the HVAD. This is to describe the occurrence of fluid dynamic stresses in specific regions of the device. The wall shear stress contour, velocity field and isovolume plot were used to analyse the existence of shear and normal stresses in the HVAD. The effects of varying operating conditions such as rotational speed and flow rate on the volume of stresses produced was also investigated. In addition, different axial gap clearances were simulated. Stresses produced were compared because its sensitivity to rotational speed, pressure head and flow remains unknown in current HVAD research. Lastly, the results were compared against the HM 2 model (axial pump) simulations to determine the prevalence of normal stress in comparison with shear stress in rotary VADs. This study is the first to quantify the fluid stress components in real blood-contacting devices.

4.1 CFD Results and Experimental Validations

4.1.1 Mesh Sensitivity and Selection

Firstly, three meshes of coarse, medium and fine were constructed to conduct a mesh sensitivity study. The details of mesh construction were discussed in **Chapter 3**, under section 3.2.1. The mesh discretization error was assessed by comparing pressure head, velocity fields and stress volumes using the three meshes, with the operating condition 3000 r/min, 5 l/min and with the steady-state (MRF) calculations (as shown in **Figure 4.1** and **Figure 4.2**).

From pressure contour plots, high negative pressures (ranging from 21327 Pa to 22242 Pa) were observed at the inlet flow channel when the fluid was drawn into the VAD. The high pressure was relieved when fluid flowed through the impeller flow channels which produced low pressure values ranging between -4000 and -10000 Pa. Pressure head becomes positive as fluid passed through the outlet as the fluid pressure in the VAD was greater than that of the atmosphere and produced low pressures of 600 to 900 Pa. However, the minor difference between the coarse and finer meshes is the pressure contour region along the wall of two impeller blades shown in **Figure 4.1 A**. There were regions showing negative pressure of approximately -10000 Pa that can be seen concentrated at

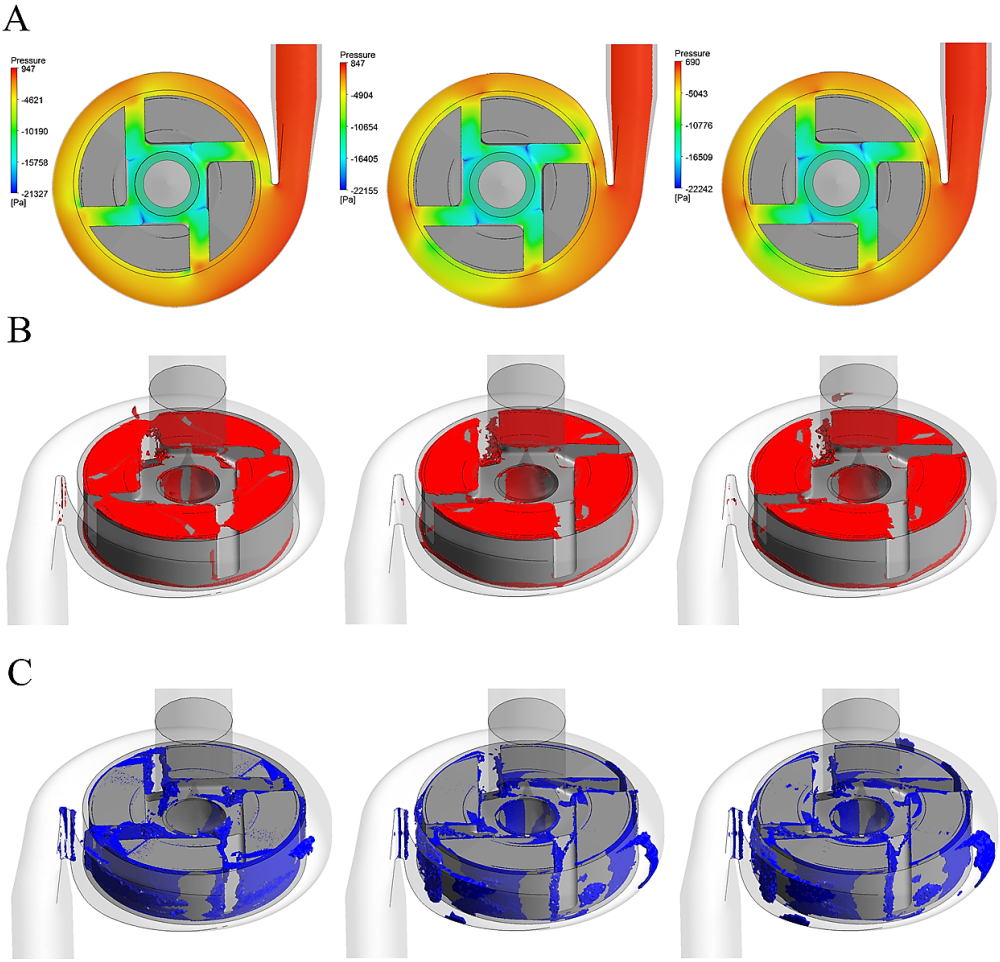

Figure 4-1: Mesh sensitivity study for centrifugal VAD with coarse, medium and fine meshes respectively. A. Pressure distribution; B. Shear stress regions; C. Normal stress regions.

the outlet tip of the flow channel and spread thinly along the walls of the impeller. The area was significantly more evident as mesh size was decreased. Moreover, the pressure distribution roughly between -4600 Pa and 950 Pa near the outlet also appeared to be larger for coarse mesh than finer meshes. The pressure heads were 107.7, 105.9 and 105.2 mmHg with coarse, medium and fine meshes respectively, giving a percentage error of 0.6 % between medium and fine meshes. The isovolume regions highlighted in red for shear stress and blue for normal stress were plotted in CFX Post. The shear stress volume produced was consistent with stresses occurring in tight gap clearance between the upper and lower plane of the impeller and housing, unaffected by fluid flow (**Figure 4.1 B**). As for normal

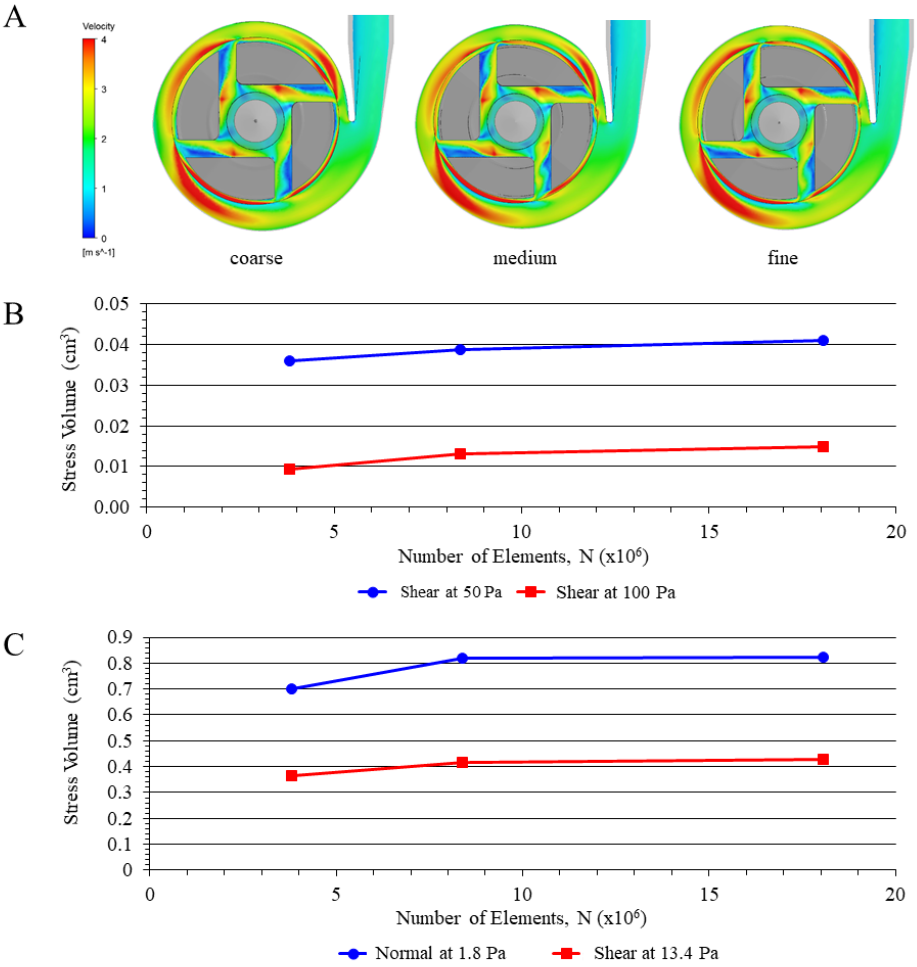

Figure 4-2: Mesh sensitivity study for centrifugal VAD with coarse, medium and fine meshes, respectively: (a) comparison of velocity fields; (b) comparison of volumes of shear stress at 50 and 100 Pa; (c) comparison of volumes of threshold stresses for RBC deformation.

stress volume, the position of stresses tends to vary but the volume remains relatively similar to values obtained from finer meshes. For coarse mesh, the approximation of the flow field may have caused an overestimation of normal stress volume as shown in **Figure 4.1 C**.

For qualitative comparison, the velocity fields are shown in **Figure 4.2 A**. Differences between coarse and medium meshes can be seen, for example in the south pointing blade gap, but are more difficult to spot between medium and

fine meshes. Due to their direct dependence on velocity gradients, the fluid stress is more sensitive to discretization error than the velocity. The percentage difference between medium and fine meshes was 8.9 % and 5.7 % for the normal and shear stress volumes at 50 Pa, respectively. The percentage difference between medium and fine meshes was 0.6 % and 3 % for the normal and shear RBC deformation volumes, respectively. The medium mesh was used as it had an acceptable balance between computational resources and accuracy (**Figure 4.2 B** and **Figure 4.2 C**).

For the first 700 iterations, both MRF and MP approaches solved steady flow equations which are approximate of the unsteady interaction between the rotor and stator. At the interface with MRF, this produced a flow field which is dependent on the relative position of the impeller and the volute as shown in **Figure 4.3 A and C**. In MP method, the exchange of circumferential averaged flow quantities at interface is independent of relative position of impeller and volute. Thus the flow field characteristics observed was equivalent on either side of the interface, conserving momentum and energy (**Figure 4.3 B and D**). The effects of the calculated flow field to the volume of stresses produced appears to be not significant. The difference between the values ranged between 0.0002 to 1 cm^3 and the stresses produced by MP method is lower than MRF method as it introduces physical approximations (**Figure 4.4**).

4.1.2 Validation

For validation, the calculated pressure-flow plots were compared with published experimental data for steady flow in the HVAD and HM 2 [92]. To date, no published experimental data on the velocity fields for either the HVAD and HM 2, for the real scale. Therefore, a benchmark blood pump obtained from the US FDA [82] was modelled using a mesh created with the same principles as described in section 3.2.1 and with the flow calculated using the methods given in section 3.4.2. The operating condition was an angular velocity of 3500 rpm with a flow rate of 6 l/min. The quantitative validation then compared velocity plots from specific regions of the blood pump with published PIV results.

The calculated pressure heads were in good agreement with experimental data from Noor *et al* with an average percentage error of less than 5 % (**Figure**

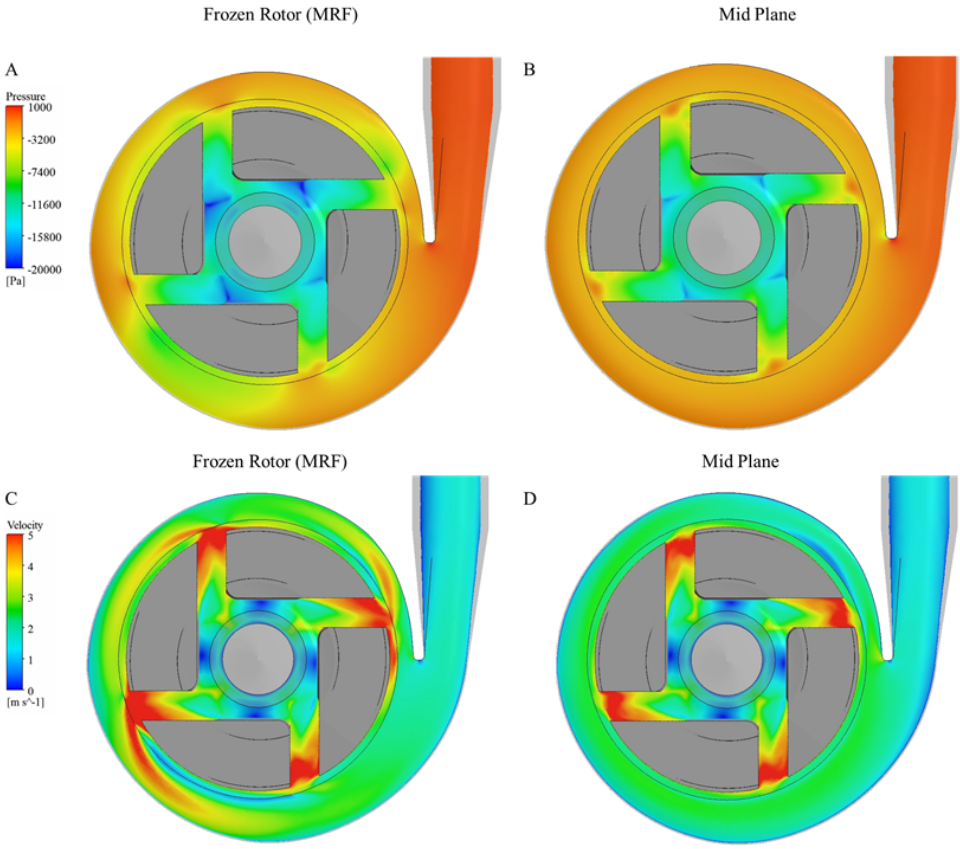

Figure 4-3: HVAD Flow Fields. A. Pressure contour with MRF method; B. Pressure contour with MP method; C. Velocity contour with MRF method; D. Velocity contour with MP method

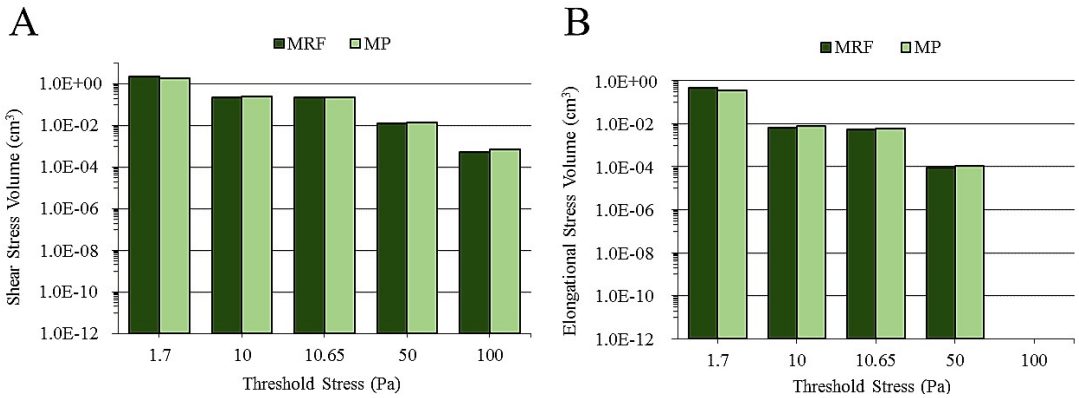

Figure 4-4: Volume of Stresses Produced using MRF and MP methods. A. Shear Stress; B. Normal Stress.

4.5 B) [92]. Therefore, to validate the CFD method, here the flow field for the FDA Benchmark blood pump was solved and the calculated velocity fields were compared with the published PIV results. There is a reasonable qualitative agreement in the velocity fields and an average 4.6 % error as compared to the measurements (**Figure 4.6**). To date, there is no existing experimental data on the velocity field of the HeartWare HVAD.

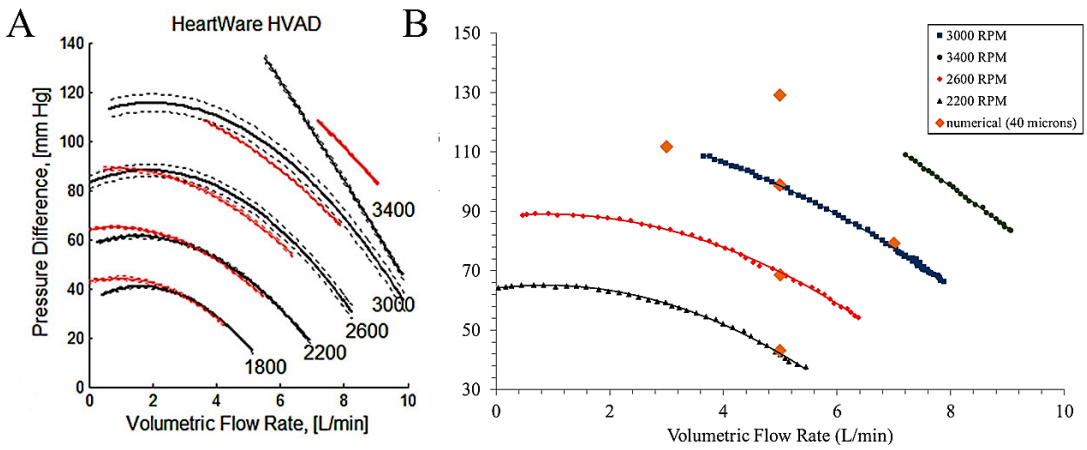

Figure 4-5: A. HVAD differential pressure (aortic left ventricular pressure) versus flow rate (HQ) plot; B. Simulated pressure head at the specific flow rates against a digitised plot of **Figure 4.5 A** experimental results.

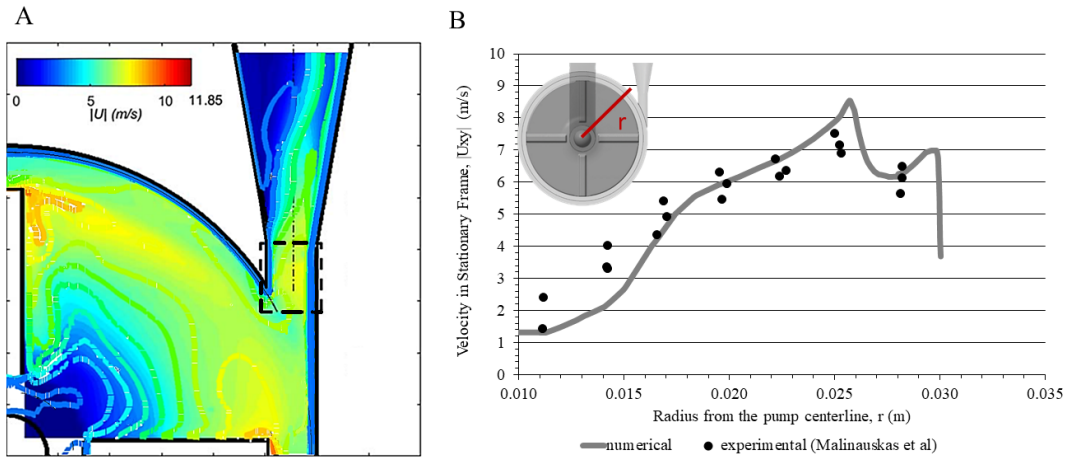

Figure 4-6: A. 2D contour plot of experimental PIV measurements from Malinauskas *et al* [82] to compare with velocity contour lines from our calculations; B. Velocity profile along pump radius compared with experimental data.

4.2 Flow Field of Centrifugal Pump

4.2.1 Primary Flow Path

Understanding the dominant flow structures and the root causes for fluid dynamic stresses occurring at specific regions of the fluid domain is of vital importance in order to assess and improve the designs of VADs. The flow field shown in **Figure 4.7 A** depicts velocity contours and isovolume plot of normal stress at the condition of 3000 rpm rotational speed of a 5 l/min flow rate. The primary flow path was designed to achieve desired head rise. Blood enters the inflow cannula from the left ventricle due to the high negative pressure. It then passes through the impeller flow channels and collects at the volute at a lower velocity. The inertial property of blood by which it continues in a circular motion at constant velocity causes the normal stress to appear alongside the impeller blade. The normal stresses exist at the edges of the flow channels in a straight line due to centrifugal force stretching and directing blood away from the center post which the impeller body is revolving (**Figure 4.7 B**). There was also a stagnation point at the flow divider between the outlet and re-entering volute where an accumulation of stresses occurred. Large high velocity regions can be witnessed at the edge of the blade as the impeller rotates. The constant velocity elongates the fluid leaving a trail of stress-induced regions along the wall of the blades.

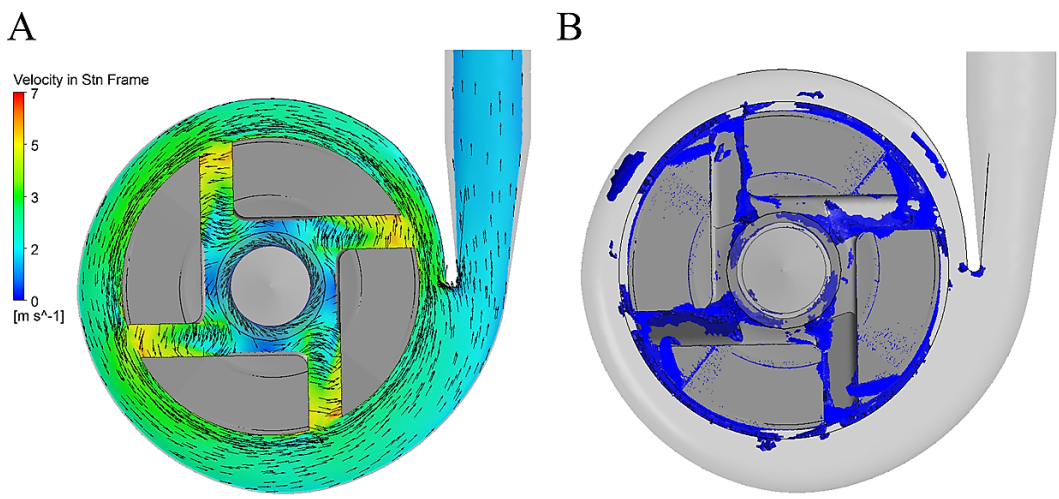

Figure 4-7: Primary flow path in the centrifugal VAD at initial phase. A. Velocity contour plot with velocity vectors; B. Normal stress Volume.

4.2.2 Secondary Flow Path

There was a secondary flow path outside of the rotating magnet as this was designed to wash the underside of the impeller. Blood enters from the volute and passes underneath the impeller. It flows through the annular gap between the impeller and center post and is re-entrained in the primary flow path (**Figure 4.7**). Shear stresses were produced over a distance in between thin-walled structures as the impeller rotating wall has some relative velocity to the other. Furthermore, there is an evident velocity gradient in the annular gap which causes shearing of blood cells as the blood is being pressurised through a tight gap in **Figure 4.8**.

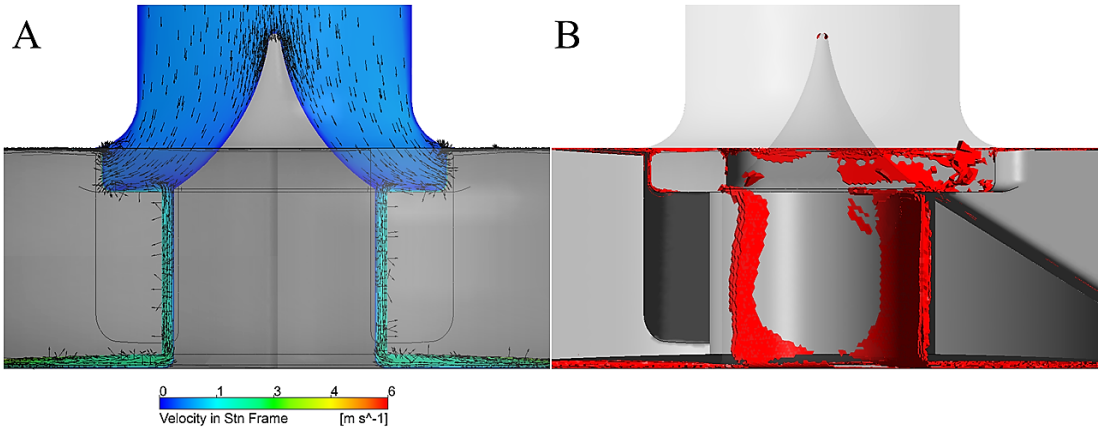

Figure 4-8: Secondary flow path in the centrifugal VAD. A. Velocity contour plot with velocity vectors; B. Shear Stress Volume.

An alternative route for blood flow was designed to support the impeller. Initially, the blood enters the impeller flow channel and passes the HTB. Then, it re-entrained in the primary flow path or continues through the downstream HTB. Shear stresses appeared in the axial gap clearance between the upper plane of the impeller and the volute casing. Although it is generally assumed that centrifugal VAD exerts predominantly shear stresses, the preliminary calculations of the flow field include substantial regions with normal components in addition to regions with large shear flows. The shear stress variation for centrifugal VAD design developed mostly on the impeller, thus it was examined as shown in **Figure 4.9**.

To correlate the volume of stresses produced above the blood damage threshold, shear stress distribution displayed that most of the regions of the impeller experi-

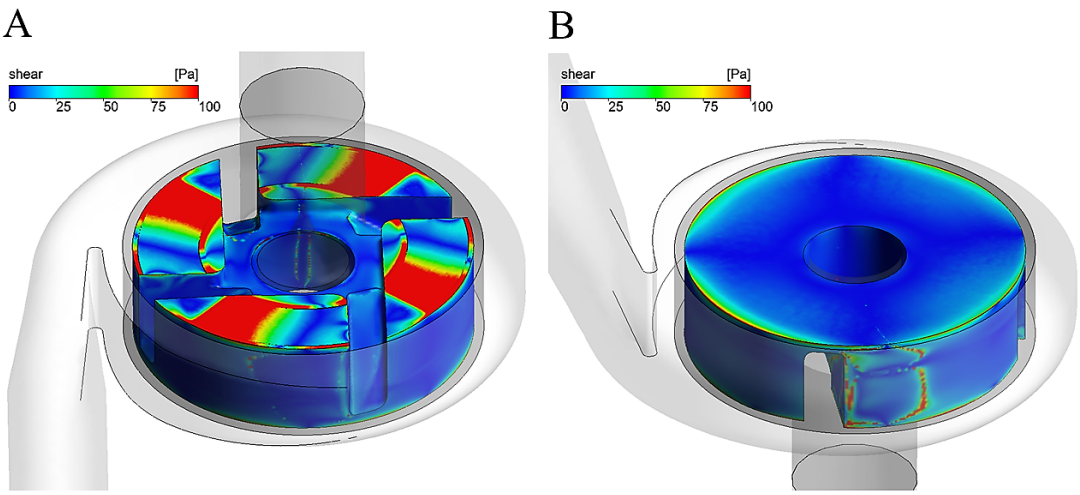

Figure 4-9: Shear stress distribution on impeller. A. Topside; B. Underside.

ence stress levels of lower than 25 Pa. Volumes that are subjected to viscous shear stresses below 100 Pa are small. Small volumetric portions in the HVAD undergo haemolysis and platelet activation at the axial gap clearance between HTB and volute casing. Nevertheless, the underside and walls of the impeller produce lower values of wall shear stress below 25 Pa, which shows that the design is susceptible to other types of blood damage such as protein untangling. This includes the comparison against normal stress variation of the impeller which also displayed stress distribution to occur below 25 Pa in **Figure 4.10**.

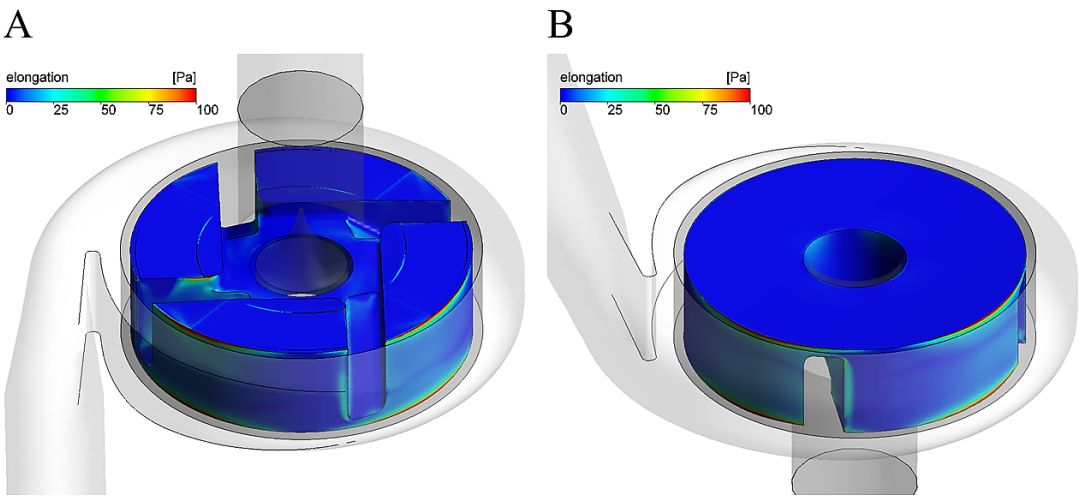

Figure 4-10: Normal stress distribution on impeller. A. Topside; B. Underside.

4.3 Flow Field of Axial Pump

Comparing centrifugal VAD against the axial VAD, the flow path of the axial VAD started with the blood flow entering the pump through the tripod conical bearing. At most operating conditions as described by Fraser *et al* [94], the flow smoothly follows the shape of the impeller blades. Turbulence, helical flow and recirculation zones developed downstream in between the diffuser blade causing a disturbance. The helical flow was enhanced by the curve of the blades at the outlet.

According to the contour plots for the axial VAD, the data showed that the high pressure regions between the blades and volute casing experience high shear stress, while the negative low pressure side of the blade experiences the normal stress (**Figure 4.11 A**). High velocity regions also appear to show more shear stress volume in **Figure 4.11 B**. Normal stress volume forms along the curvature of the blade which tends to follow the streamline of the flow as displayed in **Figure 4.12 C and D**.

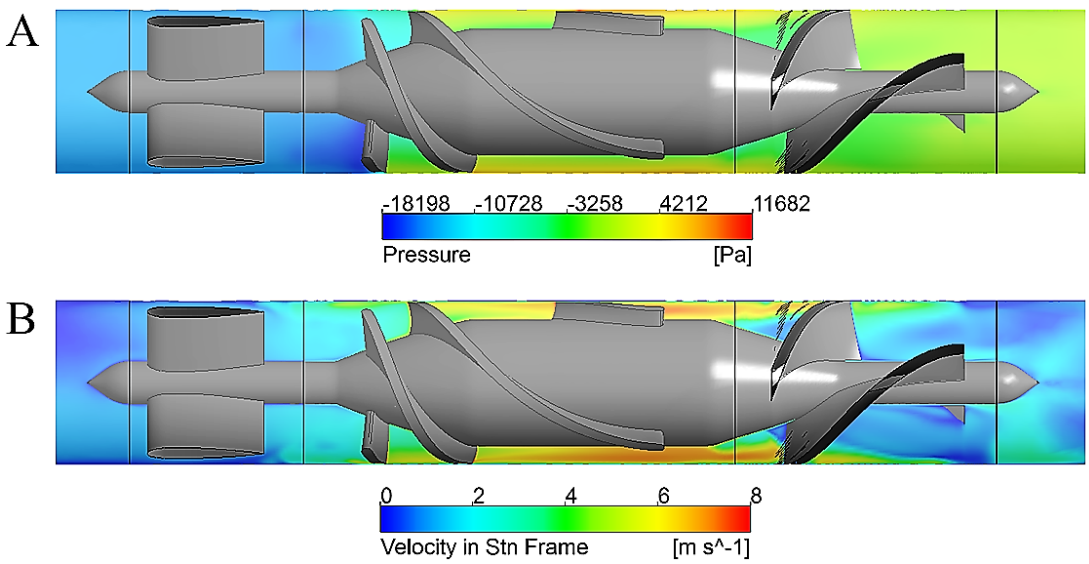

Figure 4-11: Axial VAD Flow Field. A. Pressure contour plot; B. Velocity contour plot.

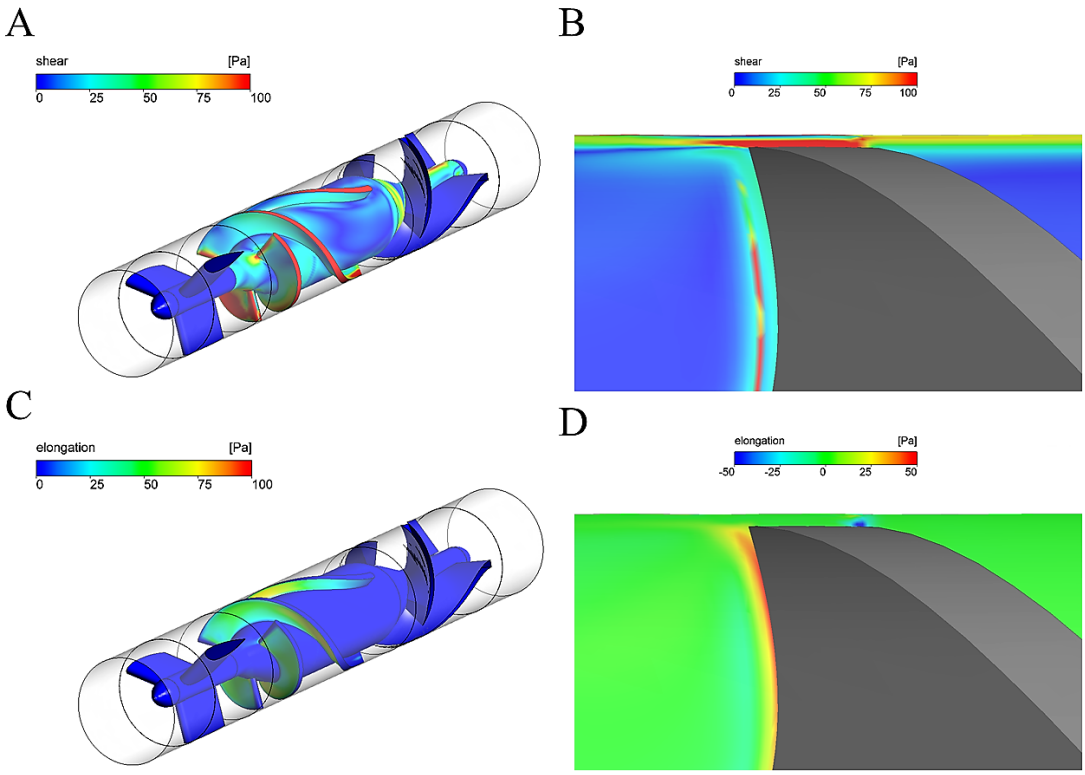

Figure 4-12: A. Estimates of shear stress in axial VAD; B. Shear stress distribution at the blade; C. Estimates of normal stress in axial VAD; D. Normal stress distribution at the blade.

4.4 Fluid Stresses Threshold Volumes

In the HVAD the highest shear stress was found in the narrow axial hydrodynamic bearing gap clearance of 20 μm above the impeller (**Figure 4.13**). Shear stress in this region was in the range of 100 Pa to 1000 Pa. Other regions with high shear stress were the gap under the impeller (shear stress up to ∼80 Pa), shear stress on the volute wall was in the range 0 to 60 Pa, and there were regions of high shear within the blade passages (up to ∼15 Pa). The bulk of the volute experienced shear stress in the range 2 to 6 Pa. Similarly the highest normal stresses (up to ∼100 Pa) were also found in the hydrodynamic bearing gap, specifically in the regions of the narrowest part of the gap where blood leaks over the edges of the hydrodynamic blades and tiny regions at the tips of the leading edges of the blades.

Normal stress up to around 15 Pa was found in the inter-blade passages where, due to a recirculation zone which narrows the passageway, the forward flow is forced to accelerate. There was also a stagnation point at the flow divider between the outlet and re-entering volute where both high shear and high normal stresses occurred (up to 23 and 33 Pa respectively). In the HM 2, the highest shear stresses were found in the blade tip gaps (up to ∼400 Pa), whereas the blade's negative, low pressure side experienced the highest normal stress (up to ∼100 Pa) along the curvature of the blade. High velocity regions (between 5 to 8 m/s) at the mid-section of the impeller and housing also experienced shear stress. In the diffuser section, the highest normal stresses are between the hub and the blades (up to ∼50 Pa).

Both VADs clearly experienced higher shear stress over a larger volume as compared to normal stress. In the HVAD the volume at 10 Pa was almost two orders of magnitude higher for shear stress compared to normal stress (0.74 cm^3 compared to 0.011 cm^3) while at 100 Pa the difference is three orders of magnitude (0.020 cm^3 compared to 0.000015 cm^3). In HM 2 the differences between shear and normal stress volumes were similar, with the shear volume still always larger (0.86 cm^3 compared to 0.027 cm^3 at 10 Pa, and 0.10 cm^3 compared to 0.00077 cm^3 at 100 Pa). Both shear and normal stress volumes were larger in the HM 2 compared with the HVAD. The internal fluid volumes of the two VADs are similar: the HVAD is 12 cm^3 and the HM 2 is 7 cm^3.

4.4.1 Cell and Protein Deformation Threshold Volumes

Literature suggests lower normal stresses cause cell deformation and protein unravelling, compared with shear stress, the fluid volume was thresholded based on RBC and vWf deformation. For cell deformation, the values used were 13.4 Pa for shear stress and 1.8 Pa for normal stress (**Figure 4.14**). In the HVAD the RBC deformation volume was larger for shear stress as compared with normal stress (0.61 cm^3 compared to 0.46 cm^3) whereas in the HM 2, the shear stress volume was smaller than the normal stress volume (0.46 cm^3 compared to 0.80 cm^3). The vWf deformation volume was much larger for normal stress as compared with shear stress: 5 times the size (0.99 cm^3 compared to 0.18 cm^3) for the HVAD and 2.5 times the size (0.75 cm^3 compared to 0.31 cm^3) for the HM 2.

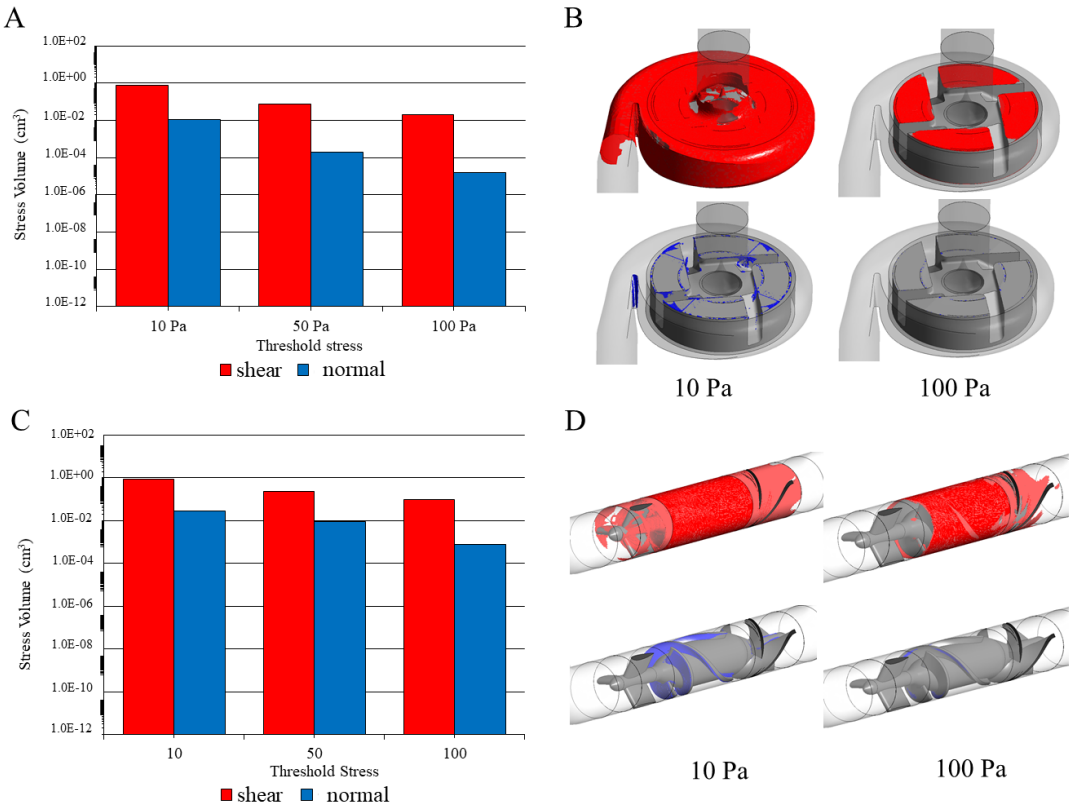

Figure 4-13: A. Shear and normal stress volumes in HVAD (centrifugal VAD) for blood damage threshold stress values, B. Regions of HVAD (centrifugal VAD) with a threshold above 10 and 100 Pa, C. Shear and normal stress volumes in HM 2 (axial VAD) for blood damage threshold stress values and; D. Regions of HM 2 (axial VAD) with a threshold above 10 and 100 Pa.

Based on the threshold for vwF deformation (shear at 35 Pa; normal at 0.7 Pa), the variation in cell deformation volume over time as the impeller rotates was investigated by plotting the volumes every 20° interval (which is every 10th-time steps or 1.1 ms) to monitor the volume of stresses changing with time. The cell deformation volume due to shear stress was constant over time. The shear stress occurred mostly in the gap clearances above and below the impeller which do not change with time (as shown in **Figure 4.15**). The cell deformation volume due to normal stress was a repetitive continuous wave because of the rotating impeller with a peak volume of 0.47 cm^3 and minimum volume of 0.45 cm^3. The peak occurred at 60°, which corresponds to the blade passage pointing directly at the cutwater. In **Figure 4.16**, recurring regions of normal stress at this threshold

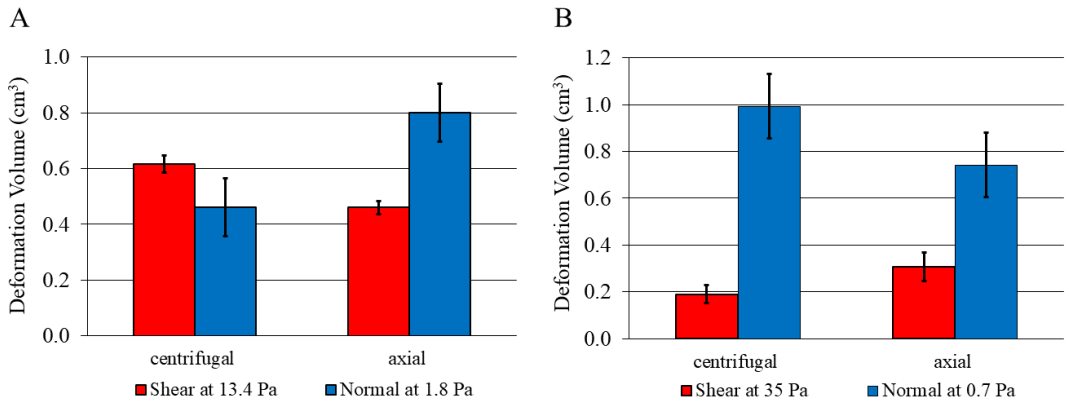

Figure 4-14: A. Mean RBC deformation volumes and; B. vWf deformation volumes over time, with error bars showing standard deviation.

occurred in the volute, at the wall of the impeller, and in between the blades along the slope. Single threshold values for cell deformation do not account for the real damaging effects in the centrifugal VAD, but this method of characterising stresses remains a simple and expressive approach to comparing the volume of stresses as a point of indication for potential blood damage.

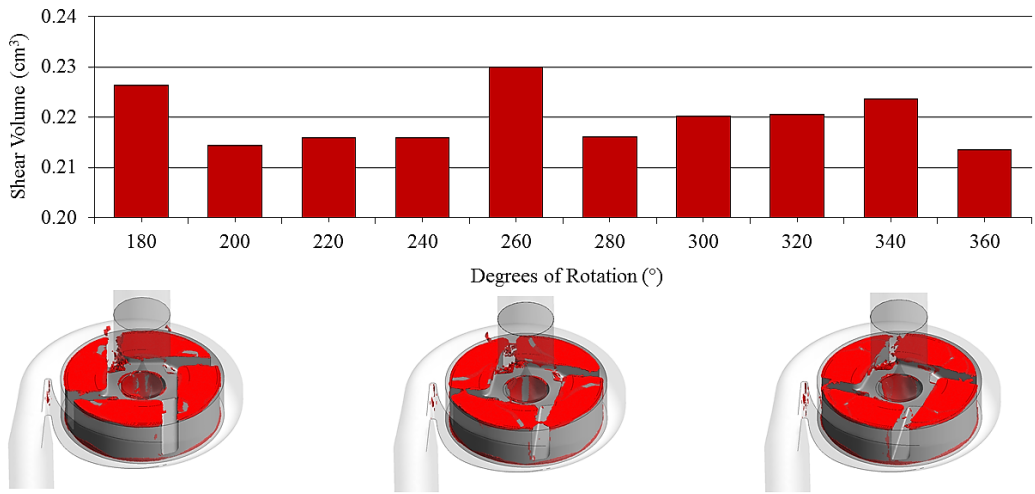

Figure 4-15: Shear stress volume with threshold for vwF deformation (shear at 35 Pa), respect to time at every 20° (figures below represent 180°, 260° and 340°).

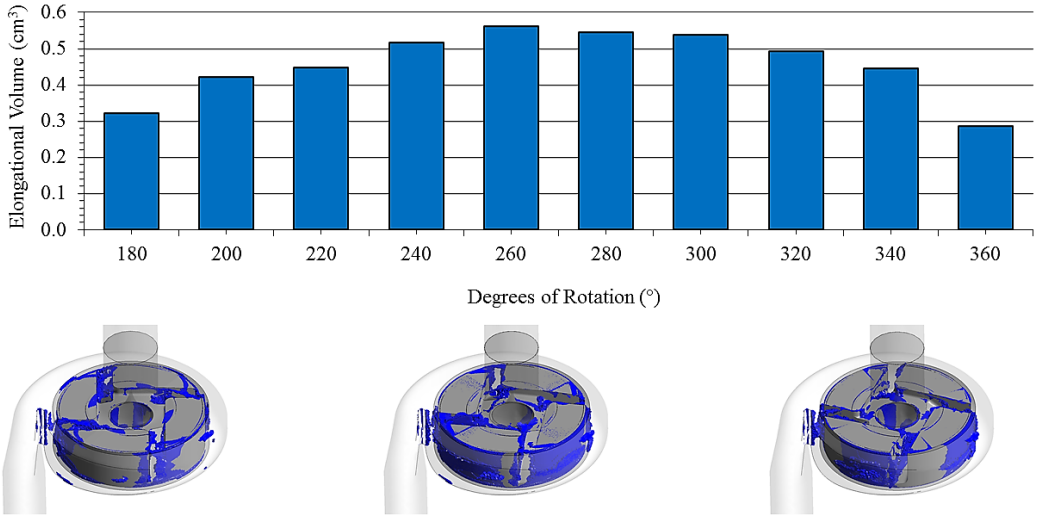

Figure 4-16: Normal stress volume with threshold for vwF deformation (normal at 0.7 Pa), respect to time at every 20° (figures below represent 180°, 260° and 340°).

4.4.2 Exposure times

Using the pathline-based approach, the mean exposure times of blood in the two VADs to levels of normal and shear stress sufficient to deform RBCs and vWf were found (**Table 4.1**). The duration of exposure to shear stress is clearly longer than that to normal stress; however, the exposure times for normal stress were not insignificant at around 1 – 2 ms depending on the VAD and blood component of interest. It is also worth noting that while the shear stress exposure times were almost identical for both VADs, the normal stress exposure times in the HM 2 were double those in the HVAD. Considering only the shear stress in the VADs would make these two appear similar, in terms of damage performance, which could imply that potential differences in their safety, related to the normal stress, would be missed.

4.4.3 Influence of Operating Conditions

The difference in the cell deformation volume was investigated for varying operating conditions (**Figure 4.17**). As the rotational speed was increased, with a constant flow rate of 5 l/min, the cell deformation volumes for both normal and shear stress increased with the normal RBC deformation volume reaching

Table 4.1: Mean exposure times of blood to the stress levels required to deform RBCs and vWf.

Blood component	VAD	stress	time /ms
RBCs	HVAD	normal (1.8 Pa)	0.87
		shear (13.4 Pa)	12
	HMII	normal (1.8 Pa)	2.1
		shear (13.4 Pa)	12
vWf	HVAD	normal (0.7 Pa)	1.1
		shear (35 Pa)	8.6
	HMII	normal (0.7 Pa)	2.5
		shear (35 Pa)	8.2

0.50 cm^3 and shear volume reaching 0.63 cm^3 at a speed of 3400 rpm. The pathline analysis showed that the exposure times for the normal stress deformation volumes were roughly constant with changes in speed whereas the exposure times for the shear stress deformation volumes decreased by a factor of two between 2200 and 3400 rpm.

The deformation volumes also depended on the flow rate. Increasing flow rate from 3 to 7 l/min, with impeller speed constant at 3000 rpm caused a tiny increase in shear stress volume from 0.58 cm^3 to 0.64 cm^3. The influence of flow rate on elongational cell deformation volume was more significant: the increase from 3 l/min to 7 l/min caused the RBC deformation volume to increase from 0.39 cm^3 to 0.54 cm^3. In the case of flow variation, the pathline analysis showed the opposite trends as compared to those for speed variation. The exposure times for the shear deformation volumes were constant with changes in flow, likely because the small increase in the size of the deformation volume was countered by the increasing average speed through the VAD with flow rate. However, the exposure times for normal stress deformation volumes increased by a factor of five between 3 and 7 l/min, showing the larger increase in the size of the deformation volume was the important effect in this case.

4.4.4 Influence of Axial Clearance Gap

The HVAD impeller is hydrodynamically suspended, so the clearance gaps vary with operating conditions. The gap used in the study was 20 μm [85] but to assess the impact of any possible error, the gap was varied from 20 to 100 μm in **Figure**

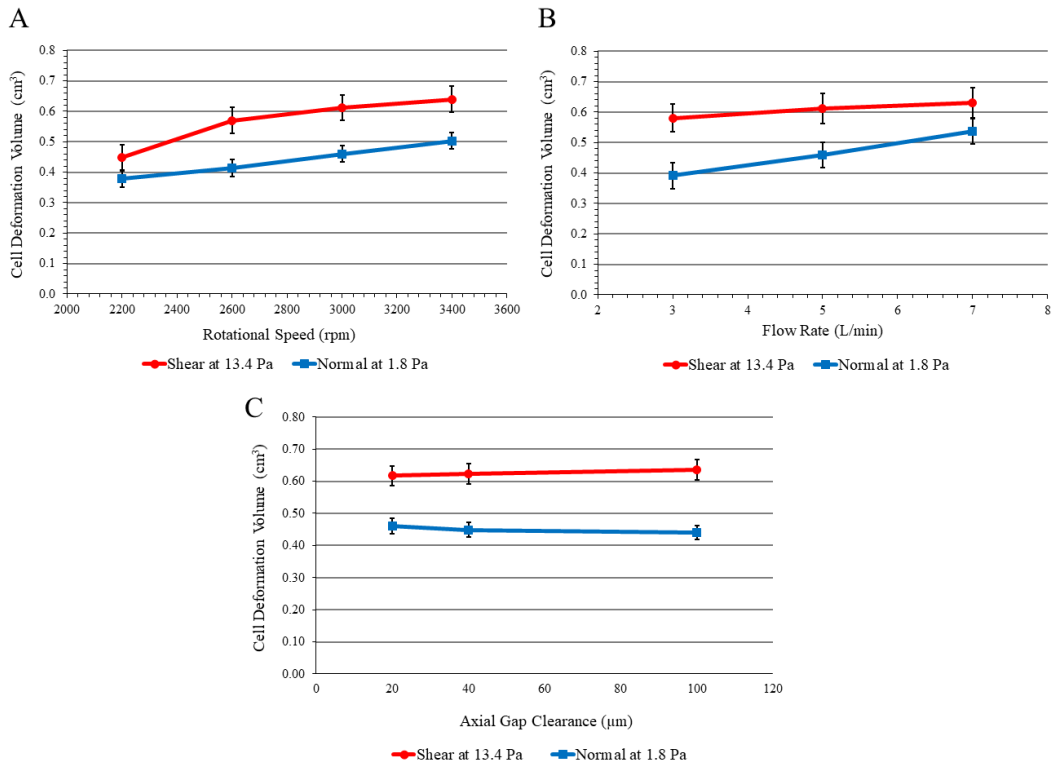

Figure 4-17: Mean variation of RBC deformation: A. Impeller speed, B. Flow rate and C. Axial gap clearance. Error bars show standard deviation in mean.

4.17 (with the operating condition: 5 l/min at 3000 rpm). The cell deformation volume due to normal stress decreased slightly (from 0.46 cm^3 to 0.44 cm^3) as the axial gap clearance increased, whereas the cell deformation volume due to shear stress remained constant. This difference did not cause a change in the exposure times and is not enough to influence the conclusions.

4.5 Discussion

Fluid stresses are well known to be a major cause of blood damage in rotary VADs [88]. As discussed in section 2.4, the different components of the stress deform and damage the blood components differently, with normal stress causing larger cell and protein deformations at smaller stress magnitudes as compared with shear stress [68, 77, 95, 96]. There have been many studies measuring the

effects of shear stress on blood damage [47, 48, 67, 97], but far fewer on the effects of normal stress [69, 98]. Before embarking on such studies we wanted to find out how significant the problem of normal stress in rotary VADs might be. Therefore, the aim of this study was to assess the prevalence of normal stress as compared with shear stress in the most commonly implanted rotary VADs. CFD calculations were performed for the HVAD, a centrifugal blood pump, and the HM 2, an axial blood pump, and the normal and shear stresses were calculated.

The results of the calculations showed there are large regions experiencing high shear stress magnitudes in both VADs: the volume above 10 Pa was 0.74 cm^3 (6.2 %) and 0.86 cm^3 (12 %) for the HVAD and HM 2 respectively. A value of 10 Pa is above the level of the WSS in the vast majority of the normal healthy cardiovascular system [99]. The volumes with shear stress above 50 Pa, which is well above the WSS in the whole normal circulation were 0.075 cm^3 (0.63 %) and 0.228 cm^3 (3.3 %) for the HVAD and HM 2 respectively. The volumes above 100 Pa, enough to cause haemolysis, were 0.020 cm^3 and 0.03 cm^3.

In contrast, the volumes experiencing normal stress at the same threshold values were much smaller: above 10 Pa the volumes were 0.011 cm^3 (0.092 %) and 0.027 cm^3 (0.39 %) for the HVAD and HM 2 respectively. A 10 Pa normal stress is sufficient to cause maximal cell deformation [68] and protein unravelling [77]. The volumes with normal stress above 100 Pa were 0.000015 cm^3 (1.3 $\times 10^{-4}$ %) and 0.00077 cm^3 (0.011 %) for the HVAD and HM 2. So, the shear stress magnitudes are clearly greater than normal stress magnitudes, and the volume of the fluid domain experiencing these high values is larger for shear stress than for normal stress. This is logical since the devices are rotating with small gaps that create a shearing action. Available data for the effects of normal stress on haemolysis come from Down *et al* [69] and Yen *et al* [98] The study by Yen *et al* [98] implies normal stress of at least 1000 Pa is required to cause 1% haemolysis. However, the exposure time is lower in both of these capillary entrance experiments [69, 98] as compared with the VADs, in which recirculation is also possible. The residence time in the very high normal stress regions ($> 1000Pa$) in these works can be estimated as 0.00317 and 0.06 ms [98] in contrast with average times of 0.87 to 2.1 ms in the cell deformation regions found here, and with average total times of 144

and 84 ms in the HVAD and HM 2 respectively [83] There are no experimental studies which measured thresholds for haemolysis with normal stress exposure times around 1 ms.

Given that the available literature for cell and protein deformation [68, 77] shows that these deformations occur at lower normal stress magnitudes than shear stress magnitudes, the fluid volumes were thresholded according to deformation. When the RBC deformation threshold of DI = 0.5 was applied, the cell deformation volumes were 1.5 to 2 times larger for normal stress as compared with shear stress. The exposure times were smaller for normal stress, between 0.87 and 2.1 ms, which is 7% to 17% of the shear stress times. These normal stress exposure times can be compared with estimated exposure times from the work by Yaginuma *et al* [95]. Based on the data given in that work, the exposure time for cells to reach DI = 0.35 was 1.7 ms and therefore, the exposure times calculated here are likely to be sufficient to cause cell deformation. Differences in deformation volume were even more pronounced when considering vWf deformation: when the vWf extension threshold of 27% was applied, the vWf deformation volumes were 5 to 20 times larger for normal stress as compared with shear stress. Again the exposure times were smaller for normal stress, between 1.1 and 2.5 ms, which is 12% to 30% of the shear stress exposure times. There are no studies of exposure time on vWf deformation to compare with. To compare our simulations with those already published, we calculated the SSS [4] a scalar invariant quantifying the stress magnitude.

$$\sigma_{SSS} = \left[\frac{1}{6}\left((\sigma_{11}\sigma_{22})^2 + (\sigma_{22} - \sigma_{33})^2 + (\sigma_{33} - \sigma_{11})^2\right) + (\sigma_{12} + \sigma_{23} + \sigma_{13})^2\right]^{\frac{1}{2}} \tag{4.1}$$

The volumes of SSS were in good agreement. For HM 2, the volume above 9 Pa was 1.6 ml, compared to 1.7 ml [100] and 2.1 ml [88] and at 50 Pa was 0.32 ml, compared to 0.3 ml [100] and 0.42 ml [88]. This investigation showed that normal stresses are present in rotary VADs. Furthermore, while the magnitudes and exposure times for the normal stresses are lower than the shear stresses, there is sufficient normal stress magnitude, for a long enough exposure time, to cause cell and protein deformation. This finding suggests that damage to the blood components caused by the normal stress components is an important con-

sideration for the design of VADs and the development of blood damage models. The results of our investigation then justify further experimental studies into the effects of normal stress, and normal stress in combination with shear stress, on the blood components. The results of these future experiments would enable the proper incorporation of the effects of normal stress into numerical blood damage models.

4.5.1 Limitations

This investigation was designed to calculate normal stress experienced by blood in the direction of the flow, analogous to the type of normal stress experienced when blood enters a narrow constriction, such as at the entrance to a needle or through arterial stenosis. From the literature, this type of normal stress stretches RBCs, in the direction of the flow, and unravels vWf. The study was not designed to calculate normal stress in the directions perpendicular to travel. This type of normal stress would be experienced by blood when the shape of the channel changed, such as if the shape of a channel changed from a vertical to a horizontal slot of the same cross-sectional area. It seems possible that this type of normal stress would similarly deform RBCs, elongating them perpendicular to the direction of travel. However, there are no experimental results in the literature related to this scenario. Furthermore, blood damage effects, including RBC deformation and the unravelling of vWf molecules, depend on changes in fluid stress with time, which occur due to the blood transiting regions with spatial shear stress gradients. These effects were not the subject of this study but could be investigated in future, using particle-based models (see for example [101–103]).

As explained in section 3.3 the unsteady Reynolds Averaged Navier-Stokes equations were solved with the SST k-ω model for turbulence. This was because, with a 5 l/min flow rate, Re at the straight tube inlet was 2530, which is above the critical threshold for transition to turbulence in a straight tube, usually taken to be 2300. However, turbulence models are designed for high Re turbulence, which could result in some errors in the mean flow field. These are likely to be small and would affect both shear and normal stresses similarly. The turbulent shear and normal stresses (components of the Reynolds stress) were not included in this investigation since the literature on the effects of turbulent stresses is incon-

clusive.

Blood is well known to be a multiphase, shear-thinning fluid, however, in this work, it was treated as a single-phase Newtonian fluid. The shear-thinning viscosity has the potential to increase shear rates near the walls which would have a small effect on the shear stress calculation. Additionally, haematocrit in the gap regions between the impeller and housing has been shown to be lower compared with that in the bulk flow [104]. This causes reduced viscosity in these regions so would reduce the, predominantly, shear stresses found there.

Pathlines calculated from one simulation timestep were used to estimate the duration of exposure of blood to the various stress threshold levels. Since these are transient simulations a more correct approach would have been to calculate time dependent particle tracks, initiated from the inlet of the flow domain and tracked with the flow to the outlet. However, only a small portion of the flow passes through the high stress regions, many of which are located in the secondary flow path, so in order to achieve a representative number of tracks which encountered these high stress regions a vast number more would need to have been seeded. We used 2000 pathlines, but with particle tracking, the number of particle tracks initiated from the inlet would have had to be much larger. The pathline approach is justified in this work since the maximum exposure time for normal stress is equivalent to 45° rotation of the impeller which, with the exception of the region near the cut water, has only small changes in the velocity field. The pathline-based approach is therefore likely to be most accurate for the normal stresses but might overestimate the exposure to shear stresses which have longer exposure times over which the velocity field would change more. It is also important to note that the method only looked at exposure to individual high deformation regions. In reality, the blood components would be exposed to multiple regions of high stress, so the total exposure times would be considerably longer.

4.5.2 Conclusion

Based on these calculations, normal stresses do occur in rotary VADs. The fluid volume experiencing normal stress above 10 Pa was 0.011 and 0.027 cm^3 for HVAD and HM 2, respectively. Although the fluid volumes experiencing normal stress were smaller than those experiencing shear stress, for all threshold stress

values (10, 50 and 100 Pa), normal stress volumes were in existence and were not negligible. When thresholds for RBC and vWf deformation were considered, the fluid volumes experiencing significant deformation were larger for normal stress as compared with shear stress. Exposure times to the shear stress deformation regions were larger than exposures to the normal stress deformations; nevertheless, the normal stress exposure times were between 0.87 and 2.5 ms which are sufficient to cause cell and protein deformation. In conclusion, the fluid within rotary VADs experiences more shear stress at much higher magnitudes as compared with normal stress. However, there is a significant volume of normal stress, with a magnitude and exposure time large enough to cause RBC and vWf deformation, which means that the normal stresses present are likely to be an important contributor to blood damage in rotary VADs. Further experimental studies into the effects of normal stress on the blood components are required, and these can then be used to properly incorporate the effects of normal stress into numerical blood damage models.

Chapter 5

The influence of flow pulsatility in LVADs

There are post-surgical complications related to the non-physiological flow conditions experienced by blood in the VADs implanted. VADs are designed for specific operating conditions and are optimized in the steady-state. However, the flow rate through the VAD is pulsatile due to the beating heart. This chapter covers the investigation of the effect of realistic flow conditions, and thrombosis potential was assessed by the size of recirculation regions.

I was able to carry out flow field investigations on the influence of flow pulsatility on flow properties such as wall shear stresses and deformation volumes. In Chapter 4, steady blood flow through the VADs was simulated using the transient rotor-stator (TRS) method. Alternative methods for simulating turbomachinery are frozen rotor methods, in which flow near the rotor is solved in a rotating reference frame while flow near the stator is solved in the absolute, or stationary, reference frame. Between coupling of both parts at the interface, produced a flow field dependent on the relative position of the impeller and the volute. The computational cost for the technique is typically a factor of 30 larger than the effort for a frozen rotor technique [105]. Initially, the application was explored to know how realistic the profiles are in a steady flow. The quantities and regions of shear and normal stress were calculated and compared using each of the different turbomachinery methods.

To account for pulsatile flow from the beating heart, pulsatile flow and pressure boundary conditions from the literature were applied and compared with steady flow conditions. Streamline plots were used to compare the size and location of recirculation zones between the steady and pulsatile flows. Then, the size of the shear and normal stresses were also compared.

5.1 Frozen Rotor and Sliding Mesh

5.1.1 Pressure and Velocity Profile

The pressure variation across the time of one cardiac cycle is shown in **Figure 5.1 A** comparison to the experimental result from Noor *et al* [92]. As described in the "Methods", the flow rate against cycle time from the literature was used as the inlet boundary condition to mimic pulsating flow. During the flow acceleration phase, the simulated pressure heads are lower than those simulated for the flow deceleration phase. Derived from HQ data, frozen rotor and sliding mesh approaches lead to underprediction of the pressure head at the start of systole and as flow rate decelerates (**Figure 5.1 B**).

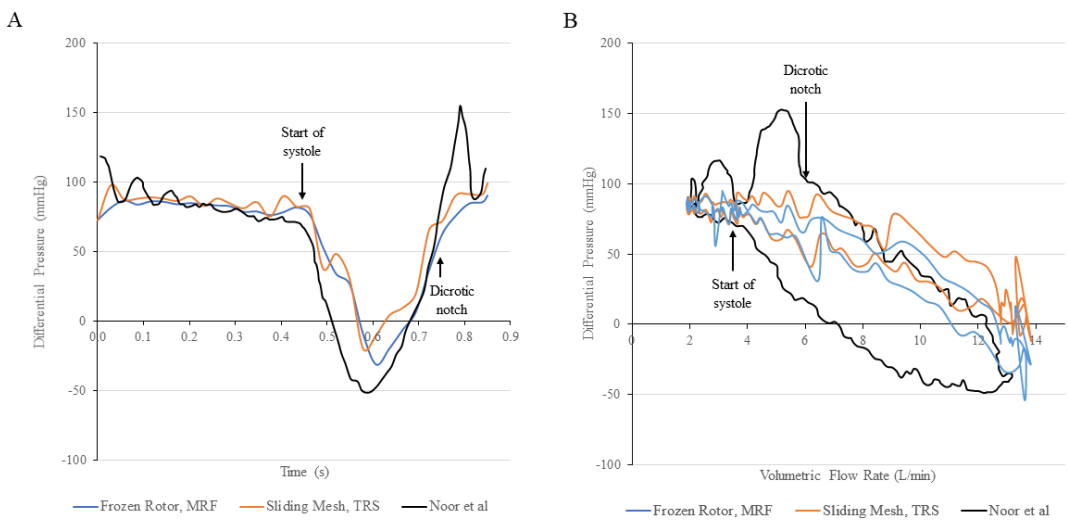

Figure 5-1: A. Differential pressure as a function of Time: Frozen Rotor and Sliding Mesh predictions, and; B. Steady flow left ventricular assist device (LVAD) differential pressure versus flow rate (HQ) relationship for the HVAD, depicted by the black solid line.

The pressure and velocity profiles extracted from both approaches were statistically time-averaged over multiple cardiac cycles which were done to obtain the average flow property in a transiently varying flow. The pressure distribution and velocity field are compared in **Figure 5.2** for an average flow rate of 5 l/min. The pressure distributions obtained from both calculations are not identical, but the general behaviour is the same. With the frozen rotor, the negative pressure results in low velocities where the interface tends to overestimate the pressure difference (**Figure 5.2 A**, Region 2). Low velocities can be found in the region near the outlet provided by the rotating impeller itself. This can be seen especially for the frozen rotor interface where the negative pressure rises in the case of the one relative position of the rotor and stator being calculated (**Figure 5.2 C**, Region 1). This is an important finding as it shows that the simulation model reveals some sensitivity in predicting absolute pressure values when rotational effects dominate over the pressure loss [106].

Meanwhile, the sliding mesh approach shows that the distribution of the pressure and flow over the impeller and volute is most homogeneous, though not uniform. The non-uniformity is mainly caused by geometrical asymmetry of the volute and static interference [107]. The increase in pressure in the volute is the centrifugal force generated by the rotation of the impeller. The pressure increases along with the passage and reaches the maximum at the trailing edge (**Figure 5.2 B**, Region 2). An adverse pressure gradient occurs when the static pressure increases in the direction of the flow. With frozen rotor, the rotor stands still, and flow separates from the blades as the impeller stays localised in the volute space after the intersection at the outlet. For either of the two positions of the impeller, a wake causes an unphysical flow separation on the sides of the upper and lower wall of the impeller (as shown in **Figure 5.2 C**, Region 1). In reality, this does not happen since wakes are largely mixed in the volute and are unsteady (**Figure 5.2 D**, Region 1). No localised separation occurs in the impeller.

5.1.2 Fluid Stress Threshold Volumes

The difference in fluid stress volumes is investigated for both approaches in **Figure 5.3**. As the flow rate increases (t = 0.5 s), with a pulsatile inlet flow of

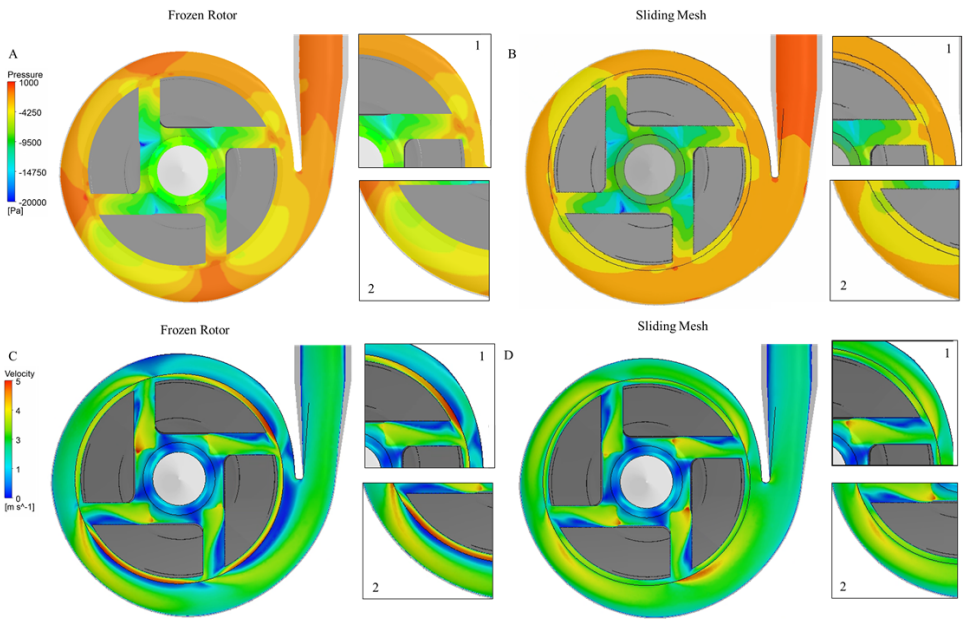

Figure 5-2: Distribution of average static pressure (top) and absolute velocity (bottom) in the midplane for HVAD at 2600 rpm for different turbomachinery modelling: (left) frozen rotor with MRF and (right) sliding mesh. There is a wake that shed from the blades of the impeller and stays localised in the volute space after the intersection at the outlet at **Figure C, Region 1**.

an average of 5.5 l/min, the cell deformation volumes for both shear and normal stress increase. Changing the flow rate from constant 5 l/min to pulsatile flow varying from 2 – 14 l/min, with a constant impeller speed of 2600 r/min didn't influence shear stresses (10 Pa and 100 Pa). During the phase of the cycle where the flow rate is quite constant (between 0.1 and 0.5 s), the volume at 10 Pa was almost two orders of magnitude higher for shear stress compared to normal stress (0.70 cm^3 compared to 0.01 cm^3) while at 100 Pa the difference is three orders of magnitude (0.018 cm^3 compared to 0.00008 cm^3). And during the phase where the flow rapidly increases and then decreases (0.5 to 0.75 s), the differences between shear and normal stress volumes are similar.

At peak flow (0.65 s), the volume for normal stress using the frozen rotor approach at 10 Pa was almost two orders of magnitude higher compared to sliding mesh (0.050 cm^3 compared to 0.045 cm^3) while at 100 Pa the difference between both approaches stress volumes is similar. This is because the highest amount of fluid stresses (shear and normal stresses) was discovered that the narrow axial

hydrodynamic bearing gap clearance (20 μm) up to 100 Pa. The influence of both approaches was more significant for normal stresses on cell elongation, at a higher flow rate during systole displayed in **Figure 5.3 C**.

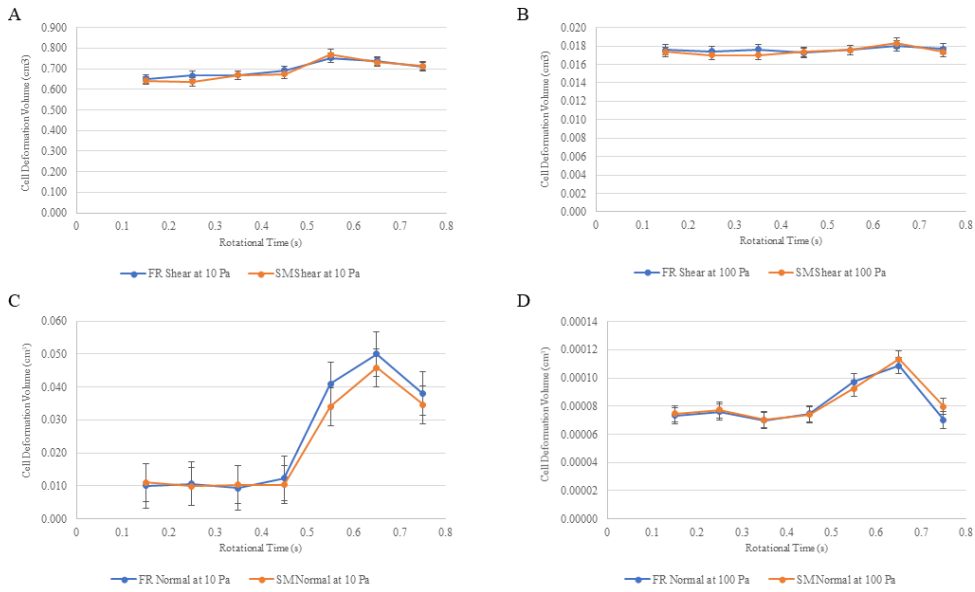

Figure 5-3: Shear (top) and normal (bottom) stress volumes in HVAD for blood damage threshold stress values through one cardiac cycle. The difference in colour shows the difference between which rotor-stator interaction was used.

It is observed that the normal stresses trail over the edge of the impeller blades and small regions at the tip of the leading edge of the blade. It is also frequently found in the inter-blade passages in **Figure 5.4** where the recirculation zone narrows the pathway and forces fluid through.

The increase in shear stress distribution appears at the interface of rotor and stator and impeller clearance. Normal stresses appear to be significantly affected by the increase in flow separation. Compared to the sliding mesh approach, the frozen rotor approach calculates the non-uniform circumferential velocity and pressure distributions to accurately predict the wake mixing in the downstream rotor and rotor-to-rotor flow physics. Of both methods, the moving mesh method produces accurate, realistic flow physics by employing the unsteady coupling of the rotors.

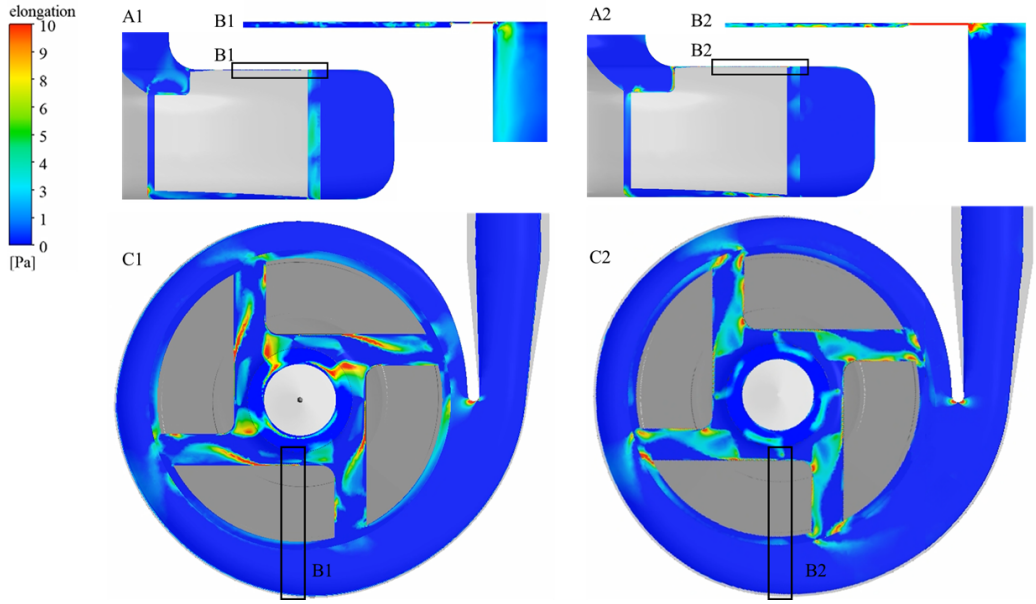

Figure 5-4: Time average of the transient results for normal stress distribution at the midplane of HVAD. (left) Frozen Rotor. (right) Sliding Mesh.

5.2 Transient State Result Analysis

5.2.1 Primary Flow Path

As discussed previously in section 3.4.2, the inlet boundary condition for steady flow was mass flow rate, fixed to give flow rates of 3, 5 or 7 l/min with varying speeds. However, the critical question arises on the representation of steady (non-pulsatile) flow conditions and are such data clinically representative of LVAD in a heart. For pulsatile flow in section 3.4.3, the inlet boundary condition was characterised more physiologically to represent pulsatile flow conditions both the arterial compliance and the anatomy and function of the left heart must be appropriately modelled. The flow patterns for steady and pulsatile flow are similar in that recirculation regions occur in similar places (**Figure 5.5**) before systole and at the dicrotic notch, the size of these regions does differ and as the pulsatile flow varies throughout the cycle (**Figure 5.6**).

Before systole (t = 0.45 s), the vector plot of relative velocity shows large recirculation zones that can be seen in the impeller channels exposed to the largest volute pressure. Flow velocities are very low in these channels. The flow vectors

at the periphery of the impeller point inwards, so in the mean, there is reversed flow in these channels. The impeller channels exposed to the lowest volute pressure have a flow that is well aligned with the impeller blades. As the flow rate increases, the recirculation zones become smaller, however, the areas of flow separation observed at the trailing edge of the blades get larger as the flow rate accelerates and achieves peak flow (t= 0.45 - 0.55 s). From t = 0.65 - 0.75 s, the flow rate decelerates with time and the region of flow disturbances decreases.

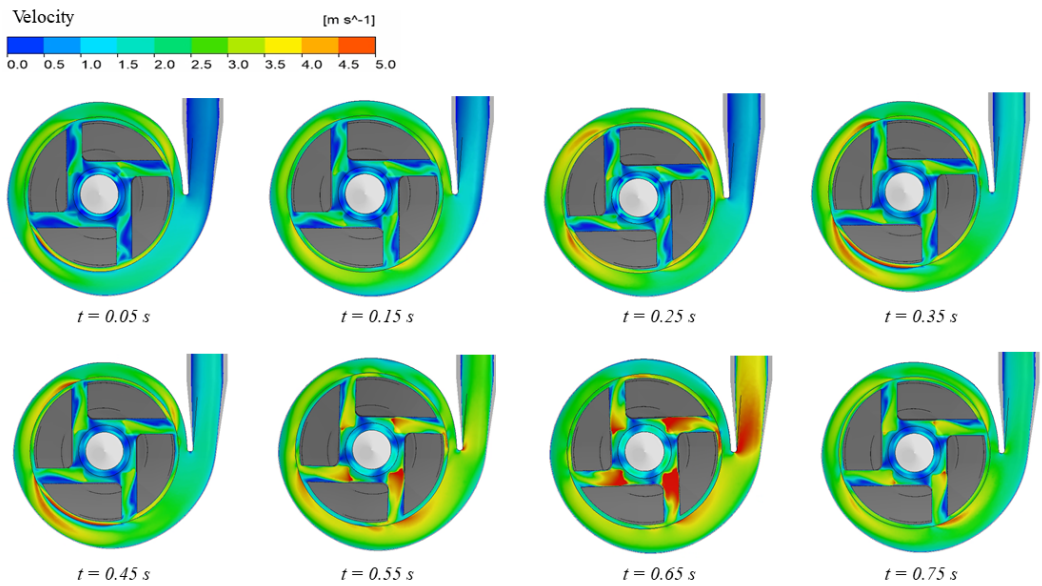

Figure 5-5: Change of flow velocity in the flow domain around the impeller at various time points in the cardiac cycle at a constant speed of 2600 rpm.

To further analyse the velocity profiles in the blood pump, the proportions of fluid at different flow rate ranges were extracted, and the selection of time points was based on systolic accelerating flow, peak flow, and decelerating flow. Flow detachment or strong recirculation was observed formerly in steady flow inside the blade channels (**Figure 5.6 A**, Marker A1, and A2). During systole at 0.55 s, the recirculation zone minimises as the pressure difference between the blades leading edges and volute is overcome by increasing flow rates. At the peak flow, it is noticed at the outlet (**Figure 5.6 B**, Marker B3) that the stagnation point at the flow divider between the outlet and re-entering the volute is more evident. These effects are temporary as in decelerating flow (t = 0.75 s) the profiles of both flow conditions are similar.

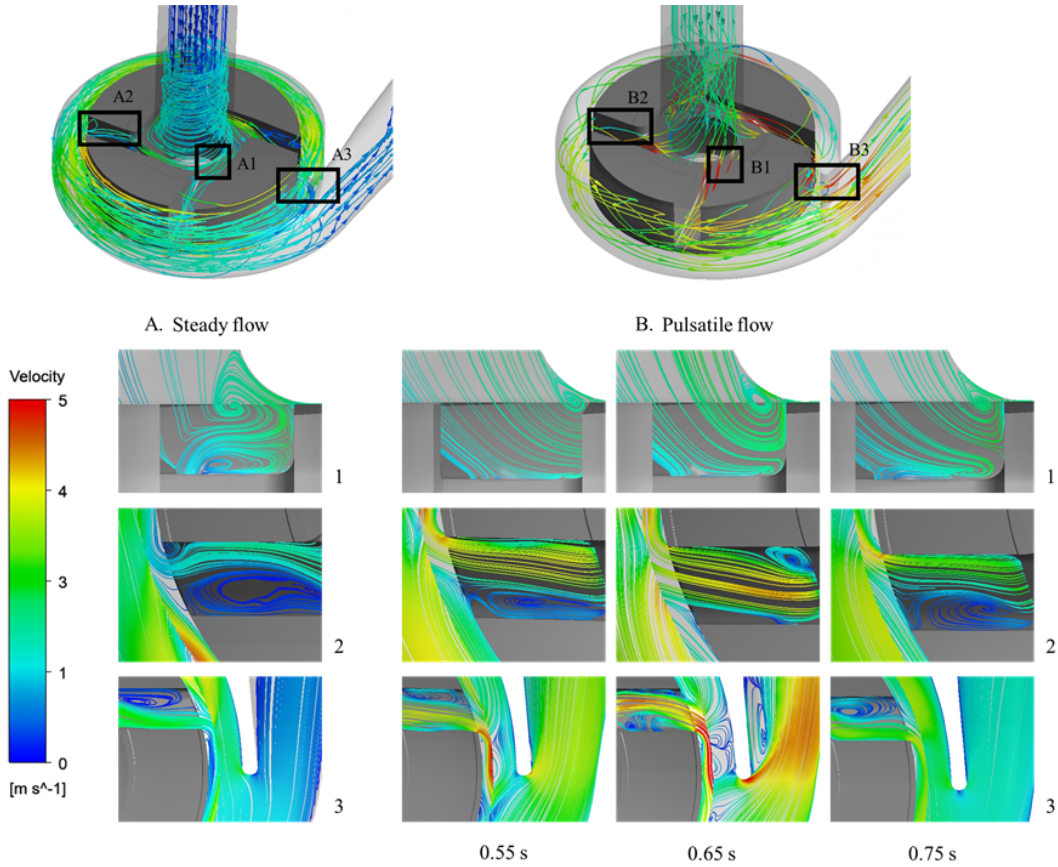

Figure 5-6: Typical streamline regions of the relative velocity for: A. Steady flow. B. Pulsatile flow at accelerating flow (t = 0.55 s), peak flow (t = 0.65 s) and decelerating flow (t = 0.75 s).

5.2.2 Secondary Flow Path

A secondary flow path exists in the gap between the rotating impeller and lower housing and the central magnetic strut. In steady flow or before systole, the secondary flow intersects the main flow near the leading edge due to the pressure difference between the volute. This causes a small portion of the fluid to flow back and reenters the channels through the gaps between the impeller and the bottom housing and between the impeller and the central strut (**Figure 5.7 A**). During systole, the flow is accelerated through the impeller blades, and this causes high pressure at the volute. This decreases the amount of flow passing through the secondary pathway as it reaches peak conditions (**Figure 5.7 B - C**). As the flow decelerates, the pressure difference between the impeller leading edge and

volute is restored as flow is seen passing through the secondary pathway (**Figure 5.7 D**).

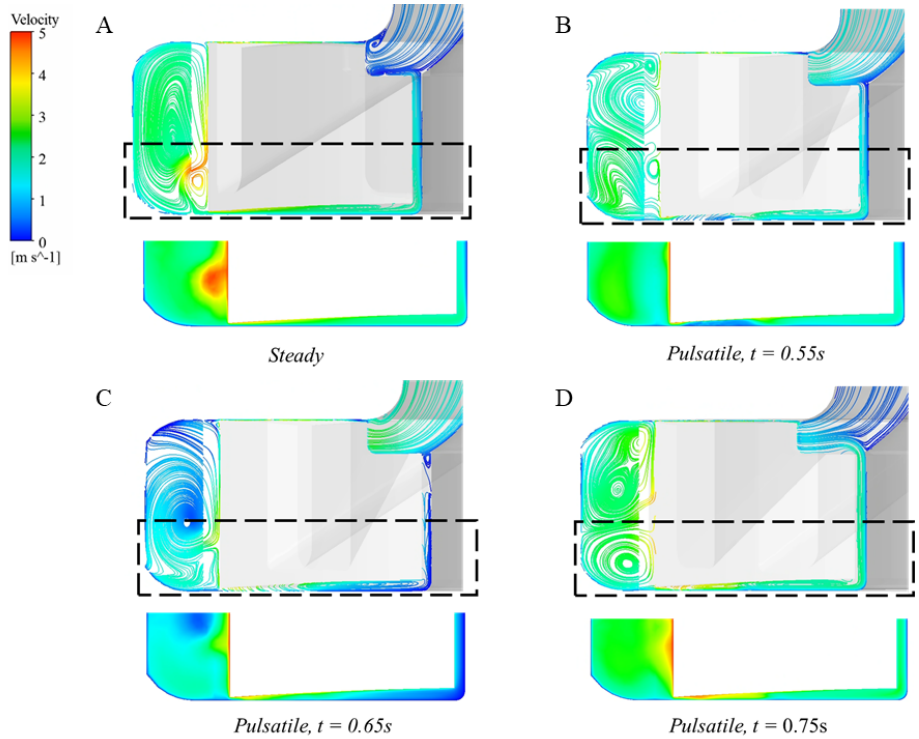

Figure 5-7: The difference in streamlines of the relative velocity for the HVAD at constant 2600 rpm with an average flow rate of 5 l/min. A. Steady flow (Non-pulsatile). B. Pulsatile flow at peak systole, t = 0.65 s. The dotted box represents the velocity contour plot of the secondary flow path under the impeller.

5.2.3 Fluid Stresses Threshold Volumes

The highest shear stress was similarly highlighted at the hydrodynamic bearing gap of 20um clearance for both flow conditions in **Figure 5.8**. High shear stress in this region between 100 - 1000 Pa is approximately 12%, mostly also occupying regions in the gap under the impeller. In both steady and pulsatile flow, the range of shear between 10-100 Pa exists as wall shear stress on 40% of the impeller surface. However, there was also a region of high shear within the blade passage (steady) and along the side of the impeller wall (pulsatile). The bulk of the volute experienced shear stress in the range lower than 10 Pa.

Similarly in **Figure 5.9**, the highest normal stresses were also spotted at the

hydrodynamic bearing clearance. This normally occurs at the gap where blood leaks over the edge of the impeller blades and tips of the leading edge. Normal stresses above 100 Pa is negligible as the volume appearing on the impeller is too small. Mainly the stresses appeared more evidently at the clearance between the impeller and top housing. The majority of the impeller (approximately 96% impeller surface) does experience low normal stresses.

Flow condition	Shear stress volume		Normal stress volume	
	10 Pa	100 Pa	10 Pa	100 Pa
Steady flow	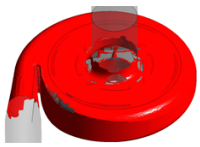	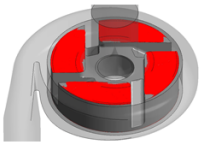	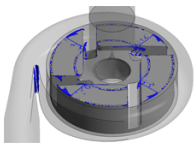	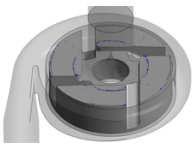
Pulsatile flow	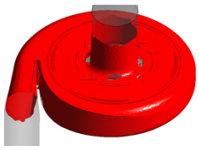	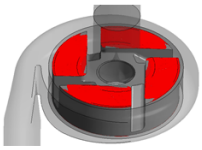	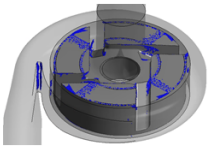	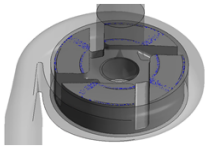

Figure 5-8: Time-averaged volume of regions of HVAD with thresholds above 10 and 100 Pa in different flow conditions.

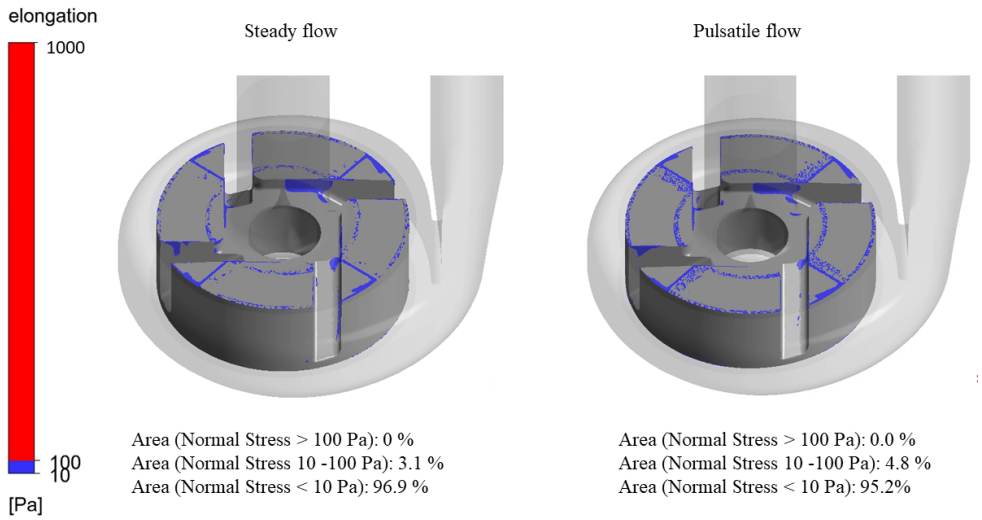

Figure 5-9: Time-averaged volume of normal stress distribution on the impeller surface for steady (left) and pulsatile flow (right)

5.2.4 Cell and Protein Deformation Threshold Volumes

Based on **Figure 5.10**, there's a difference between steady and pulsatile flow at the inter-blade passage where the recirculation zone is more significant in pulsatile flow. This increases the forward flow in the narrow passage, thus increasing the occurrence of normal stresses up to around 15 Pa. Ultimately, the high shear and normal stresses both exist in both flow conditions at the stagnation point at the flow divider between the outlet and re-entering the volute. In general, blood in VAD still experiences higher shear stress over a large volume as compared to normal stress. However, in the HVAD, the pulsatile flow shear stress volumes at 10 Pa, 50 Pa and 100 Pa were similar to a steady flow. While for normal stress, there was a ratio of 4:1 magnitude between pulsatile flow (0.024 cm^3, 0.00040 cm^3 and 0.00008 cm^3) to steady (0.0083 cm^3, 0.00015 cm^3 and 0.00002 cm^3). At a steady flow rate, the calculations showed normal stresses do occur in rotary VADs: the fluid volumes experiencing normal stress above 10 Pa were 0.0083 ml (0.069 %) and were present in the HVAD. In pulsatile flow, the normal stress volumes were higher above the 10 Pa threshold which was 0.024 ml (0.2 %). There is an increase in 2 orders of magnitude of normal stress compared with steady flow at peak flow, which existed in the clearance between the top housing and rotating impeller.

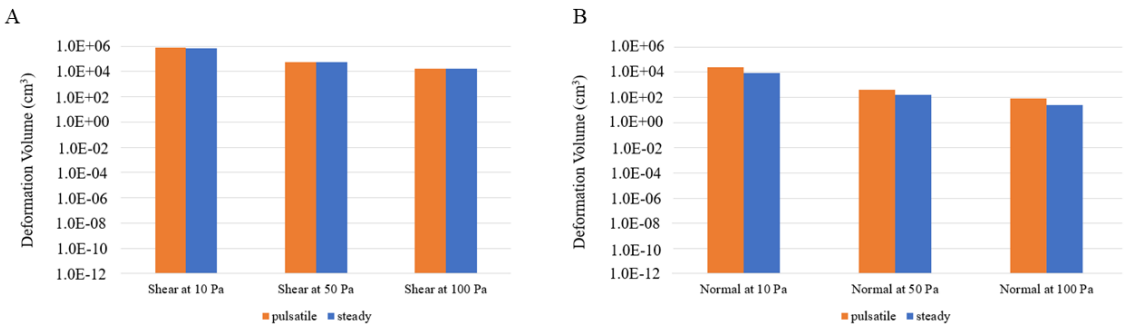

Figure 5-10: Deformation volumes for blood damage threshold stress values between the pulsatile and steady flow. A. Shear stress and; B. Normal stress.

For cell deformation, the values used were 13.4 Pa and 35 Pa for shear stress; and 0.7 Pa and 1.8 Pa for normal stress (**Figure 5.11**). Normal stresses in pulsatile flow are higher than in steady flow. At the RBC threshold value of deformation, the normal stress volume at 1.8 Pa in pulsatile flow exhibited higher

values compared to steady flow (0.55 cm^3 compared to 0.41 cm^3) while shear stress volume at 13.4 Pa the difference is similar in magnitude. For vWf deformation, the normal stress volume is larger in pulsatile flow than in steady flow (1.22 cm^3 compared to 0.95 cm^3). As for shear volume, it remains similar. Blood in HVAD experienced higher shear stress over a larger volume as compared to normal stress in pulsatile flow.

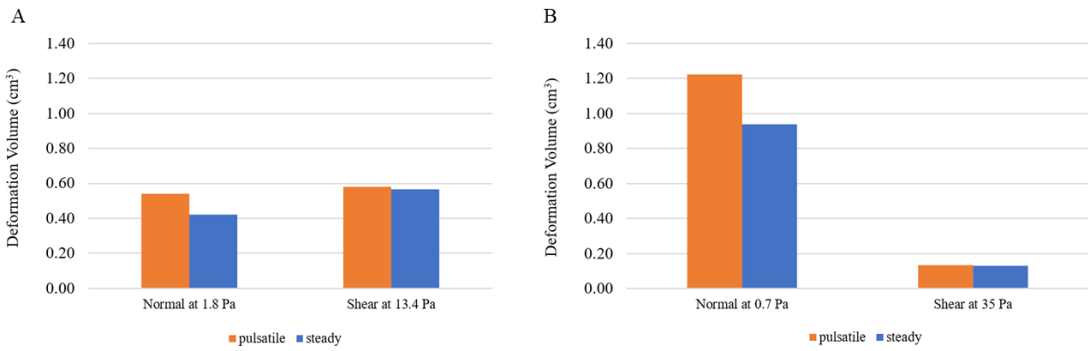

Figure 5-11: Deformation volumes in HVAD for blood damage with pulsatile and steady flow. A. Mean RBC deformation volumes and; B. vWf deformation volumes over time.

5.3 Discussion

The risk of clinically significant adverse effects of flow pulsatility has not been eradicated yet [108]. Under constant speed operation, CF-VAD not only diminishes vascular pulsatility but also causes permanent closure to the atrioventricular (AV) valves [109]. This is because the endothelium and smooth muscles of the heart can sense a change in the arterial pulse and adapt to cyclic pressure-flow changes to maintain normal homeostasis. The increase in wall stiffness changes the structural composition of the aorta in CF-VAD patients due to the absence of the AV valve opening, compared with age-matched HF patients and non-failing donors [110]. However, the clinical benefits of vascular pulsatility which has the potential to consequently cause non-physiological stress-induced blood damage have been debated for decades. In this chapter, CF-VAD was numerically analysed instead for the pulsatile flow structure and fluid stress volumes and assessed under normal working conditions (5 l/min at 2600 rpm) of the LVAD system. The CFD predicted an increase in 2 orders of magnitude of normal stress compared

with the steady flow at peak, which existed in the clearance between the top housing and rotating impeller. This could be attributed to its flow path design which encourages flow detachment and recirculation.

With the frozen rotor approach, the boundary layer of fluid move from the channels along the impeller wall and slows down because it is forced to move from an area of low pressure to an area of high pressure. When the boundary layer of fluid slows down to a certain point, it detaches from the surface of the impeller and becomes turbulent. It is low turbulence as it has a turbulence intensity of 1 %, and only if a flow is completely uniform (no velocity difference) turbulence does not occur. Pressure drag occurs when fluid flows past the impeller, it induces a large wake that completely changes the flow downstream of the point of separation. Separation occurs in flow that is slowing down in (**Figure 5.2**), with pressure increasing, after passing through the channels. Without sliding mesh, the flow field prediction is, like for the frozen rotor calculation, not realistic. Large pressure variation imposed by moving interface and flow disturbances due to pulsatility (introduces changing velocities with time) from inlet data, the greater the inertia compared to the viscosity, the higher the risk of boundary layer separation in the volute. Hence, if the flow field is realistic then the stresses will also be realistic, the decision was to use the sliding mesh approach.

Analysis of CFD data demonstrated that cell deformation volume by shear stress remains unchanged. This is logical since the devices rotate with small gaps and that creates a shearing action mostly recurring in these regions. However, normal stress is significantly affected as they normally appear alongside the wall of the impeller and between the blades and along the slope. The flow separation is caused by the pressure differential between the start and end surfaces of the flow channel into the volute. In general, blood in VAD still experiences higher shear stress over a large volume as compared to normal stress. However, in the HVAD, the pulsatile flow shear stress volumes at 10 Pa and 100 Pa were similar to a steady flow. While for normal stress, there was a difference of 2 orders of magnitude between pulsatile flow 0.2 % (0.024 cm^3), and 6.7 $\times 10^{-4}$ % (0.00008 cm^3) to steady 0.06 % (0.0083 cm^3) and 1.6 $\times 10^{-4}$ % (0.00002 cm^3). In pulsatile flow, as the pump speed increase, the normal stress volumes elevate and were above the 10 Pa threshold which was 0.024 ml (0.2 %), compared with the steady

flow at peak flow conditions. For blood damage effects, including RBC deformation and protein unravelling, the normal stress volume in pulsatile flow was 1.25 times larger compared to a steady flow, while the shear stress volume difference is similar in magnitude for both flow conditions. It has also been shown that normal stress is the primary culprit at the low-stress threshold of blood trauma.

5.3.1 Limitations

The methodology for this study is quite similar, most of the assumptions are aforementioned in section 4.5.1. The CFD approaches used in this study have additional shortages. As shown at the beginning of the chapter, the differential pressure generated from simulation differ from the human mock circulation loop experimentation done by Noor *et al* [92]. There are no experimental results or other investigations carried out in literature related to this scenario. It may be that there are physical limitations associated with the simulation setup which could have inadequately modelled the HQ data produce and caused an adverse effect on the results obtained.

The HVAD gap is set to be constant for simulation. While the geometry of the HVAD is reversed engineered by measuring a used physical pump. The inaccuracies of the model could potentially cause a small change in the impeller position which could noticeably affect the fluid stress field. This is due to the small size of gap clearances between the impeller. Especially, fast rotating impellers would experience significant unbalanced pressure distribution on the impeller surface and hydrodynamic forces. The small changes, however, might be negligible as the secondary flow path accounts for only a small amount of the total volume of blood.

The present work also is only a comparative and correlation study between pressure-velocity profiles and fluid stress volume distribution under different flow conditions. It would be wise to include the linearised power law model to calculate the haemolysis index under steady and pulsatile flow conditions. The applicability of this blood damage model for pulsatile flow conditions needs to be experimentally validated. It is premature to make conclusions based solely on CFD simulations. As for cell deformation and protein unravelling, particle-based

models will need to be considered as this depends on the change of fluid stress with time to investigate the effects of blood damage.

5.3.2 Conclusion

It was found that the quantity and regions of shear stress were not affected as much as the quantity and region of normal stresses. The shear stress occurred mostly in the gap clearance above and below the impeller which does not change with time. The increased relative pressure between the centre strut and the impeller causes various amounts of flow detachment which increase the normal stresses. Recurring regions of normal stress are at the wall of the impeller and in between the blades along the slope. This justified that the flow unsteadiness caused by rotor-stator interaction cannot be disregarded in this case and the full TRS simulation is required to calculate the normal stresses accurately. When pulsatile inlet flow is accounted for, flow disturbances increased as quantified by the size of recirculation zones and reduced the amount of streamlined flow at the outlet during the acceleration phase. Transient results were examined, and the occurrence of fluid dynamic stresses was increased at peak of systole. Nevertheless, the average flow profile suggested that the influence on overall shear and normal stresses seems seemingly insignificant. Flow variation doesn't become critical unless there is an interest in blood cell deformation at a certain time point in a cardiac cycle.

Chapter 6

Conclusion and Future Work

This chapter further highlights the conclusions drawn from the research and provides suggestions for additional work to be developed and improved upon the results obtained.

6.1 Conclusions

In summary, the study carried out in the thesis adds to existing literature focused on the prevalence of elongational stress, in comparison with shear stress, in rotary VADs with steady and pulsatile fluid flow. This research project was conducted at a time when the number of heart transplants was declining and HVAD was commercially available in the market [34]. In this context, HVAD was chosen to be investigated and explored for existential fluid stresses linked to blood trauma.

The thesis explores numerical models for blood damage which are generally based on the Scalar Shear Stress (SSS), a scalar invariant calculated from the tensor components in analogy with the von Mises stress for solids and first introduced by Bludszuweit [4]. Relationships between damage to the blood components and the SSS are then used in predictions of blood damage from the whole device. These methods make an assumption about the relative contribution from the normal and shear stress components to the scalar which leads to blood damage. In literature, a few numerical studies also assumed steady state inflow conditions, whereas the beating heart imposes a pulsatile inflow on the VAD. Therefore, the

following was done to assess the importance of pulsatile boundary conditions on the estimation of blood damage in VADs. The research conclusions are as follows:

- Simulations disclosed that shear stress volumes are predominantly larger than elongational volumes for both centrifugal and axial VADs.

- For pulsatile inlet flow, larger variations were observed in the flow profile and stress field over time, but the time-averaged values were indiscernible compared to fixed-rate (steady flow).

This study is a starting point for further experimental studies into the effects of normal stress and pulsatility. It is crucial to properly incorporate the effects of normal stress and pulsatile flow into the numerical blood damage model.

The shear stress volumes were up to two orders of magnitude larger than the normal stress volumes. However, considering thresholds for red blood cell and von Willebrand factor deformation by normal and shear stresses, the fluid volumes causing deformation by normal stress were 2.5 and 5 times the size of those causing deformation by shear stress. There is a significant volume of normal stress at low threshold stress levels and if taken into consideration alongside the shear stress measurements, has the potential to change the predicted blood damage field and hence change the way devices are designed.

Combining CFD-based computational models and experimental studies from Noor *et al* [92], the flow dynamics of the HVAD with flow data from a pulsatile mock circulation loop and its potential risk for device-induced blood trauma was investigated numerically. At a steady flow rate, the calculations showed normal stresses do occur in rotary VADs: the fluid volumes experiencing normal stress above 10 Pa were 0.0083 ml (0.069%) and were present in the HeartWare HVAD. In pulsatile flow, the normal stress volumes were higher above the 10 Pa threshold which was 0.024 ml (0.2 %). There is an increase in 2 orders of magnitude of normal stress as compared to steady flow at peak flow, which existed in the clearance between the top housing and rotating impeller.

6.2 Future Work

As for future work, a generic parameterised numerical model of the left ventricular with a LVAD attached can be constructed to compute the intraventricular haemodynamics [111]. Combining the pulsatility and blood damage model developed will allow real-time simulation of the LV with LVAD which will be able to produce physiological flow conditions of a LVAD patient. The model will apply threshold stresses for vWf deformation from the experimental deformation index curve for shear and elongational flow to predict bleeding and clotting regions. This will provide engineers and clinicians with the numerical tool needed to understand and test the efficiency of LVAD designs and predict their effect on patients.

In addition, vWf was chosen to be investigated at the low stress levels to study in detail the effects of elongational stress on blood components. Higher shear stress in LVADs exposes the cleavage sites for vWf, making it susceptible to proteolysis which destroys its binding function for clotting. In "Chapter 2", a few experiments have been done by previous researchers to investigate the effects of elongational stress on vWf. A variety of modelling techniques and experimental protocols (e.g. microfluidics) can be used to investigate deformation and damage with a multi-scale approach. The result can be used for the prediction of vWf cleavage in a general flow field and then be implemented with flow pulsatility to predict deformation and cleavage of vWf for different operating conditions in LVADs. Hence, the incorporation of pulsatile conditions through test and simulation would be an important next step, acknowledging the fact that dynamic pulsatility of the heart shall be still accounted for in the modelling of the LVAD support mechanisms.

References

[1] Dominica PY Khoo, Andrew N Cookson, Harinderjit S Gill, and Katharine H Fraser. Normal fluid stresses are prevalent in rotary ventricular assist devices: A computational fluid dynamics analysis. *The International Journal of Artificial Organs*, 41(11):738–751, 2018. doi: 10.1177/0391398818792757. URL `https://doi.org/10.1177/0391398818792757`. PMID: 30141359.

[2] Dominica Pi Ying Khoo, Harinderjit Gill, Andrew Cookson, and Katharine Fraser. Numerical comparison of shear and elongational stresses in rotary ventricular assist devices. July 2017. URL `https://esbiomech.org/conference/index.php/esb2017/seville`. 23rd Congress of the European Society of Biomechanics ; Conference date: 02-07-2017 Through 05-07-2017.

[3] Katharine Fraser and Dominica Pi Ying Khoo. Pulsatile flow in vads: Cfd analysis of velocity fields around the pressure-flow loop. September 2018.

[4] C. Bludszuweit. Three-Dimensional Numerical Prediction of Stress Loading of Blood Particles in a Centrifugal Pump. *Artificial Organs*, 19(7):590–596, jul 1995. doi: 10.1111/j.1525-1594.1995.tb02386.x. URL `http://doi.wiley.com/10.1111/j.1525-1594.1995.tb02386.x`.

[5] R. F. Saidi and S.K. Hejazii Kenari. Challenges of organ shortage for transplantation: solutions and opportunities. *Int J Organ Transplant Med*, 5:87–96, august 2014. doi: 10.1136/BMJ.D2483. URL `https://www.ncbi.nlm.nih.gov/pmc/articles/PMC4149736/`.

[6] J. Cleland, S. Hardman, and P. Mitchell. National Heart Failure

Audit. *National Institute for Cardiovascular Outcomes Research (NICOR)*, 2013. URL https://www.ucl.ac.uk/nicor/audits/heartfailure/documents/annualreports/hfannual12-13.pdf.

[7] Zengsheng Chen, Anqiang Sun, Hongyu Wang, Yubo Fan, and Xiaoyan Deng. Non-physiological shear stress-induced blood damage in ventricular assist device. *Medicine in Novel Technology and Devices*, 3:100024, 2019. ISSN 2590-0935. doi: https://doi.org/10.1016/j.medntd.2019.100024. URL https://www.sciencedirect.com/science/article/pii/S2590093519300244.

[8] Peter M Eckman and Ranjit John. Bleeding and thrombosis in patients with continuous-flow ventricular assist devices. *Circulation*, 125(24):3038–3047, 2012.

[9] Brit Long, Jennifer Robertson, Alex Koyfman, and William Brady. Left ventricular assist devices and their complications: a review for emergency clinicians. *The American Journal of Emergency Medicine*, 37(8):1562–1570, 2019.

[10] L. E. Copstead-Kirkhorn and J. L. Banasik. *"Heart Failure and Dysrhythmias: Common Sequelae of Cardiac Diseases" in Pathophysiology*. Elsevier Saunders, St. Louis, Missouri, 5 edition, 2013. ISBN 9780323293174.

[11] A. C. Guyton and J. E. Hall. *"Heart Muscle: The Heart as a Pump and Function of the Heart Valves" in Textbook of Medical Physiology*. Elsevier Saunders, Philadelphia, 11 edition, 2006. URL http://jpkc.hactcm.edu.cn/2012yxslx/file/TextbookofMedicalPhysiology.pdf.

[12] G. Hennersdorf. Congestive Heart Failure Pathophysiology. https://www.slideshare.net/Hennersd/heart-failure2013-path-bw, 2013. visited on 2017-09-20.

[13] E. Braunwald. Heart Failure. *JACC: Heart Failure*, 1(1):1–20, feb 2013. doi: 10.1016/j.jchf.2012.10.002. URL http://linkinghub.elsevier.com/retrieve/pii/S2213177912000078.

[14] A. Montalto, A. Loforte, F. Musumeci, T. Krabatsch, and M. S. Slaughter. *Mechanical Circulatory Support in End-Stage Heart Failure*. Springer Inter-

national Publishing, Cham, Switzerland, 1 edition, 2017. ISBN 978-3-319-43381-3. doi: 10.1007/978-3-319-43383-7. URL http://link.springer.com/10.1007/978-3-319-43383-7.

[15] Gianluigi Savarese and Lars H Lund. Global public health burden of heart failure. *Cardiac failure review*, 3(1):7, 2017.

[16] British Heart Foundation. BHF CVD Statistics Factsheet - UK. *BHF Factsheet*, (March):5, 2016. doi: 10.1017/CBO9781107415324.004. URL https://www.bhf.org.uk/research/heart-statistics.

[17] G. A. Macgowan, G. Parry, S. Schueler, and A. Hasan. The decline in heart transplantation in the UK. *BMJ (Clinical research ed.)*, 342:d2483, may 2011. doi: 10.1136/BMJ.D2483. URL http://www.ncbi.nlm.nih.gov/pubmed/21546420.

[18] NHS England. Annual Report on Cardiothoracic Transplantation. Technical report, NHS England, England, United Kingdom, 2016. URL https://nhsbtdbe.blob.core.windows.net/umbraco-assets-corp/1311/organ{_}specific{_}report{_}cardiothoracic{_}2016.pdf.

[19] Conor Stewart. Heart transplants in the united kingdom (uk) 2020/21, 2021. URL https://www.statista.com/statistics/518763/number-of-heart-transplants-united-kingdom-uk/.

[20] Edward L Hannan. Randomized clinical trials and observational studies: guidelines for assessing respective strengths and limitations. *JACC: Cardiovascular Interventions*, 1(3):211–217, 2008.

[21] James C Fang. Rise of the machines–left ventricular assist devices as permanent therapy for advanced heart failure. *N Engl J Med*, 361(23):2282–5, 2009.

[22] Colleen K McIlvennan, Kate H Magid, Amrut V Ambardekar, Jocelyn S Thompson, Daniel D Matlock, and Larry A Allen. Clinical outcomes after continuous-flow left ventricular assist device: a systematic review. *Circulation: Heart Failure*, 7(6):1003–1013, 2014.

[23] National Institutes of Health. The adrian kantrowitz papers, replacing

hearts: Left ventricle assist devices and transplants, 1960-1970: Documents, 2011. URL https://profiles.nlm.nih.gov/spotlight/gn/feature/replacing.

[24] Michael E DeBakey. Left ventricular bypass pump for cardiac assistance: clinical experience. *The American journal of cardiology*, 27(1):3–11, 1971.

[25] JC Norman, DA Cooley, BD Kahan, AS Keats, EK Massin, RT Solis, WE Luper, MI Brook, T Klima, OH Frazier, et al. Total support of the circulation of a patient with post-cardiotomy stone-heart syndrome by a partial artificial heart (alvad) for 5 days followed by heart and kidney transplantation. *The Lancet*, 311(8074):1125–1127, 1978.

[26] S. Westaby and M. Deng. Continuous flow blood pumps: the new gold standard for advanced heart failure? *European Journal of Cardio-Thoracic Surgery*, 44(1):4–8, jul 2013. ISSN 1010-7940. doi: 10.1093/ejcts/ezt248. URL https://academic.oup.com/ejcts/article-lookup/doi/10.1093/ejcts/ezt248.

[27] Jooli Han and Dennis R Trumble. Cardiac assist devices: Early concepts, current technologies, and future innovations. *Bioengineering (Basel, Switzerland)*, 6(1):E18, February 2019. ISSN 2306-5354. doi: 10.3390/bioengineering6010018. URL https://europepmc.org/articles/PMC6466092.

[28] S. A. Mokashi, J. D. Schmitto, L. S. Lee, J. D. Rawn, R. M. Bolman III, P. S. Shekar, G. S. Couper, and F. Y. Chen. Ventricular Assist Device in Patients With Prosthetic Heart Valves. *Artificial Organs*, 34(11):1030–1034, nov 2010. doi: 10.1111/j.1525-1594.2010.01102.x. URL http://doi.wiley.com/10.1111/j.1525-1594.2010.01102.x.

[29] A. Prinzing, U. Herold, A. Berkefeld, M. Krane, R. Lange, and B. Voss. Left ventricular assist devices—current state and perspectives. *Journal of Thoracic Disease*, 8(8):E660–E666, aug 2016. doi: 10.21037/jtd.2016.07.13. URL http://jtd.amegroups.com/article/view/8418/7900.

[30] J. Bumrungpetch. *Mechanism Design of Ventricular Assist Device*. PhD thesis, Queensland University of Technology, 2016. URL https://

eprints.qut.edu.au/94239/1/Jeerasit{_}Bumrungpetch{_}Thesis.pdf.

[31] N. Moazami, K. Fukamachi, M. Kobayashi, N. G. Smedira, K. J. Hoercher, A. Massiello, S. Lee, D. J. Horvath, and R. C. Starling. Axial and centrifugal continuous-flow rotary pumps: a translation from pump mechanics to clinical practice. *The Journal of heart and lung transplantation : the official publication of the International Society for Heart Transplantation*, 32(1):1–11, jan 2013. doi: 10.1016/j.healun.2012.10.001. URL http://www.ncbi.nlm.nih.gov/pubmed/23260699.

[32] S. B. Russell. HeartMate II ® Left Ventricular Assist Device (LVAD) Fact Sheet. Technical report, Thoratec Corporation, 2012. URL https://www.thoratec.com/downloads/heartmate-II-fact-sheet-b100-0812-final.pdf.

[33] Joe Carlson. Medtronic to pay $54.5m under proposed settlement in class-action investor lawsuit, 2018. URL https://apnews.com/article/e2490f7270914c91b24136ee8985c29f.

[34] U.S. Food and Drug Administration. Medtronic heartware ventricular assist device (hvad) system, 2022. URL https://www.fda.gov/medical-devices/cardiovascular-devices/medtronic-heartware-ventricular-assist-device-hvad-system.

[35] Andrea Park. As medtronic discontinues faulty heartware device, abbott offers up its own heart pump to meet demand, 2021. URL https://www.fiercebiotech.com/medtech/as-medtronic-discontinues-faulty-heartware-device-abbott-offers-up-its-own-heart-pump-to.

[36] Medical Network Device. Heartmate iii heart pump, 2020. URL https://www.medicaldevice-network.com/projects/heartmate-iii-heart-pump/.

[37] J. K. Kirklin, D. C. Naftel, F. D. Pagani, R. L. Kormos, L. W. Stevenson, E. D. Blume, S. L. Myers, M. A. Miller, J. T. Baldwin, and J. B. Young. Seventh INTERMACS annual report: 15,000 patients and count-

ing. *Journal of Heart and Lung Transplantation*, 34(12):1495–1504, dec 2015. doi: 10.1016/j.healun.2015.10.003. URL http://www.ncbi.nlm.nih.gov/pubmed/26520247.

[38] I. Netuka, P. Sood, Y. Pya, D. Zimpfer, T. Krabatsch, J. Garbade, V. Rao, M. Morshuis, S. Marasco, F. Beyersdorf, L. Damme, and J. D. Schmitto. Fully Magnetically Levitated Left Ventricular Assist System for Treating Advanced HF. *Journal of the American College of Cardiology*, 66(23):2579–2589, dec 2015. doi: 10.1016/j.jacc.2015.09.083. URL http://linkinghub.elsevier.com/retrieve/pii/S0735109715068394.

[39] Aditi Singhvi and Barry Trachtenberg. Left ventricular assist devices 101: Shared care for general cardiologists and primary care. *Journal of Clinical Medicine*, 8(10), 2019. ISSN 2077-0383. doi: 10.3390/jcm8101720. URL https://www.mdpi.com/2077-0383/8/10/1720.

[40] A. Ally. Whole Blood Basics: How to maintain a stable sample. http://blog.fisherbioservices.com/whole-blood-basics-how-to-maintain-a-stable-sample, 2015. visited on 2017-09-21.

[41] EW Errill. Rheology of blood. *Physiological reviews*, 49(4):863–888, 1969.

[42] John E Hall and Michael E Hall. *Guyton and Hall textbook of medical physiology e-Book*. Elsevier Health Sciences, 2020.

[43] R. Fahraeus. The Suspension-stability of the Blood. *Acta Medica Scandinavica*, 55(1):3–7, apr 2009. doi: 10.1111/j.0954-6820.1921.tb15200.x. URL http://doi.wiley.com/10.1111/j.0954-6820.1921.tb15200.x.

[44] J. Dupire, M. Socol, and A. Viallat. Full dynamics of a red blood cell in shear flow. *Proceedings of the National Academy of Sciences*, 109(51): 20808–20813, 2012. doi: 10.1073/pnas.1210236109. URL http://www.pnas.org/content/109/51/20808.full.pdf.

[45] S. P. Sutera and M. H. Mehrjardi. Deformation and fragmentation of human red blood cells in turbulent shear flow. *Biophysical Journal*, 15(1):1–10, 1975. doi: 10.1016/S0006-3495(75)85787-0. URL http://www.cell.com/biophysj/pdf/S0006-3495(75)85787-0.pdf.

[46] L. J. Wurzinger, R. Opitz, and H. Eckstein. Mechanical blood trauma: an overview. *Angeiologie*, 38(3):81–97, 1986. URL https://www.scopus.com/record/display.uri?eid=2-s2.0-0022443425{&}origin=inward{&}txGid=60adc1b288351292b779a1c2c04a95d6.

[47] M. Giersiepen, L. J. Wurzinger, R. Opitz, and H. Reul. Estimation of shear stress-related blood damage in heart valve prostheses - in vitro comparison of 25 aortic valves. *International Journal of Artificial Organs*, 13(5):300–306, 1990. URL https://www.scopus.com/record/display.uri?eid=2-s2.0-0025082325{&}origin=inward{&}txGid=6c0f018c28771ca19a183632788899da.

[48] G. Heuser and R. Opitz. A couette viscometer for short time shearing of blood. *Biorheology*, 17(1-2):17–24, 1980. URL https://www.scopus.com/record/display.uri?eid=2-s2.0-0019186014{&}origin=inward{&}txGid=d58531dacc09be8ec6a143e7bada2708.

[49] R. Paul, J. Apel, S. Klaus, F. Schugner, P. Schwindke, and H. Reul. Shear Stress Related Blood Damage in Laminar Couette Flow. *Artificial Organs*, 27(6):517–529, jun 2003. doi: 10.1046/j.1525-1594.2003.07103.x. URL http://doi.wiley.com/10.1046/j.1525-1594.2003.07103.x.

[50] B. Thamsen. *A Two-Stage Rotary Blood Pump Design to Reduce Blood Trauma*. PhD thesis, Charité – Universitätsmedizin Berlin, 2016.

[51] P. Hochareon, K. B. Manning, A. A. Fontaine, J. M. Tarbell, and S. Deutsch. Correlation of In Vivo Clot Deposition With the Flow Characteristics in the 50 cc Penn State Artificial Heart: A Preliminary Study. *ASAIO Journal*, 50(6):537–542, 2004. doi: 10.1097/01.MAT.0000145694.40637.A0. URL http://citeseerx.ist.psu.edu/viewdoc/download?doi=10.1.1.659.4325{&}rep=rep1{&}type=pdf.

[52] S. M. Becker and A. V. Kuznetsov. *"Mechanical Stress Induced Blood Trauma" in Heat Transfer and Fluid Flow in Biological Processes*. Academic Press, 1 edition, 2015. ISBN 9780124079007.

[53] J. D. Hellums. 1993 Whitaker lecture: Biorheology in thrombosis research.

Annals of Biomedical Engineering, 22(5):445–455, sep 1994. doi: 10.1007/BF02367081. URL http://link.springer.com/10.1007/BF02367081.

[54] I. Bakir, M. F. Hoylaerts, T. Kink, L. Foubert, P. Luyten, S. Van Kerckhoven, V. Leunens, H. Bollen, H. Reul, and B. Meyns. Mechanical Stress Activates Platelets at a Subhemolysis Level: An In Vitro Study. *Artificial Organs*, 31(4):316–323, apr 2007. doi: 10.1111/j.1525-1594.2007.00381.x. URL http://doi.wiley.com/10.1111/j.1525-1594.2007.00381.x.

[55] V. Leytin, D. J. Allen, S. Mykhaylov, L. Mis, E. V. Lyubimov, B. Garvey, and J. Freedman. Pathologic high shear stress induces apoptosis events in human platelets. *Biochemical and Biophysical Research Communications*, 320(2):303–310, jul 2004. doi: 10.1016/j.bbrc.2004.05.166. URL http://linkinghub.elsevier.com/retrieve/pii/S0006291X04011763.

[56] H. M. Tsai, I. I. Sussman, and R. L. Nagel. Shear stress enhances the proteolysis of von Willebrand factor in normal plasma. *Blood*, 83(8):2171–2179, 1994. URL http://www.bloodjournal.org/content/83/8/2171.long?sso-checked=true.

[57] A. Vincentelli, S. Susen, T. Le Tourneau, I. Six, O. Fabre, F. Juthier, A. Bauters, C. Decoene, J. Goudemand, A. Prat, and B. Jude. Acquired von Willebrand Syndrome in Aortic Stenosis. *New England Journal of Medicine*, 349(4):343–349, jul 2003. doi: 10.1056/NEJMoa022831. URL http://www.nejm.org/doi/abs/10.1056/NEJMoa022831.

[58] N. Uriel, S. W. Pak, U. P. Jorde, B. Jude, S. Susen, A. Vincentelli, P. V. Ennezat, S. Cappleman, Y. Naka, and D. Mancini. Acquired von Willebrand Syndrome After Continuous-Flow Mechanical Device Support Contributes to a High Prevalence of Bleeding During Long-Term Support and at the Time of Transplantation. *Journal of the American College of Cardiology*, 56(15):1207–1213, oct 2010. doi: 10.1016/j.jacc.2010.05.016. URL http://www.ncbi.nlm.nih.gov/pubmed/20598466http://www.ncbi.nlm.nih.gov/pubmed/20598466.

[59] C. A. Siediecki, B. J. Lestini, K. K. Kottke-Marchant, S. J. Eppell, D. L. Wilson, and R. E. Marchant. Shear-dependent changes in the three-dimensional structure of human von Willebrand factor. *Blood*, 88(8):2939–

2950, 1996. URL http://www.bloodjournal.org/content/88/8/2939?sso-checked=true.

[60] E. Di Stasio and R. De Cristofaro. The effect of shear stress on protein conformation: Physical forces operating on biochemical systems: The case of von Willebrand factor. *Biophysical Chemistry*, 153(1):1–8, dec 2010. doi: 10.1016/J.BPC.2010.07.002. URL http://www.sciencedirect.com/science/article/pii/S0301462210001900?via{%}3Dihub.

[61] S. W. Day, J. C. McDaniel, H. G. Wood, P. E. Allaire, N. Landrot, and A. Curtas. Particle image velocimetry measurements of blood velocity in a continuous flow ventricular assist device. *ASAIO Journal*, 47(4):406–411, 2001. URL http://www.embase.com/search/results?subaction=viewrecord{&}from=export{&}id=L32655816{%}5Cnhttp://sfx.library.uu.nl/utrecht?sid=EMBASE{&}issn=10582916{&}id=doi:{&}atitle=Particle+image+velocimetry+measurements+of+blood+velocity+in+a+continuous+flow+ventricular+assis.

[62] L. P. Chua, K. S. Ong, C. M. S. Yu, and T. M. Zhou. Leakage flow rate and wall shear stress distributions in a biocentrifugal ventricular assist device. *ASAIO journal (American Society for Artificial Internal Organs : 1992)*, 50(6):530–536, 2004. doi: 10.1097/01.MAT.0000144363.92963.CB.

[63] Z. J. Wu, R. K. Gottlieb, G. W. Burgreen, J. A. Holmes, D. C. Borzelleca, M. V. Kameneva, B. P. Griffith, and J. F. Antaki. Investigation of fluid dynamics within a miniature mixed flow blood pump. *Experiments in Fluids*, 31(6):615–629, 2001.

[64] C. Y. Schüle, B. Thamsen, B. Blümel, M. Lommel, T. Karakaya, C. O. Paschereit, K. Affeld, and U. Kertzscher. Experimental and Numerical Investigation of an Axial Rotary Blood Pump. *Artificial Organs*, 40(11): E192–E202, nov 2016. doi: 10.1111/aor.12725. URL http://doi.wiley.com/10.1111/aor.12725.

[65] E. Bock, A. Ribeiro, M. Silva, P. Antunes, J. Fonseca, D. Legendre, J. Leme, C. Arruda, J. Biscegli, D. Nicolosi, and A. Andrade. New centrifugal blood pump with dual impeller and double pivot bearing system: Wear evaluation

in bearing system, performance tests, and preliminary hemolysis tests. *Artificial Organs*, 32(4):329–333, 2008. doi: 10.1111/j.1525-1594.2008.00550.x.

[66] D. J. Restle, D. M. Zhang, G. Hung, J. L. Howard, F. Kallel, M. A. Acker, P. Atluri, and C. R. Bartoli. Preclinical Models for Translational Investigations of Left Ventricular Assist Device-Associated von Willebrand Factor Degradation. *Artificial Organs*, 39(7):569–575, jul 2015. doi: 10.1111/aor.12428. URL `http://doi.wiley.com/10.1111/aor.12428`.

[67] T. Zhang, M. E. Taskin, H. B. Fang, A. Pampori, R. Jarvik, B. P. Griffith, and Z. J. Wu. Study of Flow-Induced Hemolysis Using Novel Couette-Type Blood-Shearing Devices. *Artificial Organs*, 35(12):1180–1186, dec 2011. doi: 10.1111/j.1525-1594.2011.01243.x. URL `http://doi.wiley.com/10.1111/j.1525-1594.2011.01243.x`.

[68] S. S. Lee, Y. J. Yim, K. H. Ahn, and S. J. Lee. Extensional flow-based assessment of red blood cell deformability using hyperbolic converging microchannel. *Biomedical Microdevices*, 11(5):1021–1027, oct 2009. doi: 10.1007/s10544-009-9319-3. URL `http://link.springer.com/10.1007/s10544-009-9319-3`.

[69] L. A. Down, D. V. Papavassiliou, and E. A. O'Rear. Significance of Extensional Stresses to Red Blood Cell Lysis in a Shearing Flow. *Annals of Biomedical Engineering*, 39(6):1632–1642, jun 2011. doi: 10.1007/s10439-011-0262-0. URL `http://link.springer.com/10.1007/s10439-011-0262-0`.

[70] A. Garon and M. I. Farinas. Fast Three-dimensional Numerical Hemolysis Approximation. *Artificial Organs*, 28(11):1016–1025, nov 2004. doi: 10.1111/j.1525-1594.2004.00026.x. URL `http://doi.wiley.com/10.1111/j.1525-1594.2004.00026.x`.

[71] A. Arvand, M. Hormes, and H. Reul. A Validated Computational Fluid Dynamics Model to Estimate Hemolysis in a Rotary Blood Pump. *Artificial Organs*, 29(7):531–540, jul 2005. doi: 10.1111/j.1525-1594.2005.29089.x. URL `http://doi.wiley.com/10.1111/j.1525-1594.2005.29089.x`.

[72] Zengsheng Chen, Sofen K Jena, Guruprasad A Giridharan, Michael A Sobieski, Steven C Koenig, Mark S Slaughter, Bartley P Griffith, and

Zhongjun J Wu. Shear stress and blood trauma under constant and pulse-modulated speed cf-vad operations: Cfd analysis of the hvad. *Medical & biological engineering & computing*, 57(4):807–818, 2019.

[73] P. L. Maffettone and M. Minale. Equation of change for ellipsoidal drops in viscous flow. *Journal of Non-Newtonian Fluid Mechanics*, 78(2-3):227–241, aug 1998. doi: 10.1016/S0377-0257(98)00065-2. URL `http://www.sciencedirect.com/science/article/pii/S0377025798000652?via{%}3Dihub`.

[74] L. Pauli, J. Nam, M. Pasquali, and M. Behr. Transient stress-based and strain-based hemolysis estimation in a simplified blood pump. *International Journal for Numerical Methods in Biomedical Engineering*, 29(10):1148–1160, oct 2013. doi: 10.1002/cnm.2576. URL `http://doi.wiley.com/10.1002/cnm.2576`.

[75] A. Alexander-Katz and R. R. Netz. Dynamics and Instabilities of Collapsed Polymers in Shear Flow. *Macromolecules*, 41(9):3363–3374, may 2008. doi: 10.1021/ma702331d. URL `http://pubs.acs.org/doi/abs/10.1021/ma702331d`.

[76] B. Huisman, M. Hoore, G. Gompper, and D. A. Fedosov. Modeling the cleavage of von Willebrand factor by ADAMTS13 protease in shear flow. *Medical Engineering & Physics*, 48:14–22, jul 2017. doi: 10.1016/j.medengphy.2017.06.044. URL `http://linkinghub.elsevier.com/retrieve/pii/S1350453317301947`.

[77] C. E. Sing and A. Alexander-Katz. Elongational Flow Induces the Unfolding of von Willebrand Factor at Physiological Flow Rates. *Biophysical Journal*, 98:35–37, 2010. doi: 10.1016/j.bpj.2010.01.032. URL `https://www.ncbi.nlm.nih.gov/pmc/articles/PMC2862189/pdf/main.pdf`.

[78] T. A. Springer. Von Willebrand factor, Jedi knight of the bloodstream. *Blood*, 124(9):1412–1425, aug 2014. ISSN 15280020. doi: 10.1182/blood-2014-05-378638. URL `http://www.ncbi.nlm.nih.gov/pubmed/24928861http://www.pubmedcentral.nih.gov/articlerender.fcgi?artid=PMC4148764`.

[79] Hongxia Fu, Yan Jiang, Darren Yang, Friedrich Scheiflinger, Wesley P. Wong, and Timothy A. Springer. Flow-induced elongation of von willebrand factor precedes tension-dependent activation. *Nature Communications*, 8 (1):324, 2017. ISSN 2041-1723. doi: 10.1038/s41467-017-00230-2. URL `https://doi.org/10.1038/s41467-017-00230-2`.

[80] Tyler Schmidt, David Rosenthal, Olaf Reinhartz, Kirk Riemer, Fei He, Tain-Yen Hsia, Alison Marsden, and Ethan Kung. Superior performance of continuous over pulsatile flow ventricular assist devices in the single ventricle circulation: A computational study. *Journal of Biomechanics*, 52:48–54, 2017. ISSN 0021-9290. doi: https://doi.org/10.1016/j.jbiomech.2016.12.003. URL `https://www.sciencedirect.com/science/article/pii/S0021929016312660`.

[81] J. V. C. Batista. Obtaining a HVAD CAD Geometry for CFD Analysis Using a DS10 Contact Scanner. Technical Report August, University of Bath, Bath, Great Britain, 2016.

[82] R. A. Malinauskas, P. Hariharan, S. W. Day, L. H. Herbertson, M. Buesen, U. Steinseifer, K. I. Aycock, B. C. Good, S. Deutsch, K. B. Manning, and B. A. Craven. FDA Benchmark Medical Device Flow Models for CFD Validation. *ASAIO Journal*, 63(2):150–160, 2017. doi: 10.1097/MAT.0000000000000499. URL `http://insights.ovid.com/crossref?an=00002480-201703000-00009`.

[83] Molteni Alessandra, P. H. Masri Zubair, W. Q. Low Kenny, N. Yousef Haitham, Sienz Johann, and H. Fraser Katharine. Experimental measurement and numerical modelling of dye washout for investigation of blood residence time in ventricular assist devices. *The International Journal of Artificial Organs*, page 0391398817752877, 2018. ISSN 0391-3988. doi: 10.1177/0391398817752877. URL `https://doi.org/10.1177/0391398817752877`.

[84] G. M. Wieselthaler, G. ODriscoll, P. Jansz, A. Khaghani, and M. Strueber. Initial clinical experience with a novel left ventricular assist device with a magnetically levitated rotor in a multi-institutional trial. *The Journal of Heart and Lung Transplantation*, 29(11):1218–1225, nov 2010.

ISSN 1053-2498. doi: 10.1016/J.HEALUN.2010.05.016. URL https://www.sciencedirect.com/science/article/pii/S1053249810003116.

[85] B. Thamsen, M. Plamondon, M. Granegger, M. Schmid Daners, R. Kaufmann, A. Neels, and M. Meboldt. Investigation of the Axial Gap Clearance in a Hydrodynamic-Passive Magnetically Levitated Rotary Blood Pump Using X-Ray Radiography. *Artificial Organs*, 00(3):0–5, 2018. ISSN 0160564X. doi: 10.1111/aor.13074. URL http://doi.wiley.com/10.1111/aor.13074.

[86] K. Shekar, S. D. Gregory, and J. F. Fraser. Mechanical circulatory support in the new era: An overview. *Critical Care*, 20(1), 2016. ISSN 1466609X. doi: 10.1186/s13054-016-1235-3. URL http://dx.doi.org/10.1186/s13054-016-1235-3.

[87] B. P. Griffith, R. L. Kormos, H. S. Borovetz, K. Litwak, J. F. Antaki, V. L. Poirier, and K. C. Butler. HeartMate II left ventricular assist system: from concept to first clinical use. *The Annals of Thoracic Surgery*, 71(3): S116–S120, 2001. ISSN 00034975. doi: 10.1016/S0003-4975(00)02639-4.

[88] K. H. Fraser, T. Zhang, M. E. Taskin, B. P. Griffith, and Z. J. Wu. A Quantitative Comparison of Mechanical Blood Damage Parameters in Rotary Ventricular Assist Devices: Shear Stress, Exposure Time and Hemolysis Index. *Journal of Biomechanical Engineering*, 134(8):081002, 2012. doi: 10.1115/1.4007092. URL http://biomechanical.asmedigitalcollection.asme.org/article.aspx?articleid=1476077.

[89] F. R. Menter. Two-equation eddy-viscosity turbulence models for engineering applications. *AIAA Journal*, 32(8):1598–1605, aug 1994. doi: 10.2514/3.12149. URL http://arc.aiaa.org/doi/10.2514/3.12149.

[90] F. R. Menter, M. Kuntz, and R. Langtry. Ten Years of Industrial Experience with the SST Turbulence Model. *Turbulence, Heat and Mass Transfer 4*, 2003. URL http://citeseerx.ist.psu.edu/viewdoc/download?doi=10.1.1.460.2814{&}rep=rep1{&}type=pdf.

[91] ANSYS Incorporation. Modeling Flows in Moving Zones. *FLUENT 6.0 User's Guide*, 1(1):1–68, 2001. URL https://www.researchgate.

net/file.PostFileLoader.html?id=5833091096b7e41f806975ae&assetKey=AS%3A430873536405505%401479739664413.

[92] M. R. Noor, C. H. Ho, K. H. Parker, A. R. Simon, N. R. Banner, and C. T. Bowles. Investigation of the Characteristics of HeartWare HVAD and Thoratec HeartMate II Under Steady and Pulsatile Flow Conditions. *Artificial Organs*, 40(6):549–560, 2016. doi: 10.1111/aor.12593.

[93] Wikipedia. Cauchy stress tensor: Transformation rule of the stress tensor. https://commons.wikimedia.org/wiki/User:Sanpaz, 2009. visited on 2017-09-25.

[94] K. H. Fraser, M. E. Taskin, B. P. Griffith, and Z. J. Wu. The use of computational fluid dynamics in the development of ventricular assist devices. *Medical Engineering & Physics*, 33(3):263–280, apr 2011. doi: 10.1016/j.medengphy.2010.10.014. URL http://www.ncbi.nlm.nih.gov/pubmed/21075669http://www.ncbi.nlm.nih.gov/pubmed/21075669http://www.ncbi.nlm.nih.gov/pubmed/21075669.

[95] T. Yaginuma, M. S. N. Oliveira, R. Lima, T. Ishikawa, and T. Yamaguchi. Human Red Blood Cell Behavior under Homogeneous Extensional Flow in a Hyperbolic-Shaped Microchannel. *Biomicrofluidics*, 7(5):054110, 2013. ISSN 1932-1058. doi: 10.1063/1.4820414. URL http://dx.doi.org/10.1063/1.4820414.

[96] R Zhao, J. F. Antaki, T. Naik, T. N. Bachman, M. V. Kameneva, and Z. J. Wu. Microscopic investigation of erythrocyte deformation dynamics. *Biorheology*, 43(6):747–765, 2006. ISSN 0006-355X. URL http://www.ncbi.nlm.nih.gov/entrez/query.fcgi?cmd=Retrieve{&}db=PubMed{&}dopt=Citation{&}list{_}uids=17148857.

[97] T. Jikuya, T. Tsutsui, O. Shigeta, Y. Sankai, and T. Mitsui. Species differences in erythrocyte mechanical fragility: comparison of human, bovine, and ovine cells. *ASAIO journal (American Society for Artificial Internal Organs : 1992)*, 44(5):M452–5, 1998. ISSN 1058-2916. URL http://www.ncbi.nlm.nih.gov/pubmed/9804471.

[98] J. H. Yen, S. F Chen, M. K. Chern, and P. C. Lu. the Effects of Extensional

Stress on Red Blood Cell Hemolysis. *Biomedical Engineering: Applications, Basis and Communications*, 27(05):1550042, 2015. ISSN 1016-2372. doi: 10.4015/S1016237215500428. URL http://www.worldscientific.com/doi/abs/10.4015/S1016237215500428.

[99] K. H. Fraser. Mechanical Stress Induced Blood Trauma. In *Heat Transfer and Fluid Flow in Biological Processes*, chapter 11, pages 305–333. Elsevier, London, 2015. ISBN 9780124080775. doi: 10.1016/B978-0-12-408077-5.00014-6. URL http://linkinghub.elsevier.com/retrieve/pii/B9780124080775000146.

[100] B. Thamsen, B. Blümel, J. Schaller, C. O. Paschereit, K. Affeld, L. Goubergrits, and U. Kertzscher. Numerical Analysis of Blood Damage Potential of the HeartMate II and HeartWare HVAD Rotary Blood Pumps. *Artificial Organs*, 39(8):651–659, 2015. doi: 10.1111/aor.12542.

[101] D. Arora, M. Behr, and M. Pasquali. Hemolysis estimation in a centrifugal blood pump using a tensor-based measure. *Artificial Organs*, 30(7):539–547, 2006. ISSN 0160564X. doi: 10.1111/j.1525-1594.2006.00256.x.

[102] M. Ertan Taskin, Katharine H. Fraser, Tao Zhang, Changfu Wu, Bartley P. Griffith, and Zhongjun J. Wu. Evaluation of eulerian and lagrangian models for hemolysis estimation. *ASAIO Journal*, 58(4):363–372, 2012. ISSN 1058-2916. doi: 10.1097/MAT.0b013e318254833b. URL https://journals.lww.com/asaiojournal/Fulltext/2012/07000/Evaluation_of_Eulerian_and_Lagrangian_Models_for.11.aspx.

[103] Wei-Che Chiu, Gaurav Girdhar, Michalis Xenos, Yared Alemu, Jõao S. Soares, Shmuel Einav, Marvin Slepian, and Danny Bluestein. Thromboresistance comparison of the heartmate ii ventricular assist device with the device thrombogenicity emulation-optimized heartassist 5 vad. *Journal of Biomechanical Engineering*, 136(2):021014–021014–9, 2014. ISSN 0148-0731. doi: 10.1115/1.4026254. URL http://dx.doi.org/10.1115/1.4026254.

[104] Laura J. Leslie, Lindsay J. Marshall, Andrew Devitt, Andrew Hilton, and Geoff D. Tansley. Cell exclusion in couette flow: Evaluation through flow visualization and mechanical forces. *Artificial Or-*

gans, 37(3):267–275, 2013. doi: doi:10.1111/j.1525-1594.2012.01561.x. URL https://onlinelibrary.wiley.com/doi/abs/10.1111/j.1525-1594.2012.01561.x.

[105] Erik Dick, Jan Vierendeels, Sven Serbruyns, and John Vande Voorde. Performance prediction of centrifugal pumps with cfd-tools. *Task quarterly*, 5 (4):579–594, 2001.

[106] Yew Chuan Chong, Dave A Staton, Markus A Mueller, and John Chick. An experimental study of rotational pressure loss in rotor-stator gap. *Propulsion and Power Research*, 6(2):147–156, 2017.

[107] Chaoshou Yan, Jianfei Liu, Shuihua Zheng, Bin Huang, and Jiacheng Dai. Study on the effects of the wear-rings clearance on the solid-liquid two-phase flow characteristics of centrifugal pumps. *Symmetry*, 12(12):2003, 2020.

[108] Tal Hasin, Salil Deo, Joseph J Maleszewski, Yan Topilsky, Brooks S Edwards, Naveen L Pereira, John M Stulak, Lyle Joyce, Richard Daly, Sudhir S Kushwaha, et al. The role of medical management for acute intravascular hemolysis in patients supported on axial flow lvad. *ASAIO Journal*, 60(1):9–14, 2014.

[109] Robert M Adamson, Walter P Dembitsky, Sam Baradarian, Joseph Chammas, Karen May-Newman, Suzanne Chillcott, Marcia Stahovich, Vicki McCalmont, Kristi Ortiz, Peter Hoagland, et al. Aortic valve closure associated with heartmate left ventricular device support: technical considerations and long-term results. *The Journal of heart and lung transplantation*, 30 (5):576–582, 2011.

[110] Amrut V Ambardekar, Kendall S Hunter, Ashok N Babu, Rubin M Tuder, R Blair Dodson, and JoAnn Lindenfeld. Changes in aortic wall structure, composition, and stiffness with continuous-flow left ventricular assist devices: a pilot study. *Circulation: Heart Failure*, 8(5):944–952, 2015.

[111] K. May-Newman, V. Vu, and B. Herold. Modeling the Link between Left Ventricular Flow and Thromboembolic Risk Using Lagrangian Coherent

Structures. *Fluids*, 1(4):38, nov 2016. doi: 10.3390/fluids1040038. URL http://www.mdpi.com/2311-5521/1/4/38.

Appendix A

Fluid Dynamic Stresses Derivations

A.1 Stress Tensor Coordinate Transformation

By expanding the matrix operation, the new $\sigma_{ij}^{'}$ components were derived and simplified using symmetry of stress tensor to give

$$\begin{aligned}\sigma_{11}^{'} = a_{11}\left(a_{11}\sigma_{11} + a_{21}\sigma_{12} + a_{31}\sigma_{13}\right) + a_{21}\left(a_{11}\sigma_{12} + a_{21}\sigma_{22} + a_{31}\sigma_{23}\right) \\ + a_{31}\left(a_{11}\sigma_{13} + a_{21}\sigma_{23} + a_{31}\sigma_{33}\right)\end{aligned} \tag{A.1}$$

$$\begin{aligned}\sigma_{12}^{'} = a_{11}\left(a_{12}\sigma_{11} + a_{22}\sigma_{12} + a_{32}\sigma_{13}\right) + a_{21}\left(a_{12}\sigma_{12} + a_{22}\sigma_{22} + a_{32}\sigma_{23}\right) \\ + a_{31}\left(a_{12}\sigma_{13} + a_{22}\sigma_{23} + a_{32}\sigma_{33}\right)\end{aligned} \tag{A.2}$$

$$\begin{aligned}\sigma_{13}^{'} = a_{11}\left(a_{13}\sigma_{11} + a_{23}\sigma_{12} + a_{33}\sigma_{13}\right) + a_{21}\left(a_{13}\sigma_{12} + a_{23}\sigma_{22} + a_{33}\sigma_{23}\right) \\ + a_{31}\left(a_{13}\sigma_{13} + a_{23}\sigma_{23} + a_{33}\sigma_{33}\right)\end{aligned} \tag{A.3}$$

Given that $\sigma_{11}^{'}$ which is the stress component for elongational flow, then $\sigma_{12}^{'}$ and $\sigma_{13}^{'}$ are the stress components for simple shear flow. These were the forces acting on the oriented area in the current configuration. The strain tensor depicts the kinematics of the fluid flow in the pump which is then used to compute velocities, acceleration, shear and so forth. The strain rate deformation of moving flow and

can be displayed in the form of a strain tensor, $\dot{\varepsilon}_{11}$.

$$\dot{\varepsilon}_{11} = \begin{bmatrix} \frac{\partial V_u}{\partial x} & 0 & 0 \\ 0 & \frac{\partial V_v}{\partial y} & 0 \\ 0 & 0 & \frac{\partial V_w}{\partial z} \end{bmatrix} \tag{A.4}$$

Motion experienced by fluid under simple shear can be written as followed in **Equation 3.20**.

$$\dot{\varepsilon}_{12} = \begin{bmatrix} 0 & ... & ... \\ \frac{1}{2}\left(\frac{\partial V_u}{\partial y} + \frac{\partial V_v}{\partial x}\right) & 0 & ... \\ \frac{1}{2}\left(\frac{\partial V_u}{\partial z} + \frac{\partial V_w}{\partial x}\right) & \frac{1}{2}\left(\frac{\partial V_v}{\partial z} + \frac{\partial V_w}{\partial y}\right) & 0 \end{bmatrix} \tag{A.5}$$

The full derivation of the strain rate and shearing strain tensor can be seen in the **Section A.2 and A.3**. Next, the rotating component, a_{ij} of the coordinate system was solved based on the velocity of the blood flow which determines the direction for cosine function, which gives

$$a_{ij} = \begin{bmatrix} \cos a_{11} & \cos a_{21} & -\cos a_{31} \\ -\cos a_{12} & \cos a_{22} & \cos a_{32} \\ \cos a_{13} & \cos a_{23} & \cos a_{33} \end{bmatrix} \tag{A.6}$$

For rotational cosine function, a_{ij} with $i = 1$ and $j = 1$,2 and 3 and their symmetrical components

$$\cos a_{ij} = \frac{V \cdot e_j}{\|V\|} = \frac{V_j}{\sqrt{V_1^2 + V_2^2 + V_3^2}} \tag{A.7}$$

They follow the basis of Cartesian notation in the direction cosines. The rest of the directional components are computed as followed,

$$\cos a_{22} = \frac{\frac{V_u}{\sqrt{V_u^2+V_v^2+V_w^2}} + \left(1 - \frac{V_u}{\sqrt{V_u^2+V_v^2+V_w^2}}\right) V_w^2}{V_w^2 - V_v^2} \tag{A.8}$$

$$\cos a_{33} = \frac{\frac{V_u}{\sqrt{V_u^2+V_v^2+V_w^2}} + \left(1 - \frac{V_u}{\sqrt{V_u^2+V_v^2+V_w^2}}\right) V_v^2}{V_w^2 - V_v^2} \tag{A.9}$$

$$\cos a_{23} = \cos a_{32} = \frac{\left(\frac{V_u}{\sqrt{V_u^2+V_v^2+V_w^2}} - 1\right) V_v V_w}{V_w^2 - V_v^2} \tag{A.10}$$

A.2 Elongational Deformation

The fluid dynamic stresses that is experienced by blood can be best described by kinematics of the fluid. It basically refers to the motion of the fluid body without any reference to the forces or cause of motion. The fluid deformation can be best described by extension (change in length) and shear (change in internal angle) to compute velocities, acceleration, shear rate and other variables of the flow field. Let start with the derivation of deformation by elongation (strain rate),

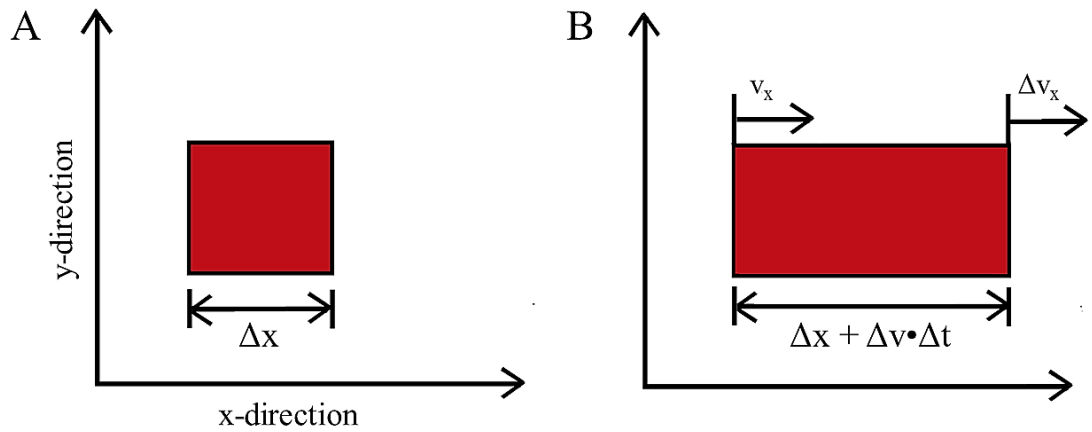

Figure A-1: A. Fluid body remains undeformed at time, t = t_0 in the direction of flow; B. Elongation deformation occurs when the body experiences velocity of fluid over period of time, t = t_0 + Δt.

Firstly, a measure of strain is divided by time, t to get strain rate as shown in **Equation 7.1** in order to form the equation of deformation, D_{xx} with regards to the direction of flow.

$$\frac{(\Delta x + \Delta v_x \cdot \Delta t) - \Delta x}{\Delta x} \tag{A.11}$$

$$D_{xx} = \lim_{\substack{\Delta t \to 0 \\ \Delta t \to 0}} \frac{1}{\Delta t} \left(\frac{(\Delta x + \Delta v_x \cdot \Delta t) - \Delta x}{\Delta x} \right) \tag{A.12}$$

By Taylor expansion of velocity in the flow direction, the equation is as followed however only the first order term was needed for the study of elongational

deformation.

$$v_x(x+\Delta x) = v_x(x) + \frac{\partial v_x}{\partial x}\Delta x + \frac{1}{2}\frac{\partial^2}{\partial x^2}\partial y \Delta x^2 A \tag{A.13}$$

The simplified measure of strain in x-direction of flow is as followed, which gives the deformation

$$\Delta v_x = \frac{\partial v_x}{\partial x}\Delta x \tag{A.14}$$

$$D_{xx} = \frac{\partial v_x}{\partial x} \tag{A.15}$$

And, if there is any changes in direction by similar method the deformation of fluid can be expressed in these forms so that volume is conserved. 2

$$D_{yy} = \frac{\partial v_y}{\partial y} \tag{A.16}$$

$$D_{zz} = \frac{\partial v_z}{\partial z} \tag{A.17}$$

A.3 Shear Deformation

The next form of fluid deformation is shear and it is described by a change in angle of α and β as shown in **Figure 7.2**. Using the tangent function, the rate of deformation in flow direction was obtained. 2

$$\tan \Delta\alpha = \frac{\frac{\partial v_y}{\partial x}\Delta x \Delta t}{\Delta x} \tag{A.18}$$

$$\tan \Delta\beta = \frac{\frac{\partial v_x}{\partial y}\Delta y \Delta t}{\Delta y} \tag{A.19}$$

The angles of change were small and can be approximated and simplified to form equations as displayed, 2

$$\Delta\alpha = \frac{\partial v_y}{\partial x}\Delta t \tag{A.20}$$

$$\Delta\beta = \frac{\partial v_x}{\partial y}\Delta t \tag{A.21}$$

Last but not least, the average deformation was taken and **Equation 7.10 and 7.11** was substituted into the change in angles, α and β.

$$D_{xy} = D_{yx} = \lim_{\Delta t \to 0} \frac{1}{2}\left(\frac{\Delta\alpha}{\Delta t} + \frac{\Delta\beta}{\Delta t}\right) = \frac{1}{2}\left(\frac{\partial v_y}{\partial x} + \frac{\partial v_x}{\partial y}\right) \tag{A.22}$$

Similarly, for deformation in different directions 2

$$D_{xz} = D_{zx} = \frac{1}{2}\left(\frac{\partial v_z}{\partial x} + \frac{\partial v_x}{\partial z}\right) \tag{A.23}$$

$$D_{yz} = D_{zy} = \frac{1}{2}\left(\frac{\partial v_y}{\partial z} + \frac{\partial v_z}{\partial y}\right) \tag{A.24}$$

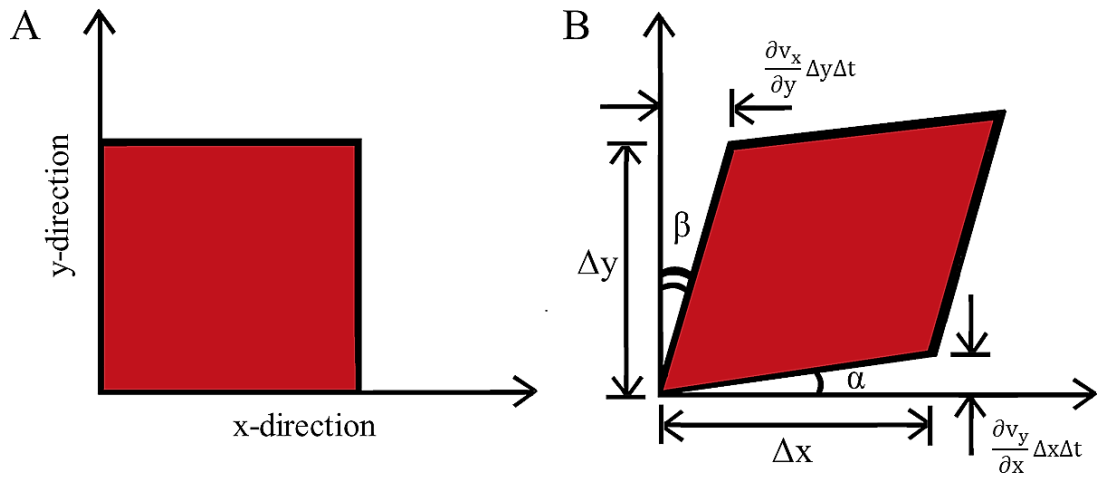

Figure A-2: A. Fluid body remains undeformed at time, $t = t_0$ in the direction of flow; B. Shear deformation occurs when the body experiences velocity of fluid over period of time, $t = t_0 + \Delta t$.